MODELING AND DYNAMIC ANALYSIS OF A TWO-WHEELED INVERTED-PENDULUM

A Thesis
Presented to
The Academic Faculty

by

Arnoldo Castro

In Partial Fulfillment
of the Requirements for the Degree
Master of Science in the
George W. Woodruff School of Mechanical Engineering

Georgia Institute of Technology
August 2012

MODELING AND DYNAMIC ANALYSIS OF A TWO-WHEELED INVERTED-PENDULUM

Approved by:

Professor William Singhose, Advisor
George W. Woodruff School of Mechanical
Engineering
Georgia Institute of Technology

Professor Kok-Meng Lee
George W. Woodruff School of Mechanical
Engineering
Georgia Institute of Technology

Dr. Wayne Whiteman
George W. Woodruff School of Mechanical
Engineering
Georgia Institute of Technology

Date Approved: 15 June 2012

This thesis is dedicated to the memory of my uncle Martin, and my

grandmother Angela.

ACKNOWLEDGEMENTS

I would like to thank my advisor, Dr. William Singhose, for his guidance on this project. I would also like to thank my committee members for their time. I would like to thank C.J Adams and James Potter for their assistance in carrying on the experiments. I also thank my sponsor, the Fulbright Program. Finally, thanks also to my brothers, my sister, my parents, and my uncles, Luis and Leonardo, for their patient support and advice.

TABLE OF CONTENTS

LIST OF TABLES

LIST OF FIGURES

SUMMARY

There is a need for smaller and more economic transportation systems. Personal transporters have made their way as consumer products to address this need. They can be found in two, three or 4-wheeled configuration. The two-wheeled configuration is a two-wheeled inverted pendulum system. One example of a commercial two-wheeled transporter is the Segway Human Transporter. However, the Segway places the operator on top of a naturally unstable platform that is stabilized by means of a control system. The control stability of the Segway can be severely affected when minor disturbances are presented. In this thesis, a dynamic model of a Segway is developed and used in simulations of non ideal conditions that can arise during normal use.

A dynamic model of a two-wheeled inverted pendulum and human rider was developed using a simple cart-pendulum system with the human rider modeled as a rigid body. Initial estimates of the parameters were calculated or obtained from references. Numerous experiments were performed better understand the dynamics of the vehicle. Different operator roles were studied. In some experiments, the operator tried to resist the movement of the vehicle, while in others he passively stood in it. The dynamic responses in both cases differed significantly and provided insights into the interaction between the person and the machine. Turning experiments were done to gather data used to characterize the yaw-rate controller of the vehicle. The data collected was then used to adjust the model parameters to match the dynamics of a real Segway Human Transporter.

The model was used to simulate different failure conditions. The simulations provide an understanding of how these conditions arise, and help identify which parameters play an important role in their outcome. The pitch angle, for example, affected the stability when traction was lost from one or both wheels. It also played a role in how well the vehicle climbed an inclined surface. Likewise, the speed was influential in the roll direction stability when making turns. The results in this thesis provide valuable information about the dynamic response of two-wheeled inverted-pendulum human transporters. The methods described in this thesis lay the groundwork for many possible future studies that may thoroughly investigate numerous different aspects of dynamics and failure modes of two-wheeled inverted-pendulum human transporters.

CHAPTER I

INTRODUCTION

There is clearly a need for personal human transporters that use less energy and take up less space than cars. Motorcycles are an obvious example of such transporters, but they cannot be used on sidewalks or indoors. Bicycles are another example that can be used in a wider range of locations, but they are human powered and have not gained much acceptance for indoor use - except in large factories. In an attempt to address one of the market-segment needs in personal human transportation, the Segway was developed. Unfortunately, the Segway is expensive and has some design defects that have resulted in its poor performance in the marketplace. The primary design defect of the Segway is that it places the operator on top of a naturally unstable mobile platform. It then attempts to both stabilize the platform and move it in a controlled manner in response to operator commands.

Given the complex dynamic behavior of inverted-pendulum human transporters, there is a need to understand their dynamic properties and their failure modes. This thesis seeks to model inverted-pendulum human transporters so that these important issues can be studied and methods for reducing the dangers of such machines can be reduced.

1.1   Inverted pendulums

The Segway is a dynamic system that is commonly referred to as an inverted pendulum. The Segway and rider form a more complicated inverted pendulum that has uncertain time-varying dynamics. Non-inverted pendulums, like crane payloads and the oscillating arm inside a grandfather clock, swing back and forth in a stable manner with limited amplitude. These types of dynamic systems occur throughout the

1

world in useful products. On the other hand, inverted pendulums do not naturally swing back and forth with a well-controlled oscillation. Rather, they fall over.

The simplest form of an inverted pendulum consists of a mass attached through a massless rod to a base mass. This is commonly known as a cart-pendulum system. This system is shown in Figure 1.1. The cart is free to move horizontally. The rod is connected to the cart through a rotational pin joint. This system is in unstable equilibrium when the rod is standing upright. Mathematically, this equilibrium can be maintained as long as there are no input forces whatsoever on the system. However, such conditions do not exist in real systems and some means of stabilization is needed to maintain the pendulum in the upright position. A force F must be applied to the cart in order to move the cart pivot back and forth from one side of the pendulum mass center to the other side. The pendulum is always falling over, but the cart motion tries to keep the leaning angle, θ, at a small level.

Given their unstable dynamics, inverted pendulums rarely occur in useful products. However, their dynamics and control have been well studied by engineers. The timeline in Figure 1.2 shows the progression of research on the dynamics and control of inverted pendulums marked by some noted events. The earliest paper listed in the database of this report is from 1908, but it is likely that even older documented work could be located.

In 1908, Stephenson [51] examined an inverted pendulum and demonstrated that it could be stabilized by applying rapid, vertical, harmonic oscillations to its base. In 1909 [52], he developed stability conditions for double and triple inverted pendulums. In 1932, Lowenstern [30] developed general equations of motion for inverted pendulums. His stability conditions aligned well with those of Stephenson.

By the 1960's, the dynamics of inverted pendulums were well understood. Many of the papers in this decade developed analytic and approximate solutions to how an inverted pendulum would respond to various inputs. The studied inputs were
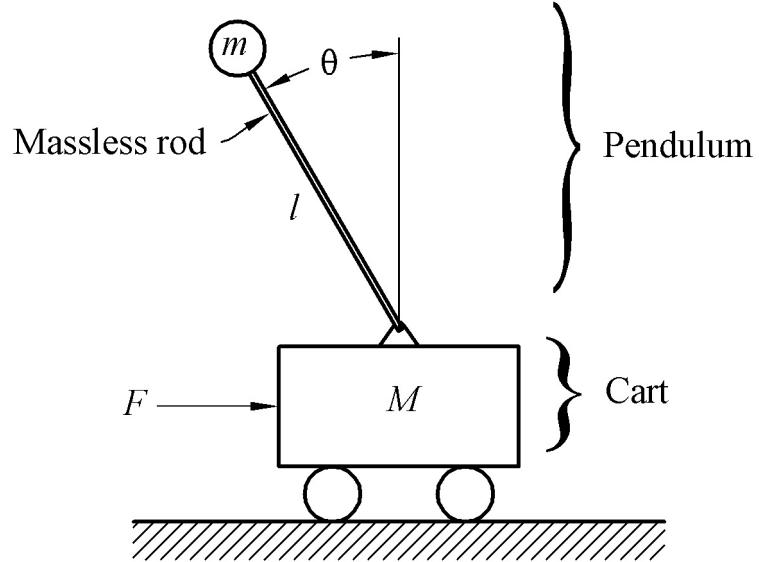
Figure 1.1: Cart-pendulum systems.
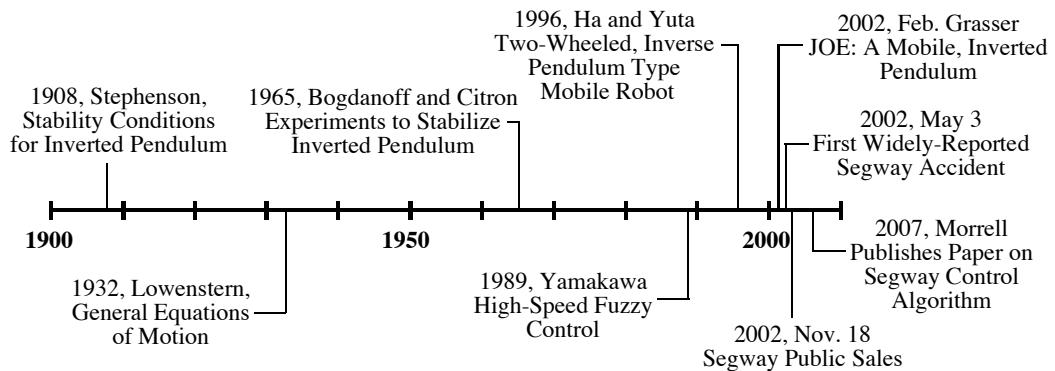
Figure 1.2: Timeline of the Inverted Pendulum Literature

generally sinusoidal, random, or impulsive. Ranges of stability were reported as a function of the input amplitude and frequency content. In particular, it was shown by several researchers that high-frequency driving inputs in both the vertical and horizontal directions could stabilize the pendulum. Numerous experimental studies were conducted to verify the stability properties [4, 40, 5, 36].

Papers in the 1980's presented controllers that could stabilize inverted pendulums for a much wider range of inputs such as parabolic and sawtooth waves [41]. Sahba [44] used an optimization algorithm to design a servocontroller instead of the more usual

3

approach of designing a controller for the linearized system. Later, Yamakawa used a specialized fuzzy controller with very high processing power for the same purpose [62]. Miles [31] found the frequencies at which a harmonic excitation can stabilize an inverted pendulum for the near vertical position. Anderson [3] managed to balance an inverted pendulum for a limited period of time by means of a single and double layer neural network. Rozenblat [42] found the optimal parametric vertical excitation required to stabilize the system.

To this day the cart-pendulum system serves as a benchmark problem for testing different control theories and visual educational demonstrations.

1.2   *Two-wheeled inverted pendulum*

To form a two-wheeled inverted pendulum (TWIP), the pendulum is anchored to a base platform that has a wheel mounted on each side, as shown in Figure 1.3. In this case, a motor drives each wheel independently. The torque from the motors makes the base move to balance pitch angle of the pendulum. It can move along curved paths by driving the motors at different speeds.

The two-wheeled inverted pendulum been proposed as a portable transporter due to its high maneuverability and small footprint [27, 9]. It has been suggested as a suitable unit for home and office environments [23]. Controlling such a system is a challenging problem due to its nonlinearities, complex dynamics, and uncertain environmental conditions [21]. The modeling of the system is also complex because of the rolling/slipping constraints of the wheels. In spite of its dynamic complexity, numerous two-wheeled inverted pendulums have been created by research institutions and companies [24] .

One of the first reported implementations of a two-wheeled inverted pendulum was done by Kanamura in 1988 [61]. By 1996, Ha [14] developed an autonomous two-wheeled inverse pendulum type robot, called the "Yamabico Kurara". This robot
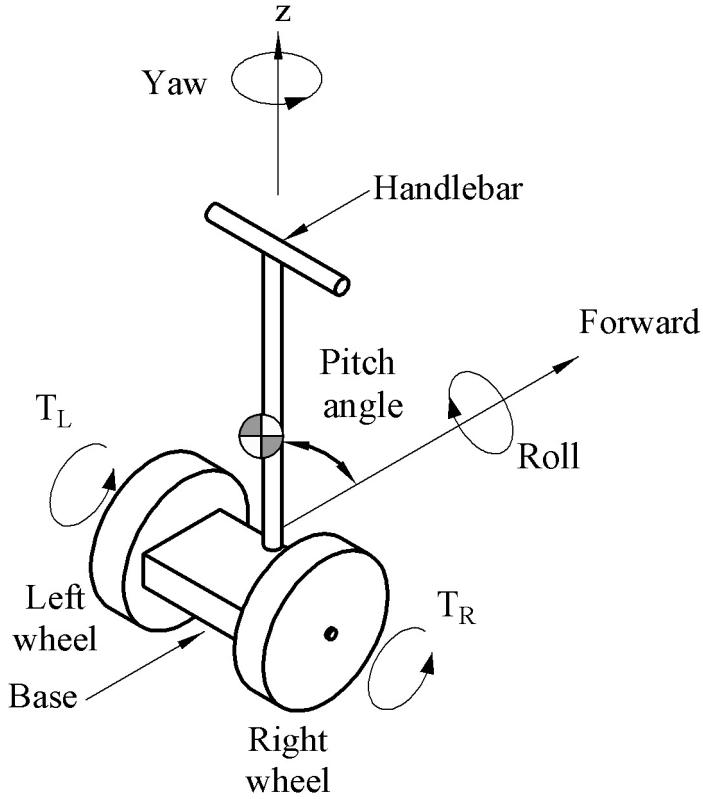
Figure 1.3: Two-wheeled inverted pendulum.

was driven by two independent driving wheels on the same axle and had a gyro type sensor to measure the inclination angular velocity of the robot's body. The same year, Shiroma [50] designed similar robots that coordinated with each other to carry a load cooperatively. In 2003, Bui [7] developed a welding mobile robot consisting of a welding torch mounted on a two-wheeled inverted pendulum that was able to follow a specified welding trajectory. In 2005, another robot [24] was introduced as a service unit for reporting fire and intruders in indoor settings. Similar robots such as the uBot series [26] and the Segway Robotic Mobility Platform (Segway RMP) series [49] continue to be used as mobile research platforms for diverse studies within the field of robotics.

In 2000, Ding [11] designed a TWIP platform intended to act as a personal transporter with an adjustable seat to keep the rider posture permanently vertical. In

2002, Grasser, et al. [13] described the development of a two-wheel vehicle named "JOE". The two-wheeled human transporter was able to stabilize the system using two decoupled DC motors driving the wheels. For safety reasons, they decided to substitute a constant weight for the driver. In 2004, Sasaki and Matsumoto [11] designed a similar vehicle but without a steering control stick. Instead, the steering was commanded by the user leaning towards one side. In 2007, Li [27] proposed a dual function vehicle that would serve both as a personal transporter and a goods transporter. In 2009, a similar robot was proposed as a baggage transporter that could follow predefined paths [55].

In 2007, Morrell and Field [32] published a paper on the design of the control algorithm used to control the Segway. In the first line of Morrell's paper, he described the two-wheeled, balancing transporter as "a novel" device. However, the authors failed to acknowledge the previous works published in the control of inverted pendulums including the highly-related papers on two-wheeled transporters like the Yamabico Kurara [14] and JOE [13]. In 2009, an experimental electric TWIP vehicle called PUMA was unveiled by GM and Segway [48].

In recent years TWIP mobile platforms have been proposed as alternatives to biped humanoid robots because of their better mobility and simpler dynamics [54]. In 2006, Kaiko [18] made an assessment of the effect of controller gains on how people perceive a TWIP humanoid robot. People were asked to judge the reaction of the robot after pushing it based on four psychological categories. Studies have also been performed on robots that coordinate their two-wheeled inverted pendulum dynamics with manipulation actions like pushing, pulling, sitting, and kicking a ball [54, 53, 25, 10].

Several approaches have been used to stabilize two-wheeled inverted pendulums. In the year 2000, Ding used a sliding mode control scheme to deal with parametric and functional uncertainties [11]. Pathak used partial feedback linearization to

design a two level position-velocity control in 2005 [38]. In 2006, Kim designed a linear quadratic regulator state feedback controller from the linearized state space equations in order to follow a reference velocity and position profile [23]. In the same year, Nasrrallah showed that a similar system could be globally stabilized without resorting to linearization techniques by choosing appropriate input and output variables [33]. Nawawi used Kim's model to develop a two-wheeled inverted pendulum robot balanced by a pole-placement controller [34]. In 2007, Jeong and Takahashi implemented a LQR state feedback control for their mobile humanoid experimental robot [16]. Meanwhile, Li implemented PID control in an experimental vehicle with two reference inputs corresponding to a human transport mode and a goods transport mode [27]. In 2008, Hopfield-type neural networks were used to balance a TWIP robot with a flexible link imitating a human lumbar spine [43]. Jung combined a neural network with a PID control to perform balancing and path following tasks [17]. In 2009, Li and Xu implemented an adaptive fuzzy controller [28], while Vlassis applied a Monte Carlo expectation-maximization algorithm to achieve balance by model free reinforcement learning [59]. In 2011, a fuzzy logic controller was designed by Huang to achieve stabilization and velocity control [15].

The unmodeled dynamics have motivated researchers to explore model-free control techniques such as neural networks and fuzzy logic implementations like the studies mentioned above. However, other studies have tried to understand these dynamics and design control techniques that consider them. Several studies have considered the dynamics involved when there are surface irregularities. For instance, Kim analyzed the effects of driving a TWIP up inclined surfaces on the torques required from the motors [23]. He noted that the turning motion had little effect on the tilting and forward motion. In 2007, Gao and Huang tested a mobile base using PID control by driving it on inclined surfaces and testing its capacity to surpass road obstacles

[27]. In 2010, Li modeled the friction between the wheels and the driving surface as uncertainties and tested an adaptive fuzzy control on this model [29].

Other studies considered changing the relative position of the global center of mass for their balance control. Humanoid Robot I-PENTAR [16] calculates the location of its center of mass and uses it to adapt the balancing controller. Another baggage transportation robot [55] adjusts its reference angle as a response to a variable load.

A few other studies have tried to incorporate external disturbance forces into their controller design. Shiroma [50] used two mobile inverted pendulum robots to cooperatively carry a load, and included a disturbance observer on their controller to improve their performance by making both robots exert the same force on the load. Sasaki [45] modeled the interaction between a TWIP vehicle with its rider as a torque exerted from the ankle of the rider to the vehicle. He included this model into the dynamics of the system which were later used to design the controller [56]. He then added a disturbance observer to estimate the handling force by the human and the slope of the ground. Choi used a reduced order disturbance observer to estimate the forces exerted by a human on a handlebar and to prevent the system from becoming unstable [9].

Even though many applications of the two-wheeled inverted pendulum system are meant to work in human environments, very little has been done to improve their safety. Kim [22] compared the performance of a PID controller with the performance of a linear quadratic regulator in preserving tilt stability at high speeds. Matsumoto [56] used a disturbance observer to account for the forces that a rider applies on a personal transporter when getting on and off the vehicle on both flat and inclined surfaces. Choi [9] applied the same approach to reject human forces on a mobile robot base that could otherwise become unstable and potentially cause harm or injury. In regard to the Segway Human Transporter, one study found that 42 injuries related to Segways were reported over a period of 44 months at one hospital, with several

degrees of severity, including 4 traumatic brain injuries [6]. Given these facts, it is important to study in more detail the circumstances under which these types of devices can fail.

1.3 Segway Human Transporter

The Segway personal transporter, shown in Figure 1.4, is a device that transports one person at relatively low speeds. The low-speed (limited to approximately 12 mph) operation combined with its electric propulsion system makes the Segway a candidate for providing short-distance transportation on city streets, sidewalks, and inside buildings. When a Segway is in use, the device is driven by two wheels that are placed side-by-side, rather than the standard in-line configuration of a bicycle or a motorcycle. When the operator leans forward, the wheels turn in unison in the same direction to provide forward motion. In order to stop, the wheels must accelerate forward to get out in front of the system's center of mass and then apply a deceleration torque to slow the system down without causing the operator to fall forward off the device. These operating principles are reversed to allow the system to move backward.

In order to turn, the wheels rotate at unequal speeds causing the system to travel in an arc. If the system is not translating forward or backward, then the wheels can rotate in opposite directions to turn the machine in place.

Given the side-by-side wheel configuration, and the elevated center of mass, the mechanical design of the transporter is unstable. It will fall over if the computerized control system is not continuously turning the wheels. This constant adjusting of the device is similar to a person balancing an inverted broom in their hand. In order to keep the broom upright, the person must continually move their hand in the direction that the broom is falling. The hand must pass to the other side of

Figure 1.4: Segway Personal Transporter.

the broom's center of mass to generate a torque that will cause the broom to start rotating in the opposite direction. As a result, the broom is always falling, but the hand motion keeps changing the direction of the fall.

Just like the inverted broom, the Segway and rider are always falling. However, it is not possible for the human operator to balance the device, as they can with a human-powered inverted pendulum such as a unicycle. The sensors in the device must constantly be measuring the state of the machine and feeding this information to the computer controller. The controller then uses this feedback signal to adjust the wheel speed so that the forward/backward (pitch) falling motion is maintained within an acceptable envelope so that device and rider do not fall over. Note that under many operating conditions, the system is mechanically stable in the side-to-side (roll) direction. Therefore, the computer does not attempt to control the roll motion. Assuming wheel-ground rolling stiction, the system is also stable in the yaw direction. However, the computer must change the yaw rate in order to turn the machine in

response to the operator input. It also limits the turning rate to a maximum value [32].

There are several different Segway models. The one shown in Figure 1.4 is the i167 model. In this model, the driver can turn by twisting a grip located on the left of the handlebar. This twisting-grip control was replaced by a leaning bar in later models, like the Segway i2. With this interface, the user has to tilt the handlebar towards the side he desires to turn. This function is shown in Figure 1.5.

Figure 1.5: Segway i2 LeanSteer technology [47].

Another version of the Segway, the x2, is intended for off-road use. It has wider tires and higher ground clearance, as shown in Figure 1.6.

Figure 1.6: Segway x2 [47].

Both the x2 and i2 models have variations that include cargo capacity. These are called the Segway i2 Commuter and the Segway x2 Adventure and are shown in Figure 1.7.

Figure 1.7: Segway i2 Commuter and Segway x2 Adventure [47].

The Segway has also been compared against other mobility methods for people with disabilities, and it is being used by the Canadian and United States Postal Services, Chicago Police, Boston Emergency Medical Services, and local university and airport security forces, among others [46].

1.4 Thesis Contributions

This thesis makes contribution to expand the understanding of the dynamics of tow-wheeled inverted pendulum and their interaction with their environments. The main contributions are:

1. A dynamic model of a two-wheeled inverted pendulum.

2. Experimental determination of the model parameters of a Segway human transporter.

3. Dynamic models of several failure conditions.

1.5   *Thesis Outline*

Chapter II starts by describing the dynamics of a cart-pendulum system. Then, it describes the model of a two-wheeled inverted pendulum and derives its dynamic equations. It then lists the parameters of the human body, and presents the dynamic equations of the two-wheeled inverted pendulum carrying a human rider. Chapter III presents the results of the experimental testing. It shows the dynamic response of two Segway human transporters to disturbance forces and turning commands. Chapter IV presents the process followed to match the simulation parameters with those of a real Segway transporter. This simulation was later used on models of failure conditions which included: inclined surfaces, loss of traction in one and two wheels, sudden turning commands, and response to disturbance forces. Finally, Chapter V provides concluding remarks and future work.

CHAPTER II

DYNAMIC MODEL OF A TWO-WHEELED INVERTED PENDULUM HUMAN TRANSPORTER

This chapter presents a model of a two-wheeled inverted-pendulum human transporter. We begin by describing the well known planar inverted pendulum.

2.1   Planar inverted pendulum model

Figure 1.1 shows the cart-pendulum system. It consists of a cart with a mass M. An inverted pendulum with a mass m, and a moment of inertia I, is attached to the cart. The center of mass of the pendulum is located at a distance l from the base. A force F is applied to the cart.
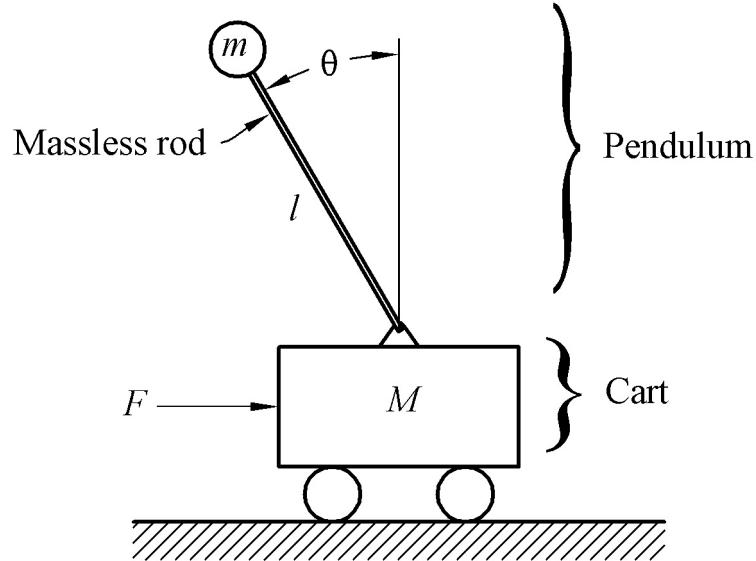
Figure 2.1: Cart-pendulum system.

A balance of forces and torques yields the following equations:

$$\left(I + mL^2\right)\ddot{\theta} - gmLsin\theta - mLcos\theta\dot{v} = 0 \tag{2.1}$$

$$mLsin\theta\dot{\theta}^2 + (M + m)\dot{v} - F - mLcos\theta\ddot{\theta} = 0 \tag{2.2}$$

where θ is the angle of the pendulum with respect to its vertical position, and v is the speed of the base with respect to the ground. These equations are combined to yield:

$$\ddot{\theta} = \frac{mL\left[cos\theta\left(F - mL\dot{\theta}^2 sin\theta\right) + g\left(M + m\right)sin\theta\right]}{(M + m)\left(I + mL^2\right) - m^2 L^2 cos^2\theta} \tag{2.3}$$

This system is unstable. If an impulse force is applied to the base, the angle of the pendulum increases without bounds as shown for an example case in Figure 2.2.
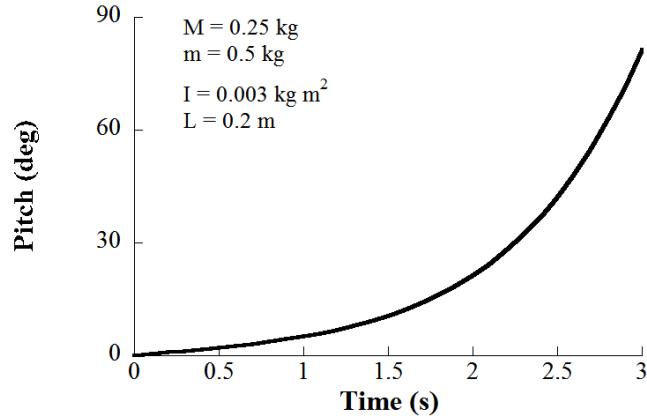
Figure 2.2: Impulse response of a cart-pendulum system.

By adding a feedback controller, the system can be stabilized. If PD control is used, the control law has the form:

$$F = K_P\theta + K_D\dot{\theta} \tag{2.4}$$

where K_P is the proportional gain and K_D is the derivative gain of the PD controller. The stabilized system is able to keep the pitch angle within finite bounds around

$\theta = 0°$. This is shown by the impulse response in Figure 2.3. Here, the pitch angle increases initially, but the controller applies a force on the base mass that makes it decrease and stabilize around zero.

Figure 2.4 shows the position of the cart. Using Figure 2.1 as a reference, the pendulum first rotates counter clockwise, and moves towards the left of the cart. As a result, the controller pushes the cart towards the left in an attempt to get below the pendulum.

In a non-inverted pendulum the characteristics of the system's response depend, besides the controller gains, on the length and inertia of the pendulum. The response of the cart-pendulum system will also be affected by the mass of the cart and pendulum.
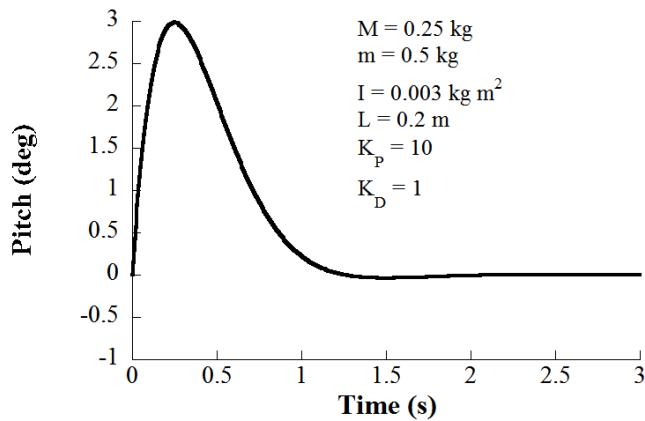
Figure 2.3: Response of the cart-pendulum stabilized by a PD controller.

2.2 Two-wheeled inverted-pendulum model

A model of a two-wheeled inverted pendulum human transporter (TWIPHT) is developed in this section. The model consists a handlebar-base assembly that will be referred to as the inverted pendulum. Attached to the base of the pendulum are two motors, that are used to drive each of the wheels. This is shown in Figure 2.5.

Figure 2.6 shows the global coordinate system 'N'. θ,γ and β are the rotation angles around the x, y and z axes, also known as pitch, roll and yaw.

16
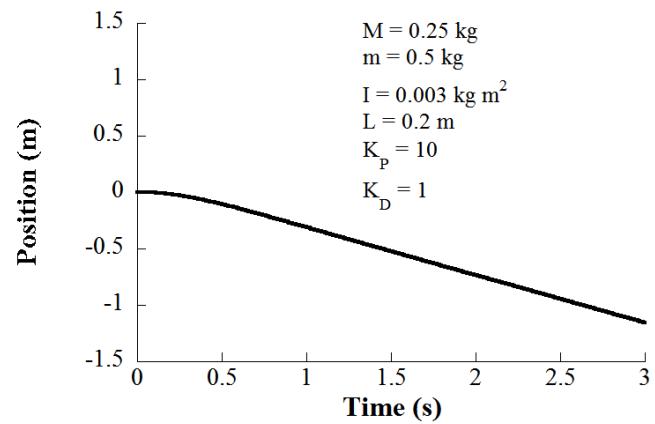
Figure 2.4: Position of the cart-pendulum.
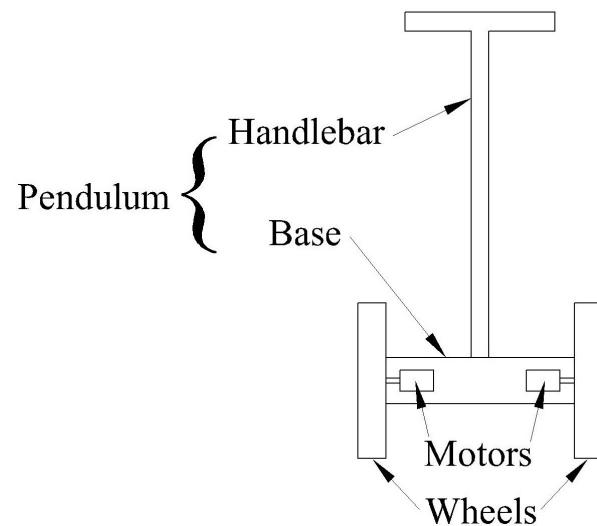
Figure 2.5: Main components of a two-wheeled inverted pendulum transporter.
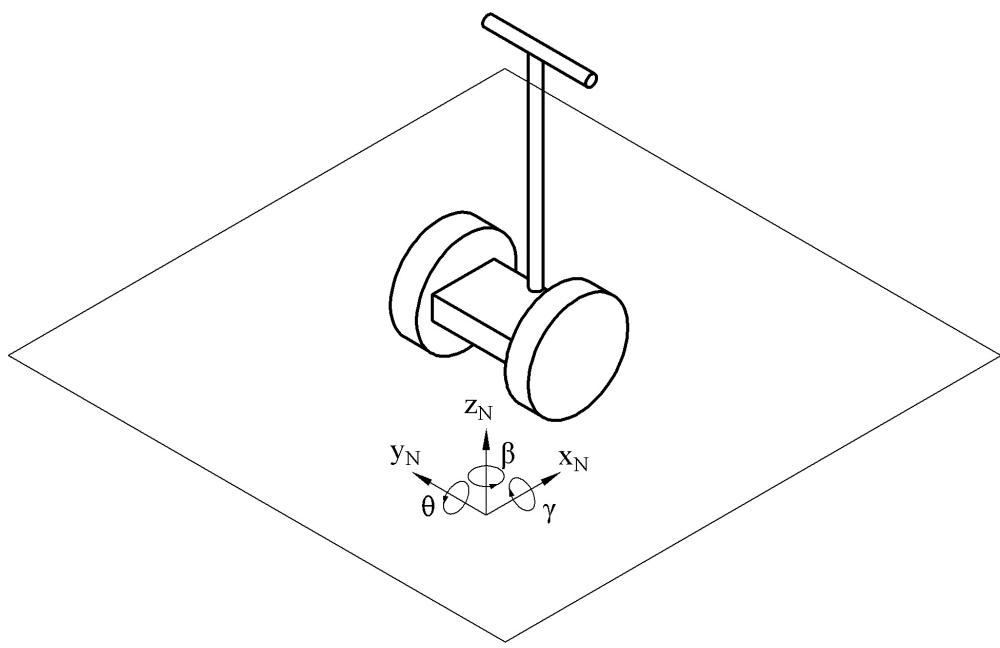
Figure 2.6: Newtonian coordinate system.

The relative rotation of the vehicle, β, with respect to the vertical axis of the global reference frame, is used to define an auxiliary reference frame 'S'. This frame is shown in Figure 2.7. Meanwhile, the rotation of the base around the wheel axis with a pitching angle θ_p defines the reference frame 'P', which is shown in Figure 2.8.
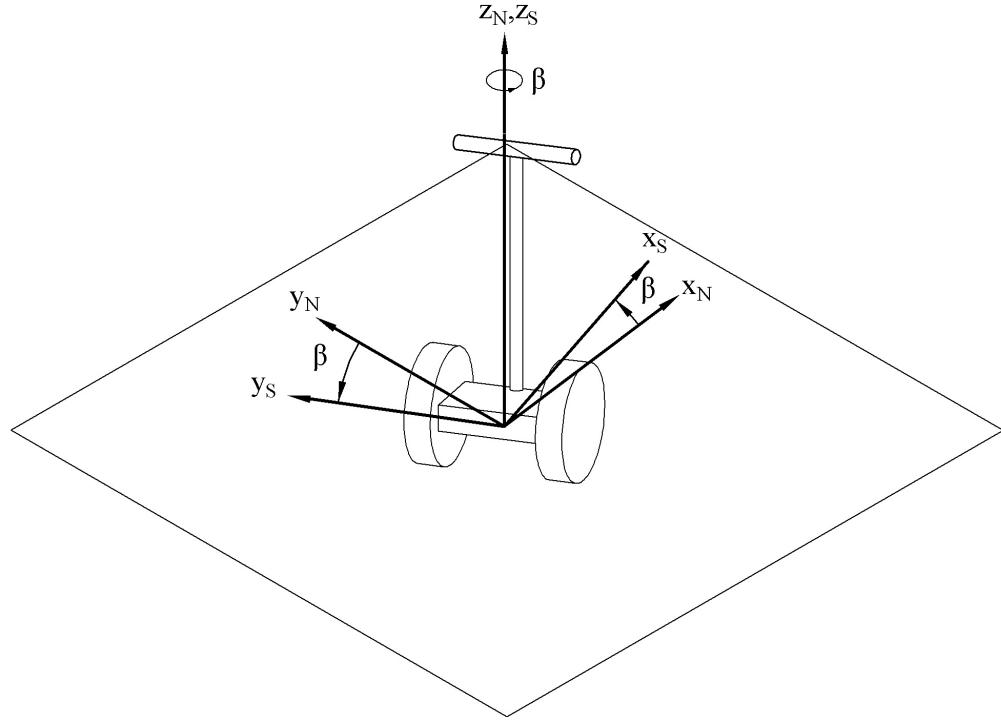
Figure 2.7: Slewing Frame 'B'.

θ_L and θ_L are the rotation angles of the left and right wheels, respectively, around the y axis of the 'S' frame. These are shown in Figure 2.9.

Figure 2.10 shows the relevant points to consider when modeling the system. Points 'lp' and 'rp' are the contact points between the base and the left and right wheels respectively. Points 'L_N' and 'R_N' are the contact points of each wheel with the ground. Point 'mid' is the point at mid distance between the centerpoint of both wheels. Point 'im' is the point at which a disturbance force can be applied. Point p_{cm} is the center of mass of the base-handlebar combination. Points l_{cm} and r_{cm} are the centers of mass of each wheel.

19
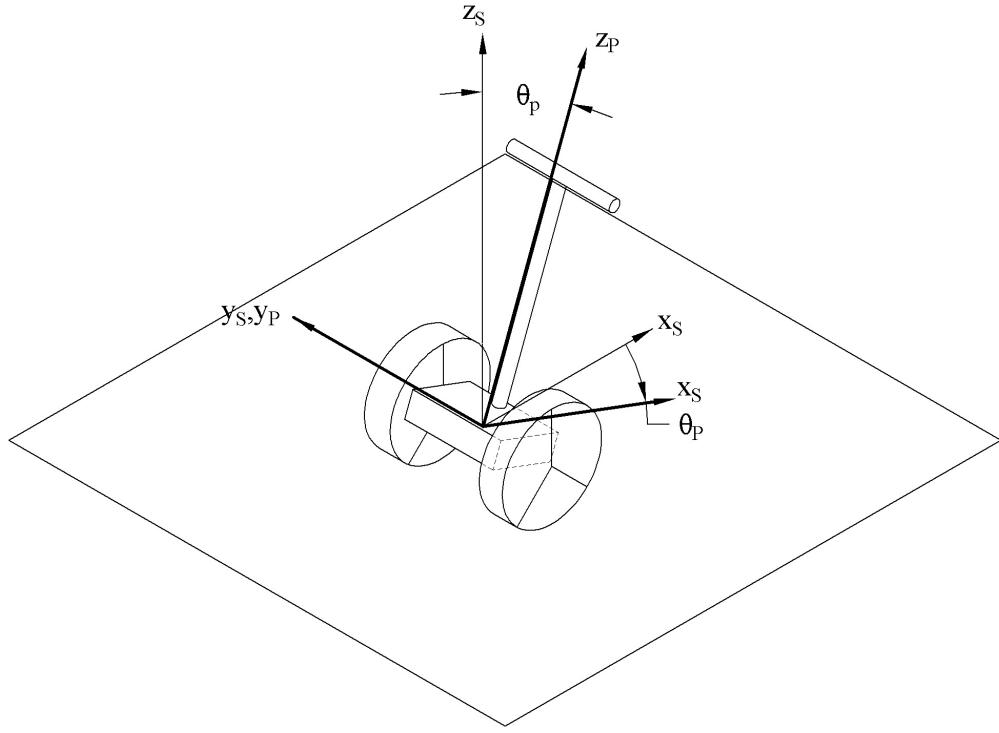
Figure 2.8: Pitching Frame 'P'.

The relevant geometric characteristics are also shown in Figure 2.10. The location of p_{cm} is defined by coordinates x_{wp} and z_{wp} with respect to the midpoint between both wheels. Point 'im' is located a distance x_{pi} in front of the axis of the wheels and a distance z_{pi} above it. The radii of the wheels is given by r_l and r_r , and the distance from point 'mid' to the center of each wheel is w.

Figure 2.11 shows the masses and forces present on the system during unloaded operation, where a test force, F_i, is a disturbance force acting on the handlebars. Besides the variables shown in Figure 2.11, the wheel inertias I_{wx}, I_{wy}, I_{wz} , and the pendulum inertias I_{px}, I_{py}, I_{pz}, are defined around their respective centers of mass.
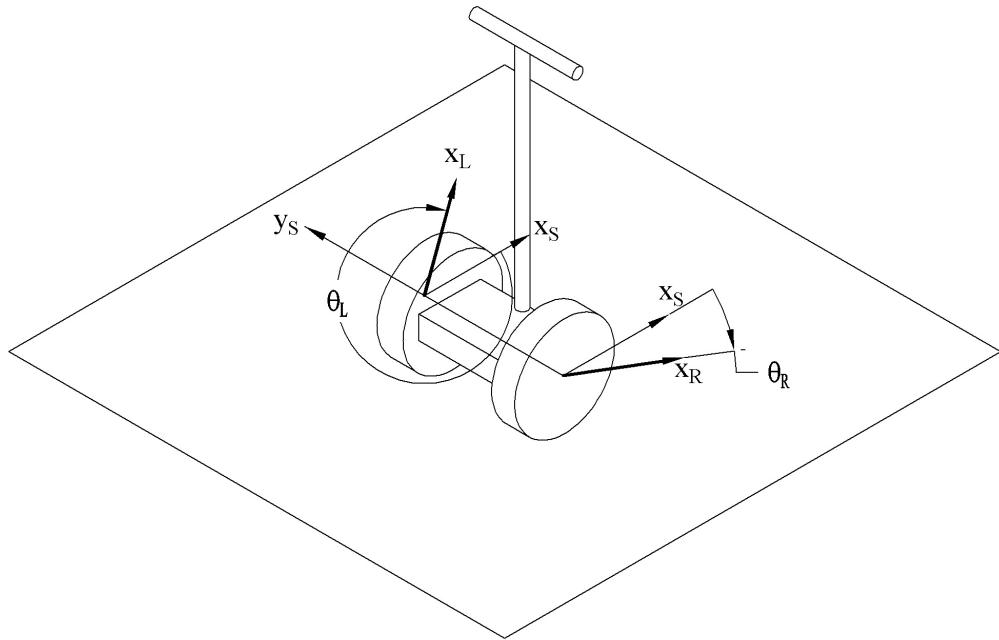
Figure 2.9: Local reference frames 'L' and 'R'.

2.3 Dynamic equations

This section first shows the kinematic equations used to defined the dynamic model of a two-wheeled inverted pendulum. These relations were introduced into a commercial multibody dynamics package to obtain the equations of motion of the system.

To develop this model, it is assumed that:

- Both wheels have same radius.

- Both wheels have the same mass.

- The wheels are not deformable.

- The wheels roll on the ground without slipping.

- The ground is a flat surface with a certain slope.

- The handlebar of the vehicle cannot be tilted sideways.
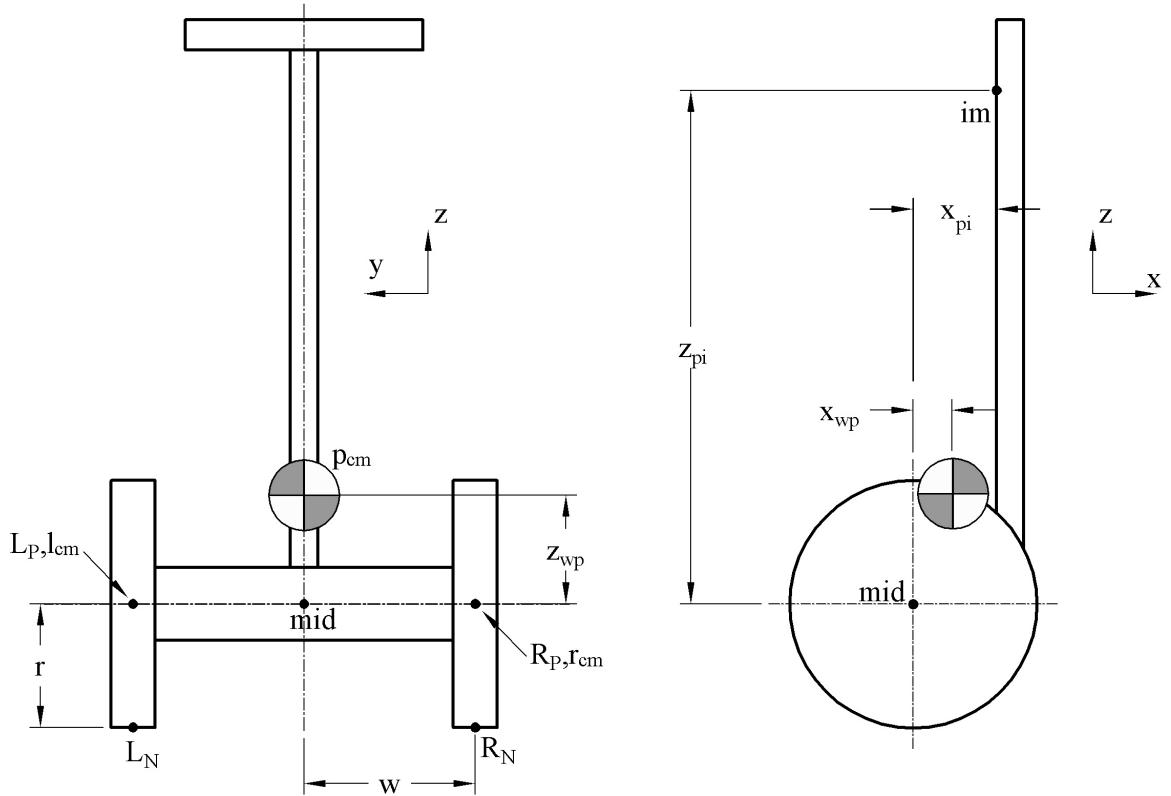
Figure 2.10: Segway model geometry parameters.

- The wheels always make contact with the ground so the vehicle is restricted from tilting in the roll direction.

- Unlike the real Segway, the vehicle does not attempt to slow down when the speed limit is reached.

- The vehicle does not attempt to push the user back if the pitch angle is too large, as it happens on commercial transporters.

- The vehicle can rotate at any desired yaw rate independently of the speed.

The velocity of the midpoint between both wheels with respect to an inertial, Newtonian reference frame, 'N', is defined as:

$$\vec{v}_{mid/N} = v_x \vec{x}_n + v_y \vec{y}_n \tag{2.5}$$

22
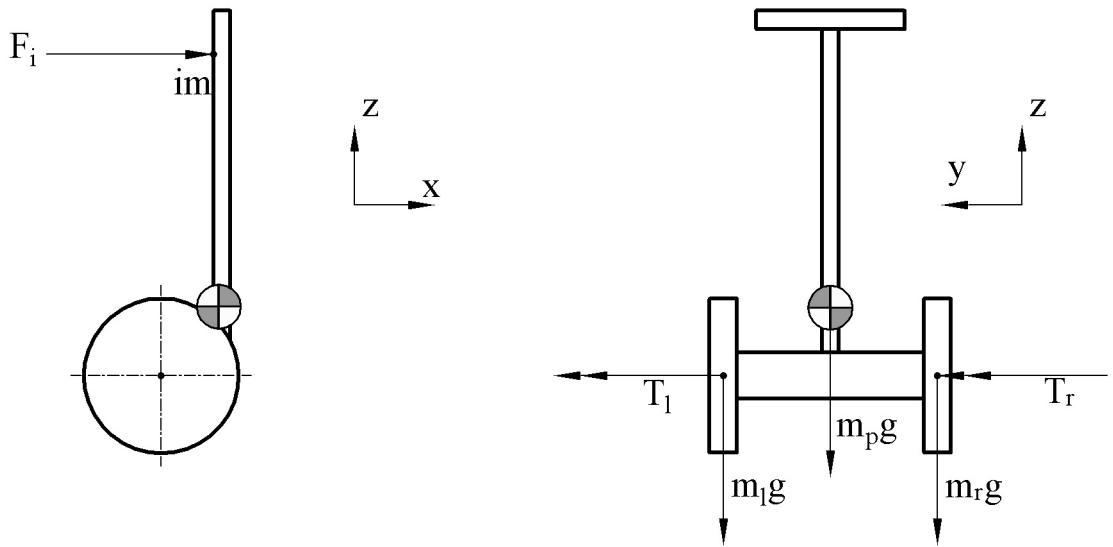
Figure 2.11: Masses and torques present during unloaded operation.

An auxiliary frame called 'S' is the frame of reference that rotates about 'N' at the same yaw angle as the vehicle. This frame of reference is used in order to simplify the definition of the angular rotation of the wheels with respect to the chassis of the vehicle. The rotational velocity of the 'S' frame about 'N' is:

$$\vec{\omega}_{S/N} = \dot{\beta}\vec{z}_N \tag{2.6}$$

The machine tilts in the pitch direction at an angle θ_P. The angular velocity of the pendulum with respect to frame 'S' is given by:

$$\vec{\omega}_{P/S} = \dot{\theta}_P\vec{y}_P \tag{2.7}$$

The angular velocity of the pendulum with respect to the Newtonian frame 'N' is then:

$$\vec{\omega}_{P/N} = \vec{\omega}_{P/S} + \vec{\omega}_{S/N} \tag{2.8}$$

23

Likewise, both wheels, which are identified by the subindices 'L' and 'R' for left and right, have angular speeds given by:

$$\vec{\omega}_{L/S} = \dot{\theta}_L \vec{y}_S \tag{2.9}$$

$$\vec{\omega}_{L/N} = \vec{\omega}_{L/S} + \vec{\omega}_{S/N} \tag{2.10}$$

$$\vec{\omega}_{R/S} = \dot{\theta}_R \vec{y}_S \tag{2.11}$$

$$\vec{\omega}_{R/N} = \vec{\omega}_{R/S} + \vec{\omega}_{S/N} \tag{2.12}$$

The position vectors to the relevant points of the vehicle are defined with respect to the midpoint between the wheels. The locations of the center of mass of the pendulum and of both wheels with respect to this point are:

$$\vec{r}_{Pcm/mid} = x_{WP}\vec{x}_P + z_{WP}\vec{z}_P \tag{2.13}$$

$$\vec{r}_{Rcm/mid} = -w\vec{y}_P \tag{2.14}$$

$$\vec{r}_{Lcm/mid} = w\vec{y}_P \tag{2.15}$$

The contact point with the ground of each wheel is defined as:

$$\vec{r}_{rn/rcm} = -r\vec{z}_N \tag{2.16}$$

$$\vec{r}_{ln/lcm} = -r\vec{z}_N \tag{2.17}$$

Using this information, the velocities of all the relevant points can be obtained:

24

$$\vec{v}_{P_{cm}/mid} = \vec{\omega}_{P/N} \times \vec{r}_{P_{cm}/mid} \tag{2.18}$$

$$\vec{v}_{P/N} = \vec{v}_{P_{cm}/mid} + \vec{v}_{mid/N} \tag{2.19}$$

$$\vec{v}_{L_{cm}/mid} = \vec{\omega}_{P/N} \times \vec{r}_{L_{cm}/mid} \tag{2.20}$$

$$\vec{v}_{L_{cm}/N} = \vec{v}_{L_{cm}/mid} + \vec{v}_{mid/N} \tag{2.21}$$

$$\vec{v}_{R_{cm}/mid} = \vec{\omega}_{P/N} \times \vec{r}_{R_{cm}/mid} \tag{2.22}$$

$$\vec{v}_{R_{cm}/N} = \vec{v}_{R_{cm}/mid} + \vec{v}_{mid/N} \tag{2.23}$$

In order to account for the no-slip velocity constraint on both wheels, the velocity of the contact point of each wheel with the ground is constrained:

$$\vec{v}_{ln/N} = \vec{v}_{L_{cm}/N} + \vec{\omega}_{L/N} \times \vec{r}_{ln/L_{cm}} = 0 \tag{2.24}$$

$$\vec{v}_{rn/N} = \vec{v}_{R_{cm}/N} + \vec{\omega}_{R/N} \times \vec{r}_{rn/R_{cm}} = 0 \tag{2.25}$$

The resultant equations of motion are:

$\ddot{\theta}_p = (m_p(x_{wp}sin(\theta_p) - z_{wp}cos(\theta_p))(F_i + (T_l + T_r)/r + m_p(x_{wp}cos(\theta_p)\dot{\theta}_p^2 + z_{wp}sin(\theta_p)\dot{\theta}_p^2 + (x_{wp}cos(\theta_p) + z_{wp}sin(\theta_p))\dot{\beta}^2)) - (m_p + 2m_w + 2I_{wy}/r^2)(T_l + T_r + F_i(x_{pi}sin(\theta_p) - z_{pi}cos(\theta_p)) - gm_p(x_{wp}cos(\theta_p) + z_{wp}sin(\theta_p)) - ((I_{px} - I_{py})sin(\theta_p)cos(\theta_p) - m_p(x_{wp}cos(\theta_p) + z_{wp}sin(\theta_p))(x_{wp}sin(\theta_p) - z_{wp}cos(\theta_p)))\dot{\beta}^2))/((I_{py} + m_p(x_{wp}^2 + z_{wp}^2))(m_p + 2m_w + 2I_{wy}/r^2) - m_p^2(x_{wp}sin(\theta_p) - z_{wp}cos(\theta_p))^2)$

$\ddot{\beta} = -(w(T_l - T_r)/r + \dot{\beta}(2(I_{px} - I_{py})sin(\theta_p)cos(\theta_p)\dot{\theta}_p - m_p(x_{wp}cos(\theta_p) + z_{wp}sin(\theta_p))(2x_{wp}$

$sin(\theta_p)\dot{\theta}_p - v - 2z_{wp}cos(\theta_p)\dot{\theta}_p)))/(I_{py} + 2I_{wxz} + 2m_w w^2 + 2I_{wy}w^2/r^2 + (I_{px} - I_{py})sin(\theta_p)^2 +$

$m_p(x_{wp}cos(\theta_p) + z_{wp}sin(\theta_p))^2)$

$\dot{v} = ((I_{py} + m_p(x_{wp}^2 + z_{wp}^2))(F_i + (T_l + T_r)/r + m_p(x_{wp}cos(\theta_p)\dot{\theta}_p^2 + z_{wp}sin(\theta_p)\dot{\theta}_p^2 +$

$(x_{wp}cos(\theta_p) + z_{wp}sin(\theta_p))\dot{\beta}^2)) - m_p(x_{wp}sin(\theta_p) - z_{wp}cos(\theta_p))(T_l + T_r + F_i(x_{pi}sin(\theta_p) -$

$z_{pi}cos(\theta_p)) - gm_p(x_{wp}cos(\theta_p) + z_{wp}sin(\theta_p)) - ((I_{px} - I_{py})sin(\theta_p)cos(\theta_p) - m_p(x_{wp}cos(\theta_p) +$

$z_{wp}sin(\theta_p))(x_{wp}sin(\theta_p) - z_{wp}cos(\theta_p)))\dot{\beta}^2))/((I_{py} + m_p(x_{wp}^2 + z_{wp}^2))(m_p + 2m_w + 2I_{wy}/r^2) -$

$m_p^2(x_{wp}sin(\theta_p) - z_{wp}cos(\theta_p))^2)$

2.4 Human model

The model in the previous section did not account for the human operator. In this section, a simple human model is described. The model of a human user of the personal transporter is shown in Figure 2.12. The silhouette of the person is shown for illustration purposes, but the model consists of a solid body with mass m_b, inertias I_{bx}, I_{by}, I_{bz}, and a center of mass located at a distance h_{cg} above the feet. This rigid body has four contact points with the personal transporter, one for each hand and foot. The distance between both hands is h_w, and the distance between both feet is f_w. The height at which the hands make contact with the handle bar is h_h.

Figure 2.13 shows the relevant points in the human body: its center of mass, and the contact points between the Segway and the person. The points labeled as 'b' are the points in the human body, while the points labeled as 'p' are the corresponding points on the Segway.
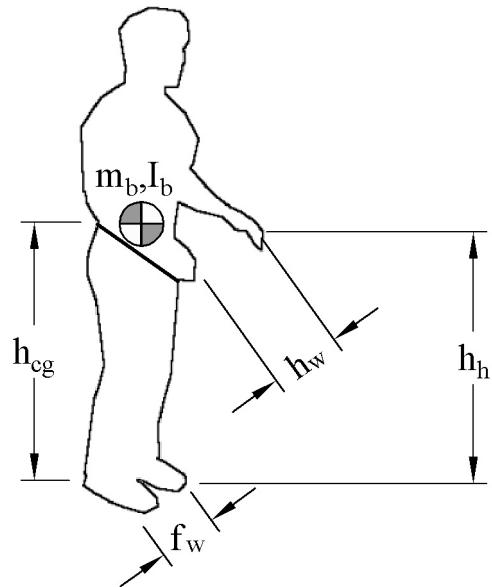
Figure 2.12: Model of the human rider.
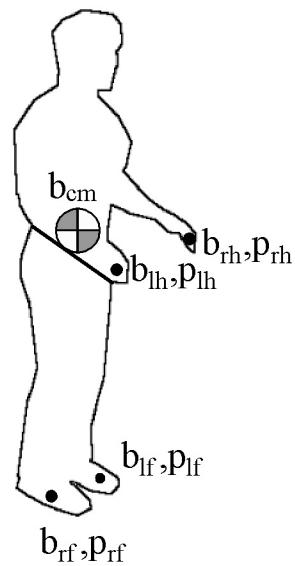
Figure 2.13: Human points.

Figure 2.14 shows the variables used to locate the hands with respect to the feet of the person. These are the height of the shoulder from the ground, the lengths of the arm and the forearm.
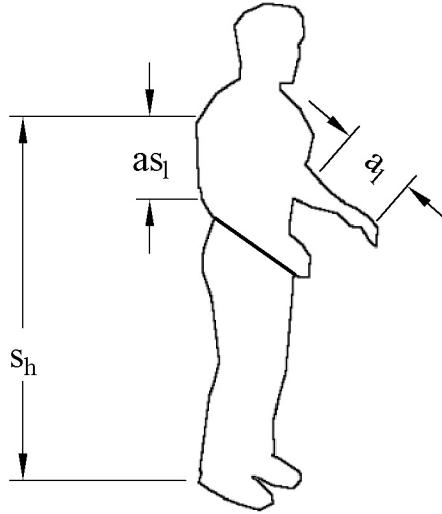
Figure 2.14: Dimensions relevant to hands location.

Figure 2.15 shows the forces that are assumed to be acting between the human body and the Segway. A torque on the feet was included because it is assumed that a person should be able to maintain balance without using his hands. This is supported in previous studies by [60].

The human body is positioned on the Segway as seen in Figure 2.16. Taking the midpoint between the centers of the wheels as the reference, the center of mass is located on the pendulum frame by the vector:

$$\vec{r}_{B_{cm}/mid} = x_{wb}\vec{x}_P + z_{wb}\vec{z}_P \tag{2.26}$$

Note that the center of mass of the system moves including a human rider has a higher center of mass. The center of mass also moves in the negative-x direction with respect to the unloaded transporter.

28
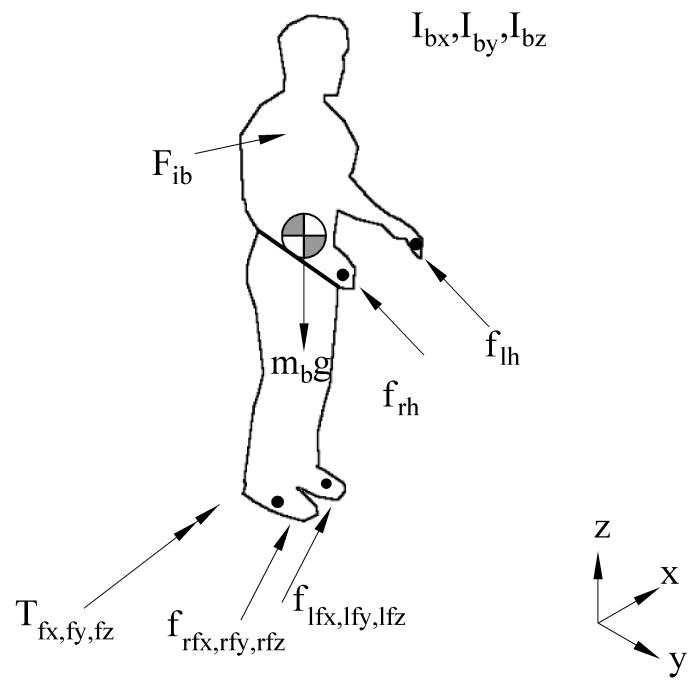
Figure 2.15: Forces acting on human body.
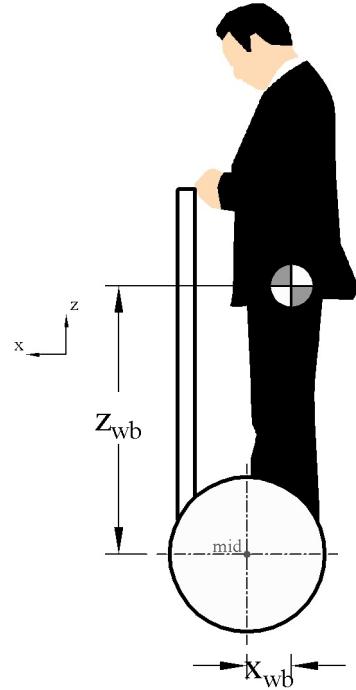
Figure 2.16: Segway model geometry.

The same procedure followed in the previous section was used to obtain the dynamic equations of motion of a human transporter with a human rider on it. A rigid body model of the human rider is considered. Because of this, it is assumed that:

- There is no relative motion between the person and the transporter.

- The human model cannot actively command the movements of the transporter.

- The connections between body segments are rigid, so there is no movement between body parts.

- The model assumes a single static posture.

- There is no flexibility between the body and the transporter. This means that the arms and legs are assumed to be rigid solid bodies.

- The human model cannot compensate for centrifugal forces during turning motion to maintain roll stability.

When the human body is included in the model, the equations of motion are given by:

$$\ddot{\theta}_p = ((m_b(x_{wb}\sin(\theta_p) - z_{wb}\cos(\theta_p)) + m_p(x_{wp}\sin(\theta_p) - z_{wp}\cos(\theta_p)))((T_l + T_r)/r +$$
$$m_p(x_{wp}\cos(\theta_p)\dot{\theta}_p^2 + z_{wp}\sin(\theta_p)\dot{\theta}_p^2 + (x_{wp}\cos(\theta_p) + z_{wp}\sin(\theta_p))\dot{\beta}^2) + m_b(x_{wb}\cos(\theta_p)(\dot{\theta}_p^2 +$$
$$\cos(\theta_p)^2\dot{\beta}^2) + \sin(\theta_p)(z_{wb}\dot{\beta}^2 + z_{wb}\dot{\theta}_p^2 + x_{wb}\sin(\theta_p)\cos(\theta_p)\dot{\beta}^2))) - (m_b + m_p + 2m_w +$$
$$2I_{wy}/r^2)(T_l + T_r - gm_b(x_{wb}\cos(\theta_p) + z_{wb}\sin(\theta_p)) - gm_p(x_{wp}\cos(\theta_p) + z_{wp}\sin(\theta_p)) - ((I_{bx} -$$
$$I_{bz})\sin(\theta_p)\cos(\theta_p) + (I_{px} - I_{pz})\sin(\theta_p)\cos(\theta_p) - m_p(x_{wp}\cos(\theta_p) + z_{wp}\sin(\theta_p))(x_{wp}\sin(\theta_p) -$$
$$z_{wp}\cos(\theta_p)) - m_b(2x_{wb}z_{wb}\sin(\theta_p)^2 + x_{wb}^2\sin(\theta_p)\cos(\theta_p) - x_{wb}z_{wb} - z_{wb}^2\sin(\theta_p)\cos(\theta_p)))\dot{\beta}^2))/$$
$$((m_b + m_p + 2m_w + 2I_{wy}/r^2)(I_{by} + I_{py} + m_b(x_{wb}^2 + z_{wb}^2) + m_p(x_{wp}^2 + z_{wp}^2)) - (m_b(x_{wb}\sin(\theta_p) -$$
$$z_{wb}\cos(\theta_p)) + m_p(x_{wp}\sin(\theta_p) - z_{wp}\cos(\theta_p)))^2)$$

$$\ddot{\beta} = -(w(T_l - T_r)/r + \dot{\beta}(2(I_{bx} - I_{bz})\sin(\theta_p)\cos(\theta_p)\dot{\theta}_p + 2(I_{px} - I_{pz})\sin(\theta_p)\cos(\theta_p)\dot{\theta}_p -$$
$$m_b(x_{wb}\cos(\theta_p) + z_{wb}\sin(\theta_p))(2x_{wb}\sin(\theta_p)\dot{\theta}_p - v - 2z_{wb}\cos(\theta_p)\dot{\theta}_p) - m_p(x_{wp}\cos(\theta_p) +$$

$$z_{wp}\sin(\theta_p))(2x_{wp}\sin(\theta_p)\dot{\theta}_p - v - 2z_{wp}\cos(\theta_p)\dot{\theta}_p)))/(I_{bz}+I_{pz}+2I_{wxz}+2m_w w^2+2I_{wy}w^2/r^2+$$

$$m_b(x_{wb}\cos(\theta_p) + z_{wb}\sin(\theta_p))^2 + m_p(x_{wp}\cos(\theta_p) + z_{wp}\sin(\theta_p))^2 + (I_{bx} + I_{px} - I_{bz} -$$

$$I_{pz})\sin(\theta_p)^2)$$

$$\dot{v} = ((I_{by} + I_{py} + m_b(x_{wb}^2 + z_{wb}^2) + m_p(x_{wp}^2 + z_{wp}^2))((T_l + T_r)/r + m_p(x_{wp}\cos(\theta_p)\dot{\theta}_p^2 +$$

$$z_{wp}\sin(\theta_p)\dot{\theta}_p^2 + (x_{wp}\cos(\theta_p)+z_{wp}\sin(\theta_p))\dot{\beta}^2) + m_b(x_{wb}\cos(\theta_p)(\dot{\theta}_p^2 + \cos(\theta_p)^2\dot{\beta}^2) + \sin(\theta_p)(z_{wb}$$

$$\dot{\beta}^2 + z_{wb}\dot{\theta}_p^2 + x_{wb}\sin(\theta_p)\cos(\theta_p)\dot{\beta}^2))) - (m_b(x_{wb}\sin(\theta_p) - z_{wb}\cos(\theta_p)) + m_p(x_{wp}\sin(\theta_p) -$$

$$z_{wp}\cos(\theta_p)))(T_l + T_r - gm_b(x_{wb}\cos(\theta_p) + z_{wb}\sin(\theta_p)) - gm_p(x_{wp}\cos(\theta_p) + z_{wp}\sin(\theta_p)) -$$

$$((I_{bx} - I_{bz})\sin(\theta_p)\cos(\theta_p) + (I_{px} - I_{pz})\sin(\theta_p)\cos(\theta_p) - m_p(x_{wp}\cos(\theta_p) + z_{wp}\sin(\theta_p))(x_{wp}$$

$$\sin(\theta_p) - z_{wp}\cos(\theta_p)) - m_b(2x_{wb}z_{wb}\sin(\theta_p)^2 + x_{wb}^2\sin(\theta_p)\cos(\theta_p) - x_{wb}z_{wb} - z_{wb}^2\sin(\theta_p)$$

$$\cos(\theta_p)))\dot{\beta}^2))/((m_b + m_p + 2m_w + 2I_{wy}/r^2)(I_{by} + I_{py} + m_b(x_{wb}^2 + z_{wb}^2) + m_p(x_{wp}^2 + z_{wp}^2)) -$$

$$(m_b(x_{wb}\sin(\theta_p) - z_{wb}\cos(\theta_p)) + m_p(x_{wp}\sin(\theta_p) - z_{wp}\cos(\theta_p)))^2)$$

CHAPTER III

EXPERIMENTAL DETERMINATION OF PARAMETERS

Several types of experiments were performed on a Segway i2 and a Segway i167 personal transporter. The purpose of the experiments was to obtain the dynamic response of both transporters to disturbance inputs, and use that information to develop a realistic dynamic model. Additionally, turning commands were given to both Segways and their responses were recorded. We start with a description of the experimental procedures and then discuss the results and their implications.

3.1 Experimental procedures[1]

A Vicon MX motion capture system was used to measure the position and orientation of the Segway in real-time. The motion capture system is composed by 12 infrared cameras that track reflective markers placed on the objects to be tracked. The data signal flow in this system is shown in Figure 3.1. The system consists of 12 MX-3+ cameras connected via 2 Vicon MX Ultranet HD units that stream camera data to the computer at a 120 Hz rate. Vicon iQ version 2.5 software running on the computer processed the camera data. The resulting position and orientation measurements were exported to MATLAB using the Vicon Tarsus Realtime data streaming application. The orientations, measured with respect to the global reference frame, were converted to Euler angles. Each MX-3+ camera can record 659x493 grayscale pixels, and position measurements made using this system have a resolution of approximately 1 mm [57, 58].

---

[1]*Experiments were performed with the collaboration of C.J. Adams and James Potter.*
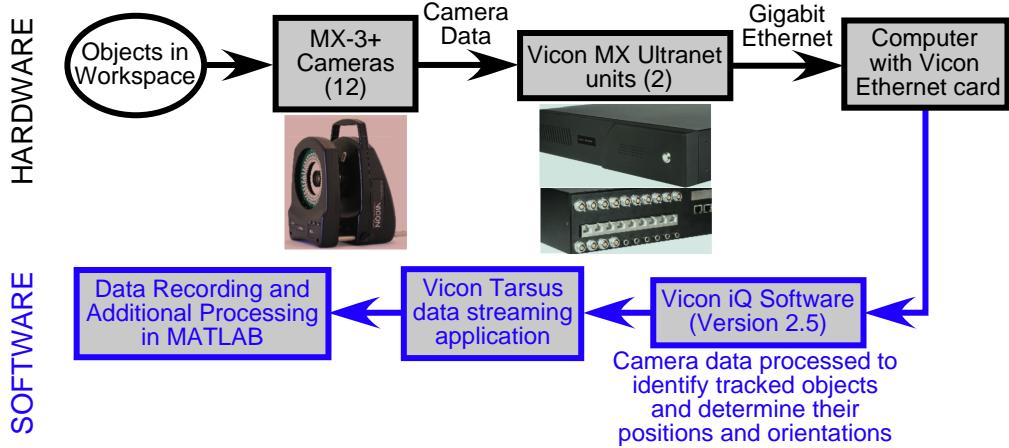
Figure 3.1: Motion Capture System Signal Flow.

Figure 3.2 shows the experiment setup for applying a disturbance force to the handlebars. On the left side is an elevated weight that is dropped. This falling weight applies forces to the Segway via the attached rope that passes through a pulley and attaches to the handlebars. Once the markers were placed on each body, a calibration was performed. Each body requires an arrangement of makers so that the software can compute their position and orientation. During the calibration, the body is placed at an arbitrarily chosen reference position and orientation. Then, within the Vicon iQ software, the body is defined and its initial coordinates stored. The recorded coordinates of each bodies during each test are measured relative to the initial calibration reference.

The position and orientation data is processed by the Vicon iQ software and recorded by a MATLAB script. The recorded data is stored as a MATLAB-variable file that contains the three coordinates and three orientation angles of each object.

A wood structure was built to apply disturbance forces on the Segway by dropping a set of weights. This structure is shown in Figure 3.3. It has a pulley attached at its top that converts the vertical rope to a horizontal state so that it can connect to the Segway. A load of 100 lbs. was used for most disturbance testing.
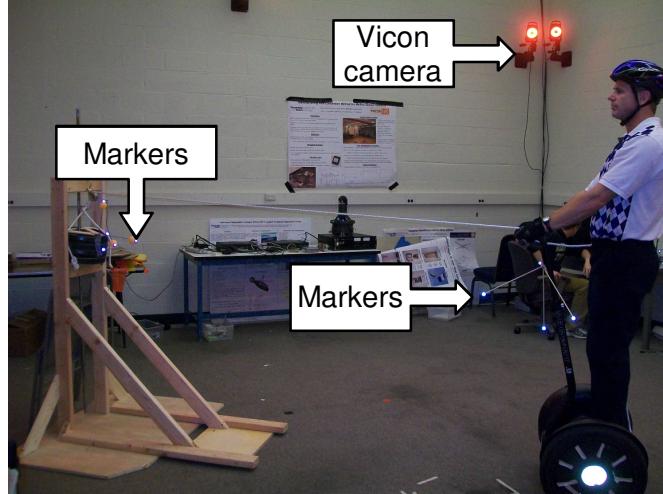
Figure 3.2: Markers and cameras.

3.1.1 Description of the experiments

The experiments performed can be divided into three categories: pulse response tests, yaw input command tests, and road disturbance tests. The first two tests were performed on both a Segway i2 and a Segway i167. The road disturbance tests were performed only on a Segway i2.

In the pulse response tests, a force "pulse" was applied on a Segway that was initially at rest. This was done for both unloaded Segways and loaded Segways (with a human rider on it). Figure 3.4 shows a manual pulse being applied to an unloaded Segway i167. The person simply pushed on the upper part of the Segway handlebars and the resulting motion of the Segway was recorded.

Segways have four pressure sensors covered by a mat over which a rider normally would stand. When the sensors are not pushed, the control system of the Segway limits the maximum speed it can reach. Therefore, if the sensors are not pushed, the impulse response is distorted, and instead of reaching an equilibrium pitch angle, this angle drifts back in order to reduce the speed. This is illustrated in Figure 3.5. To obtain the true impulse response in the unloaded tests, the sensors were held closed, and thus, the speed-limiting function was not triggered.
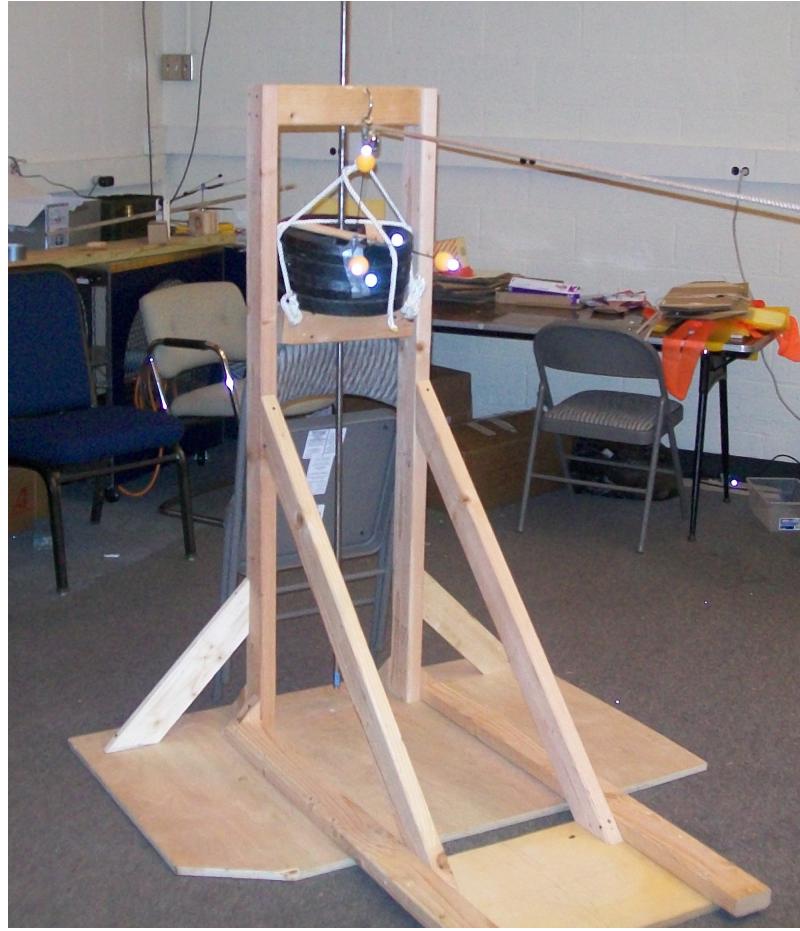
Figure 3.3: Weight dropping mechanism.

For the loaded Segway case, the force could either be applied manually or by using the weight dropping mechanism described previously described. When the force was applied manually, it was done by pushing the rider on the back, as shown in Figure 3.6. When the weight dropping mechanism was used, the force was applied to the handlebars, making the Segway pitch and move forward. This is shown in Figure 3.7.

The pulse tests were performed with different operator states. In one case, the operator acted as a rigid body attached to the Segway. In another case, the operator tried to resist the Segway motion, or slow it down. In a third case, the operator actively set the Segway into motion himself. In this case, the user riding the Segway performed the actions required to start and stop the transporter. To start moving, the user leaned forward, making the center of mass of the user-transporter system
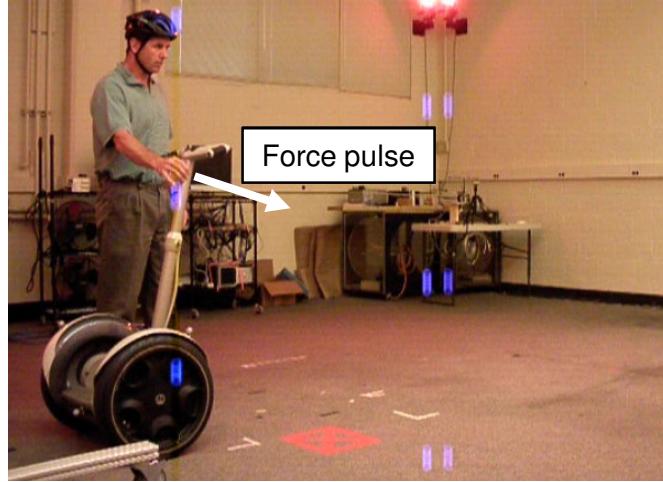
Figure 3.4: Manual pulse force applied on an unloaded Segway i167.

move forward, and causing the base to speed up in order to achieve balance. To stop, the user leaned backwards, and the controller responded by reducing the speed.

The second class of tests that were done were the yaw command input tests. These can be divided in two categories: spinning tests and turning tests.

A spinning test is shown in Figure 3.8. The rider made the Segway i2 spin at a constant rate by rolling the handlebars to the side at a fixed angle. This type of control input to induce turning differs from earlier versions of the Segway, which were turned by twisting the left hand grip. After a few seconds, the handlebars were tilted to a different angle which produced a different rotation rate. This process was repeated for a range of handlebar roll angles. These spinning tests were repeated on a Segway i167, but the left hand twisting grip yaw control was used instead of the tilting handlebar. In this case, the grip was twisted at different angles to achieve a range of turning rates.

Figure 3.9 shows a Segway i2 turning test. The Segway started at rest (Frame 1 in Figure 3.9), and then accelerated forward to a constant speed (Frame 2). The rider then made a 180-degree turn. Note that the rider must lean into the turn (Frame 3) to keep from falling off the machine. This lean must be maintained throughout the
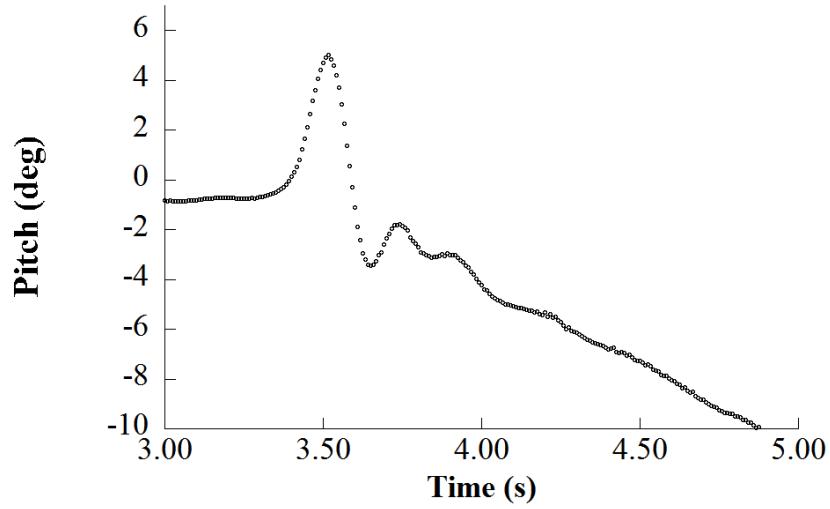
Figure 3.5: Speed limited response.

turn (Frames 4-6). The operator must adjust their lean angle to offset the centripetal acceleration caused by the turning machine. If the machine makes an unexpected turn, or unexpectedly changes its turning radius, then the rider can fall off the device because they cannot change their lean angle fast enough. This was repeated using a Segway i167.

Finally, the Segway i2 road obstacle tests were performed. These consisted of having the Segway drive over a block on the ground. This is shown in Figure 3.10.
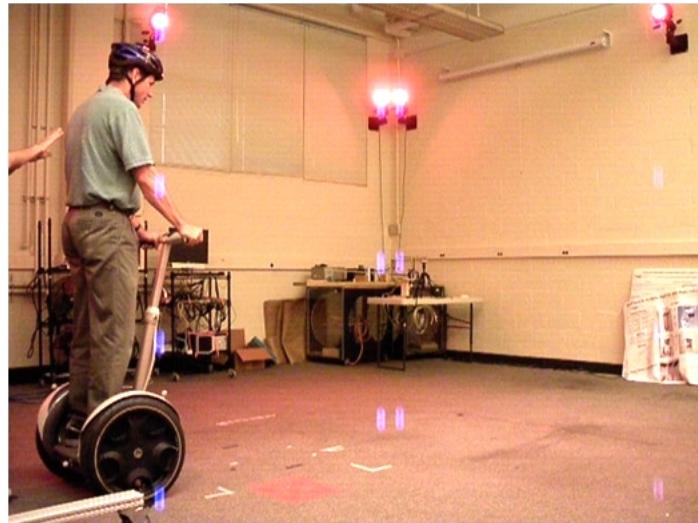
Figure 3.6: Manual pulse force applied on a loaded Segway i167.
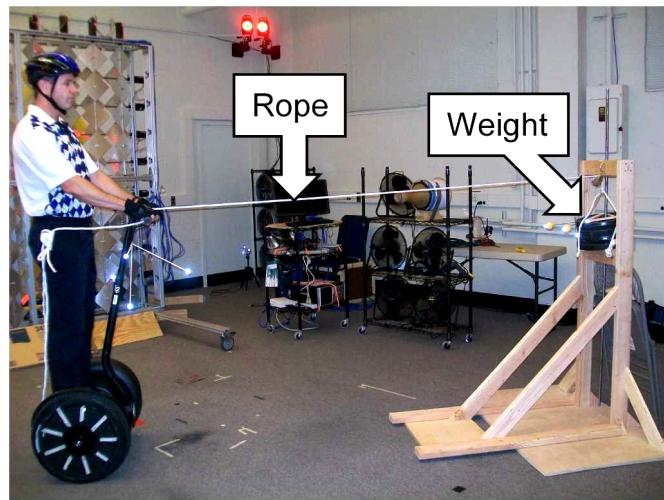
Figure 3.7: Force applied to the handlebars using the weight dropping mechanism.

Figure 3.8: Spinning Test on a Segway i2.
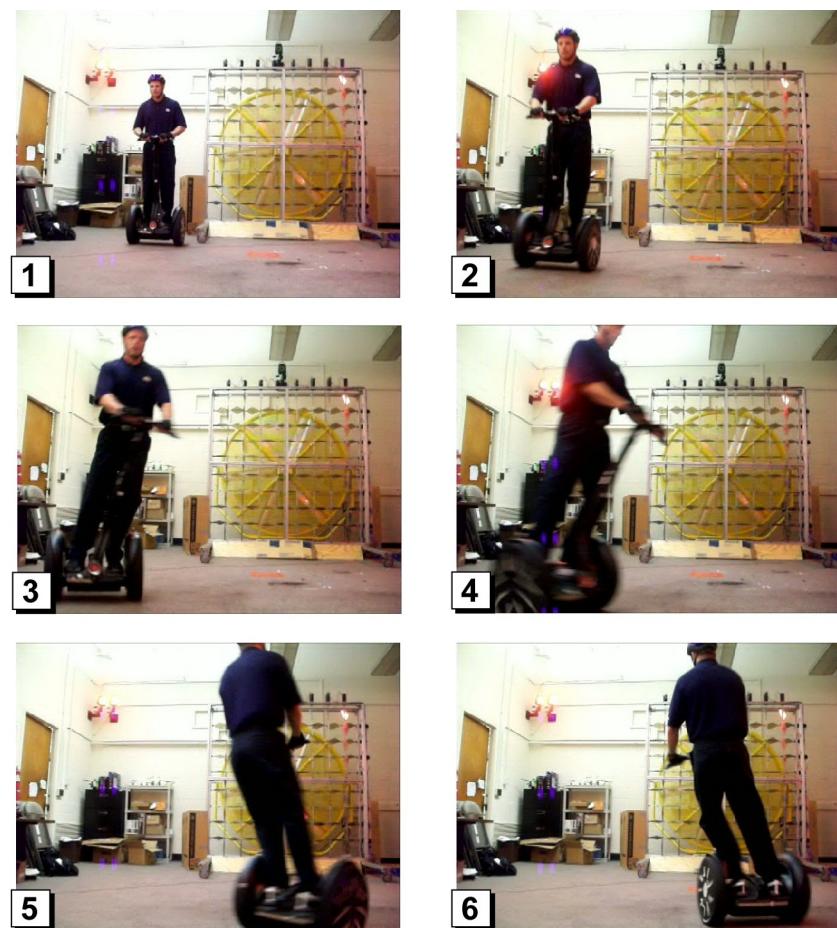
Figure 3.9: Turning test on a Segway i2.
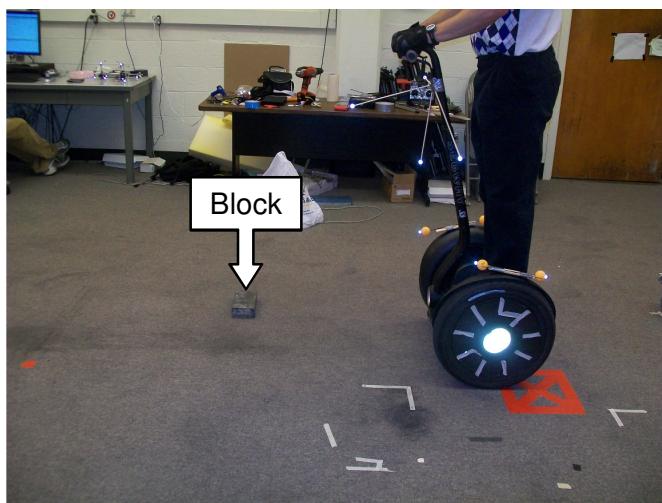
Figure 3.10: Bump test on a Segway i2.

3.1.2 Weight fall calibration

Initial tests with the weight dropping mechanism revealed that the friction between the weights as they fell and the support structure could be a significant force that could affect the final measurements. A test was performed to measure this friction force. The acceleration was obtained from the position data by using a 9th order smooth noise robust differentiator [39]. The upward force, T that opposes the fall of the weights is given by:

$$T - mg = ma \tag{3.1}$$

$$T = mg + ma \tag{3.2}$$

where g is the acceleration of gravity (9.81m/s^2) and a is the acceleration of the weights.

Figure 3.11 shows the position of the weight as it falls down, as well as the opposing upward force that resists the fall. This test was performed two times. Initially, the weight was held at a height near 0.84 m. In this position, the weight has zero acceleration, so by using (3.2), the total upward force is initially equal to the weight being held. When the weight is allowed to fall, this force drops almost to zero. This means that as it falls down, the upward force that opposes motion is close to zero. It can be seen in Figure 3.11 that there is a sudden increase of this force towards the end of the test. Given that in both cases the peak towards the end has a similar magnitude, there is an aspect of the weight dropping mechanism that caused the weights to experience a disturbance at a certain height. After this, there is a gap in the collected data. This was caused by structural components at a low height, that blocked the view of some of the cameras. For each test, an average force was calculated from the falling range during which it was relatively constant (for example

from 8.5 to 8.8 s in Figure 3.11), and then both values averaged. This resulted in an average resisting force equal to 59.62 N.
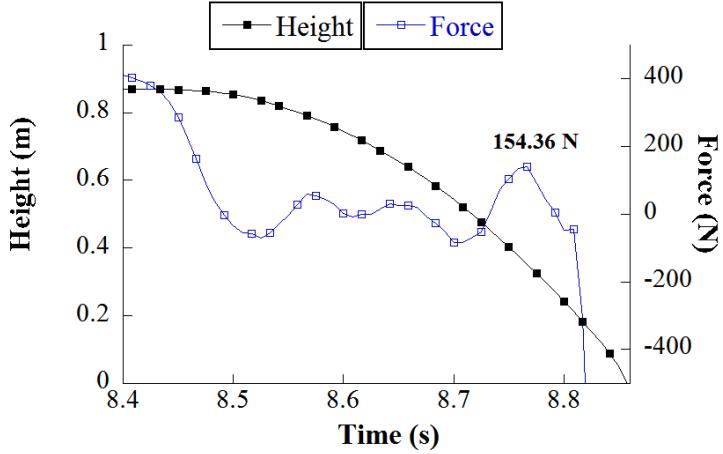
Figure 3.11: Weight fall calibration tests.

3.2   Segway i2 tests results

3.2.1   Manual pulse on an unloaded Segway i2

Figure 3.12 shows the pitch response to a manual force input of a Segway i2. Initially, both the handlebar and the base orientation were recorded. Note in Figure 3.12 that there is not a significant difference between the base and the handlebar pitch angles, which means both measurements record the same information. At time 1.2 s, when the Segway starts tilting, Figure 3.12 shows a gap in the handlebar pitch data that was caused by the motion capture system losing track of the markers.

The Segway i2 was manually pushed with different strength forces. Because this "pulse" force was applied manually, it could not be measured. However, the strength of the pulse is identified by the maximum pitch angle of the response. Figure 3.13, shows the speed and pitch angle for the 5.1° maximum pitch case. Note that when the pitch angle settles, the speed continues to increase. Also, the speed shows a delay

42
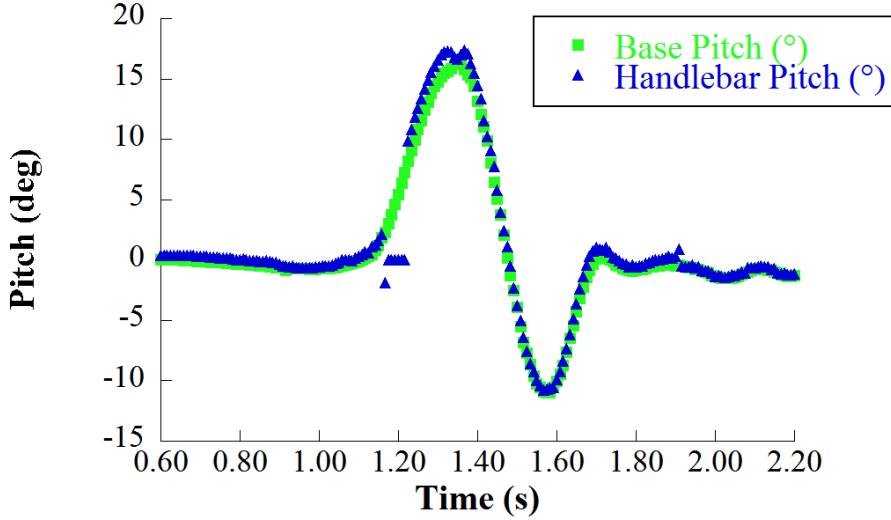
Figure 3.12: Base and handlebar pitch angle.

in its response with respect to the pitch as can be seen in the delay between both peaks. It can be observed that when the pitch is positive, the acceleration of the transporter increases.
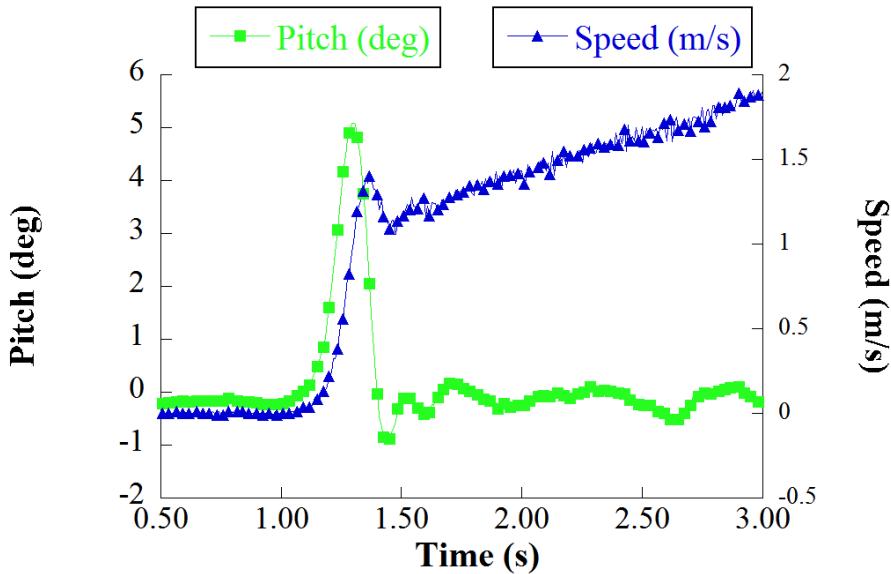
Figure 3.13: Speed and pitch angle responses for a small (5.1°) impulse.

Figure 3.14 shows the pitch responses for several different pulse magnitudes. Note that the greater the magnitude of the exerted pulse, the larger the period of the response. Therefore, the response is not exactly a linear under damped response. In

43

spite of the nonlinearities, damping ratios and damped periods were estimated using the first positive and the first negative peaks of the responses. The damping ratio was found by solving:

$$\ln\left(\frac{\theta_{max} - \theta_{ss}}{\theta_{ss} - \theta_{min}}\right) = \frac{\pi\zeta}{\sqrt{1 - \zeta^2}} \tag{3.3}$$

where θ_{max} is the maximum pitch, θ_{min} is the minimum pitch, θ_{ss} is the steady-state pitch and ζ is the damping ratio.
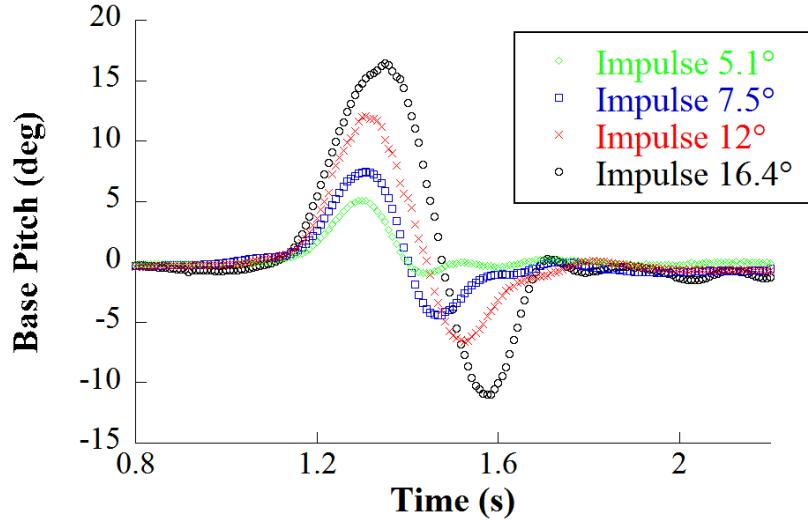
Figure 3.14: Pitch angle.

Figure 3.15 shows the period for each pitch response amplitude, or maximum pitch. Notice that as the response amplitude increases, the period does the same. An inverted pendulum can be considered linear for small pitch angles, but as the pitch angle increases, the nonlinearity manifests itself as a change in the frequency of the response. Even though the maximum angle is near to 18° (~0.3 rad) it is large enough to produce noticeably different oscillation periods.

44
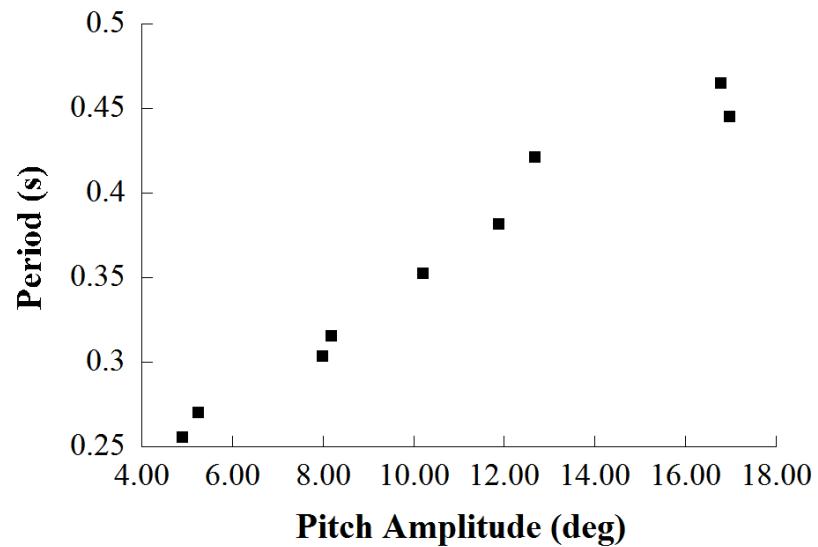
Figure 3.15: Period vs. Pitch response amplitude.
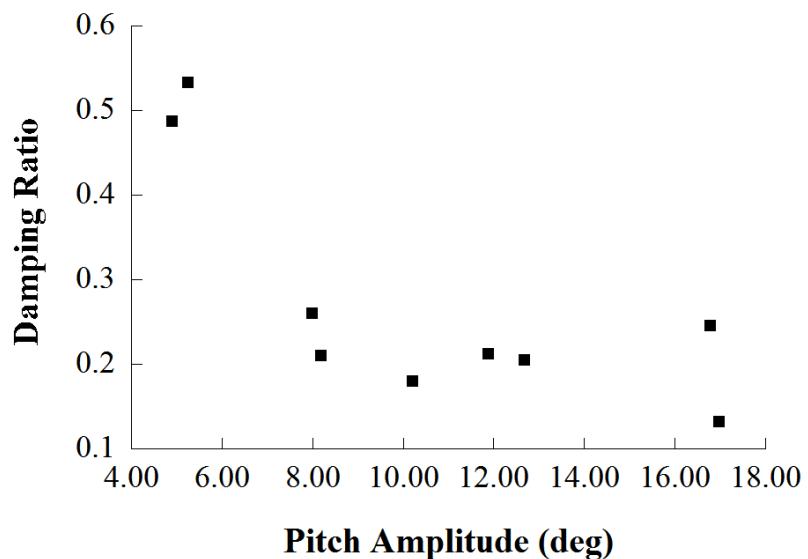
Figure 3.16: Damping ratio vs. Pitch amplitude.

Figure 3.16 shows the damping ratios for each peak pitch angle. Damping ratios were found to be between 0.4 to 0.6 for maximum pitch angles under 6°. Above that, the damping is approximately 0.2. The use of of these damping ratios is limited because the system is not linear. However, they do indicate the system will have a multi-peak response to large disturbances.

In Figure 3.17 the base speed is plotted for the four different pulses magnitudes. It shows that the speed increases as the initial pulse is stronger. The speed response oscillates around a line with positive slope (constant acceleration). As in the pitch responses, the frequency decreases as the pulse is stronger. This effect is noted by observing the period of time between the oscillations around the steady state speed. The exception to this behavior is the highest impulse (16.4°) response, which was probably affected by the speed limiting mechanism of the Segway.
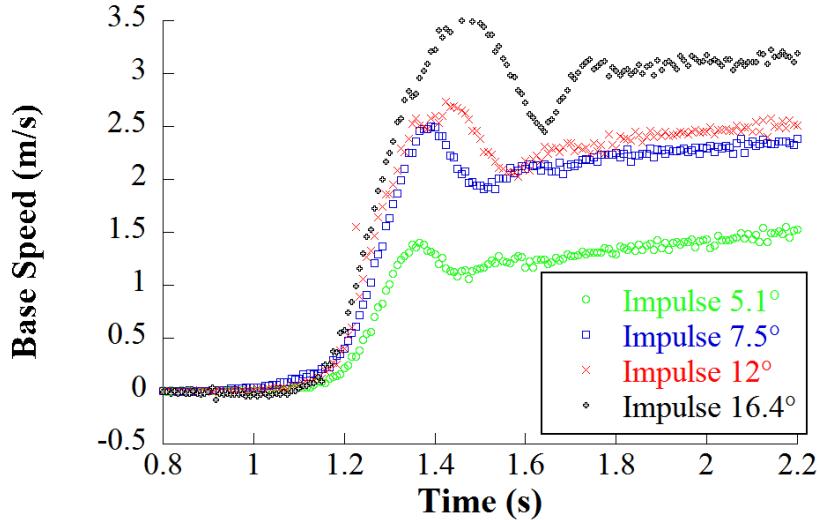
Figure 3.17: Base speeds for different impulse magnitudes.

Figure 3.18 shows the initial maximum speed (first local maximum in the speed response) against the maximum pitch angle. Here it is noted that both follow the same trend. Figure 3.19 shows the steady state acceleration plotted against the maximum pitch. This is the acceleration of the vehicle after the oscillations have dissipated. The steady state acceleration decreases as the pulse is stronger. For strong enough

46

force inputs, the Segway reaches its speed limit and cannot increase it beyond that. This is why for strong pulse forces the Segway settles to a very low acceleration value.
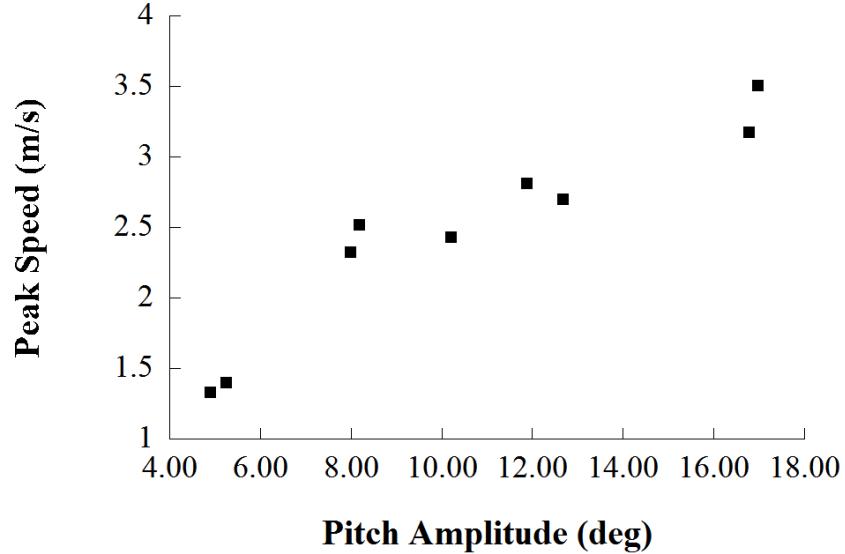
Figure 3.18: Peak Speed vs. Pitch Amplitude.

3.2.2 Manual pulse on a loaded Segway i2 - static user

Figure 3.20 shows the pitch angle response of an i2 Segway when the person riding it was pushed from behind on his back. It is noticed that in this case the peak angle does not reach values as large as the ones that were present in the unloaded case. The period of the response is larger because the center of mass is vertically higher than the unloaded Segway. Because the maximum pitch angle ranges within a smaller interval, the variation of periods of the responses is also smaller than the unloaded case. A smaller pitch angle range means that all the responses deviate similarly from the near zero pitch angle behavior (which can be referred to as the linear range). Figure 3.20 shows some noisy data in the 5.42° pulse response near time 1.8 s that was caused by the motion capture system losing track of the markers mounted on the Segway.

Figure 3.21 shows the speed response of the loaded i2 Segway. As in the unloaded case, speed is larger as the impulse is increased. In this case, however, the speed oscillates around a constant value instead of a constant acceleration line. This is due
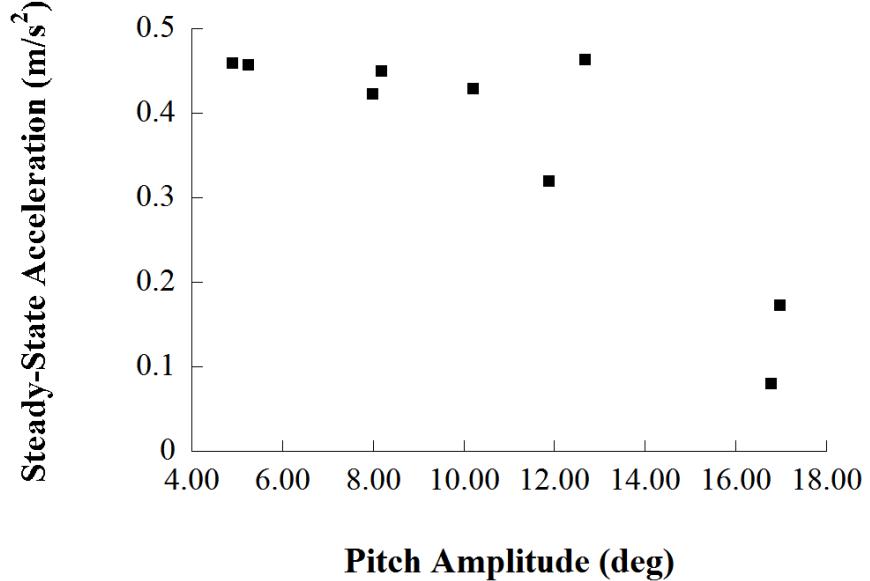
Figure 3.19: Steady-State Acceleration vs. Pitch Amplitude.

to the center of mass of the transporter-rider system being more directly above the axis of the wheels.

The loaded i2 Segway response, as mentioned before, shows larger time periods than the unloaded Segway. As shown in Figure 3.22, the period shows a decreasing trend with respect to the maximum pitch. However, all periods are within a very small range between 0.94 s and 1.08 s. This constitutes a small sample and does not provide strong evidence to conclude that the period decreases with an increasing pitch for all pitch angles. It is likely that the error associated with the measurement and computation of the periods is larger than the range presented here. It was expected that a larger maximum pitch would produce lower frequencies [35].
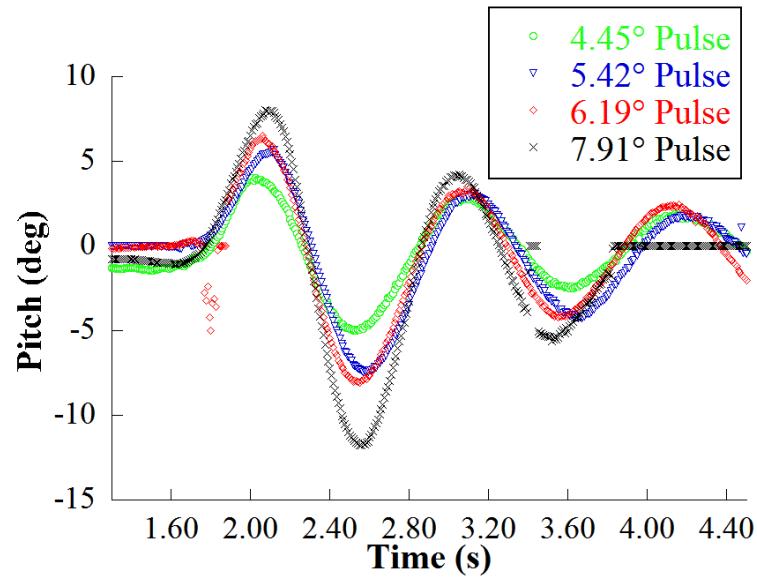
Figure 3.20: Pitch Response of a loaded i2 Segway to a force input.
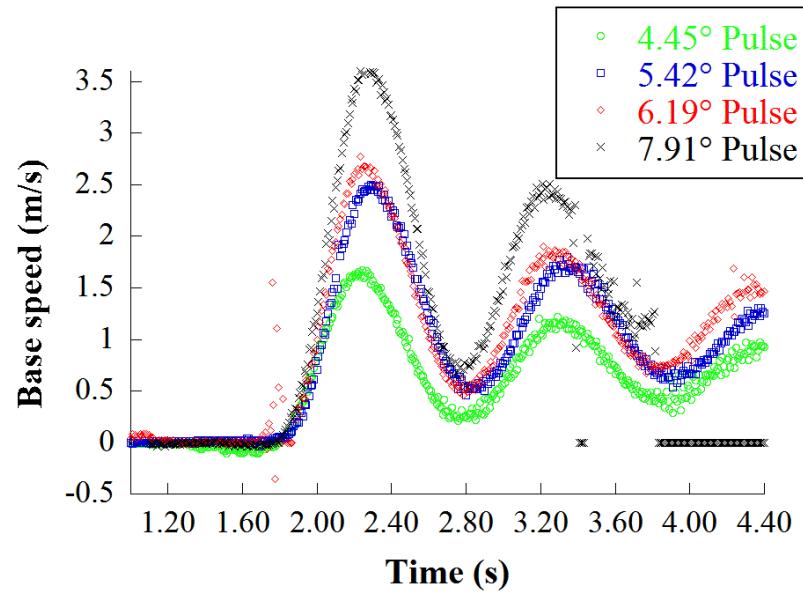
Figure 3.21: Speed response of a loaded i2 Segway to a force input.

49
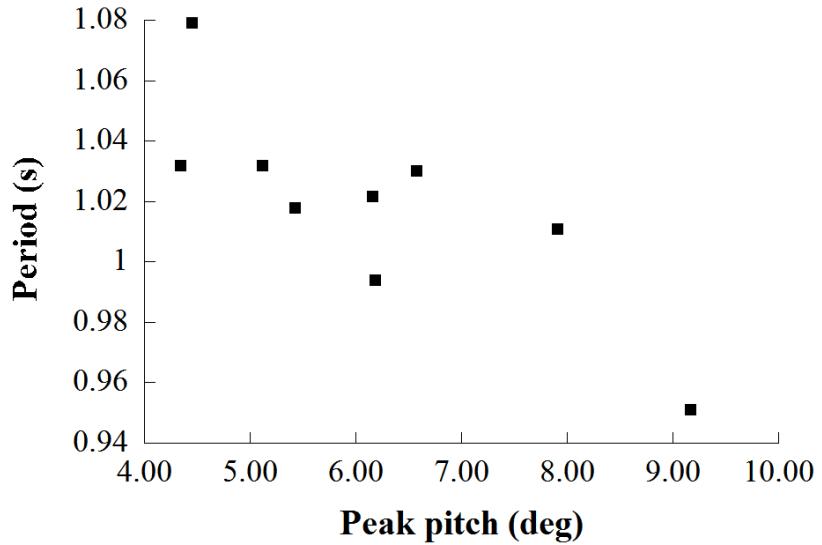
Figure 3.22: Period vs. Pitch amplitude - loaded i2 Segway.

The damping ratio does not show any clear trend with respect to the peak angle. This is shown in Figure 3.23. Most values lie between 0.08 and 0.012, except for the two cases related with the lowest pitch angles. However, these values do indicate that the Segway and rider will have a lightly damped multipeak response to a disturbance. Such responses indicate significant oscillatory behavior that is unsettling to the operator.
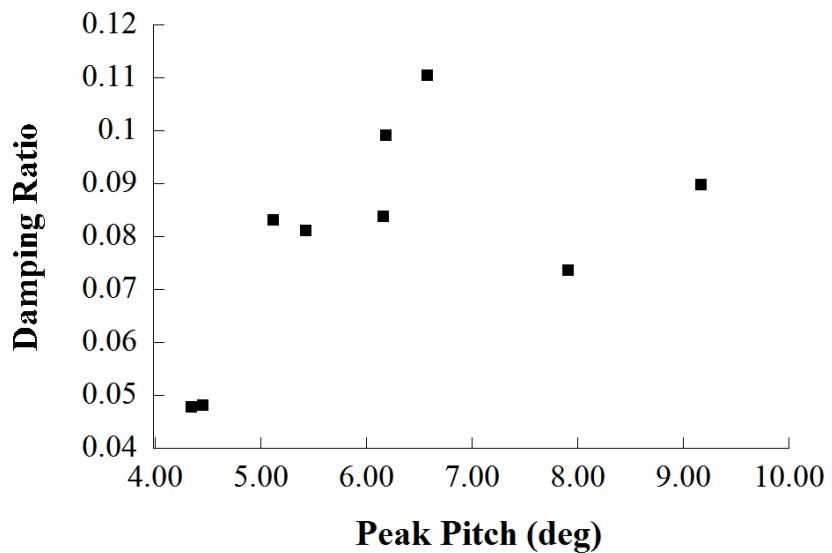
Figure 3.23: Damping ratio vs. Pitch amplitude - loaded i2 Segway.

The peak speed for different pitch angles is shown in Figure 3.24. Here it is seen that the that the first local maximum of the speed response increases with the maximum pitch angle. The increase rate seems to slow down at higher pitch angles.
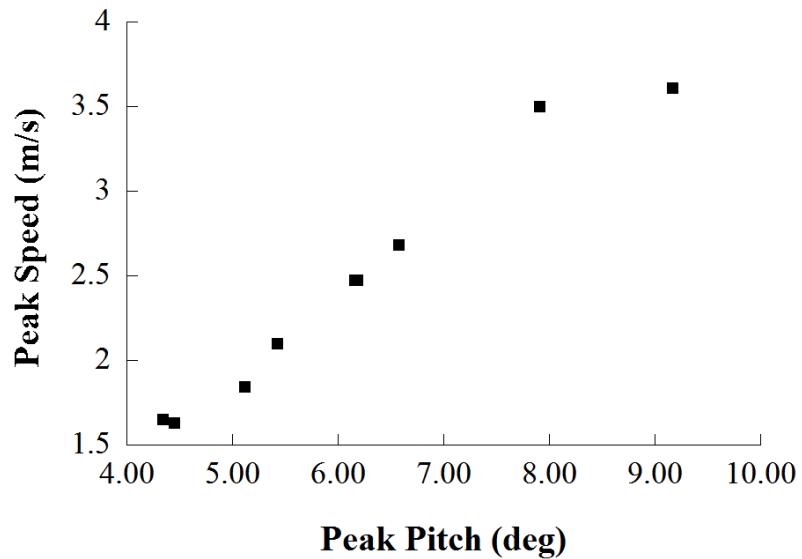
Figure 3.24: Peak speed vs Pitch amplitude - Loaded i2 Segway.

3.2.3 Manual impulse on Segway i2 - reactive user

An "impulse" force was manually applied on the back of the rider. Both the pitch angle and the speed of the Segway base were recorded. Two representative responses with different characteristics are examined here. In the first case, shown in Figure 3.25, the operator attempted to resist the motion and bring the vehicle to rest. The figure shows how initially the pitch angle and speed increase. Shortly afterward, the pitch angles decreases very suddenly to around -10° (with a negative overshoot to near -13°) and stays constant for nearly one second. This illustrates an important fundamental property - the base of the machine must accelerate forward and get out in front of the center of gravity so that the system pitches backward and can be decelerated back to zero velocity. During the time when the pitch angle remains negative, the speed of the vehicle decreases and goes negative to almost -1 m/s. At this point, the system reacts to the change in movement direction, and leans forward to increase the pitch angle so that the speed increases again. The system continues to compensate for this until it is able to stop. It takes around 2.5 seconds to do so. Note that these forward and backward pitch movements are partially induced by the Segway feedback controller and partially from the human rider. One of the significant challenges in analyzing the dynamics (and designing such vehicles) is to estimate what the human will do in all the possible conditions.

In the previous case, the user attempted to stop the vehicle aggressively, and their dynamics complicated the response. Therefore, the test was repeated with the operator reacting as passively as possible without falling of the vehicle. In the second case, shown in Figure 3.26, the user was able to stop the vehicle without producing a negative speed overshoot. Additionally, he decreased the time it took him to do so. Similarly to the previous case, the system reacted to the applied force and initial movement of the vehicle by tilting it backwards. The maximum negative pitch was very similar to the previous case. However, in this case, it did not keep the negative
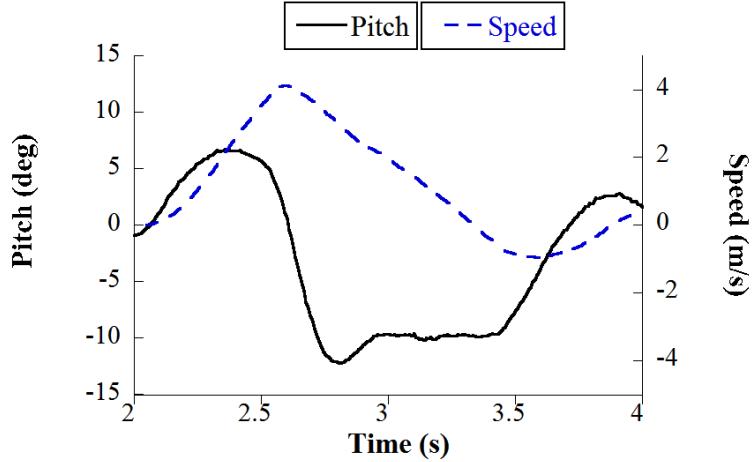
Figure 3.25: Active user resisting motion response - case 1.

pitch constant at -10°. Instead, it increased slowly back towards 0°. This allowed the vehicle to return to rest with very little negative speed overshoot, and in less time.
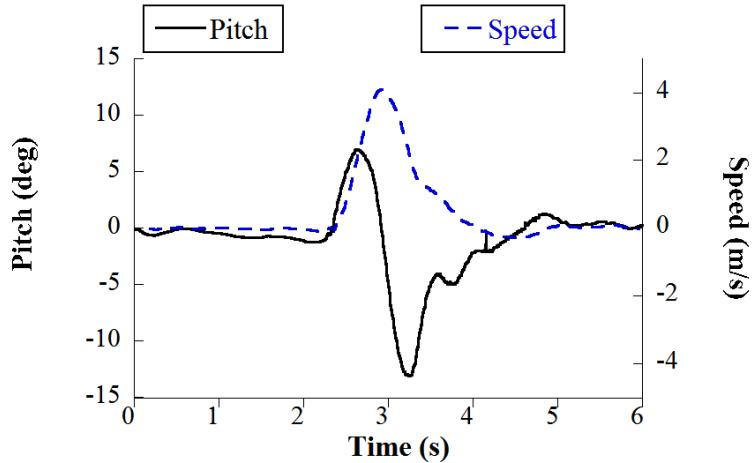
Figure 3.26: Active user resisting motion response - case 2.

3.2.4   Weight dropping tests-relaxed operator i2

The previous impulse tests used an unknown input force. To provide more certainty to the input and produce more of a "pulse" input, dropping weights were used to apply forces. Initially the user kept the Segway at rest, without exerting any forces and standing up straight. The rope was also relaxed so that the force would be applied on the Segway only after the weights had fell some distance. At the moment

53

when the force begins to be applied on the Segway handlebar, the Segway first tilts forward before speeding up. As it tilts, it pulls the user's arms, and it is impossible for him not to change his elbow angle and damp some of the forces being exerted on him by the Segway. This causes him to change his relative position and orientation with respect to the Segway. As the Segway moves forward and runs out of space, the user reacts and changes his position to stop the vehicle. Under these circumstances, the rigid body-model of the human does not fully describe the system. Therefore, the dynamic responses of these tests do not share the characteristics of a stabilized rigid inverted pendulum.

Figure 3.27 shows a sample pitch response, as well as the force exerted on the Segway's handlebar by the rope. The speed response is shown in Figure 3.28. As was mentioned before, the pitch curve does not share the characteristics of a linearly under damped response. In a stabilized rigid inverted pendulum the speed response would look more similar to the ones obtained from the manual pulse tests, where the user could passively be driven by the vehicle without the risk of an accident because the applied forces were smaller. In this case, the user movements are difficult to characterize because they were not voluntary.

3.2.5 Weight dropping tests-tense operator i2

In contrast with the previous case, here the user would lean backwards right from the start to resist movement. Because of this, the Segway also tilted backwards, and tensed the rope. Once the weight support was released, the rope transmitted the force to the Segway faster. The force applied and the pitch response are shown in Figure 3.29. Figure 3.30 shows the resulting speed response.

In this case, there was a considerably less relative motion between the user and the vehicle. This means that the rigid body model should have more validity than in
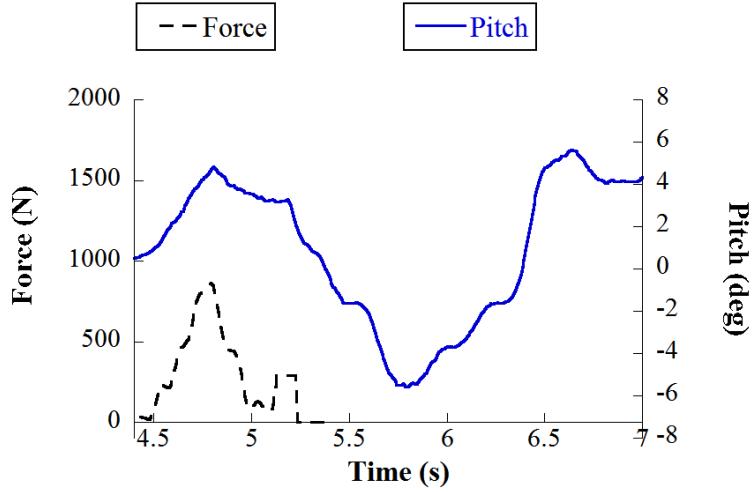
Figure 3.27: Pulse test pitch response - relaxed operator on a Segway i2.
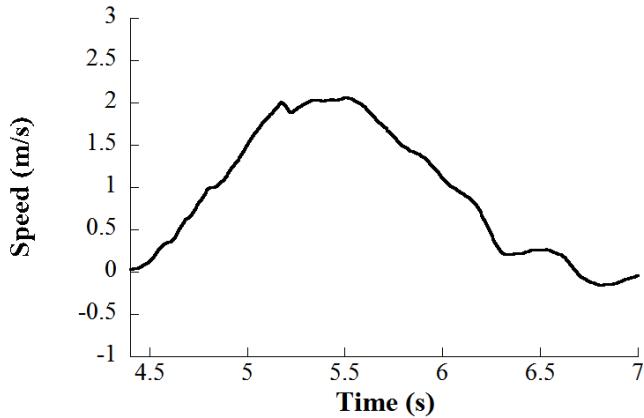
Figure 3.28: Pulse test speed response - relaxed operator on a Segway i2.

the relaxed operator case. However, because the user was leaning backwards, this test produced data corresponding to a breaking motion. The posture of the rider makes the effective center of mass of the system move backwards and affects its inertia. In Figure 3.29 a second frequency component can be observed. This could have been caused by the characteristics of the force being applied or the flexible nature of the machine/human connection.

The speed response is considerably different from the manual tests. In this case, after the pulse of force is applied, the vehicle decelerates until the end of the experiment. If the user stood straight, the system speed would have settled towards a constant value.
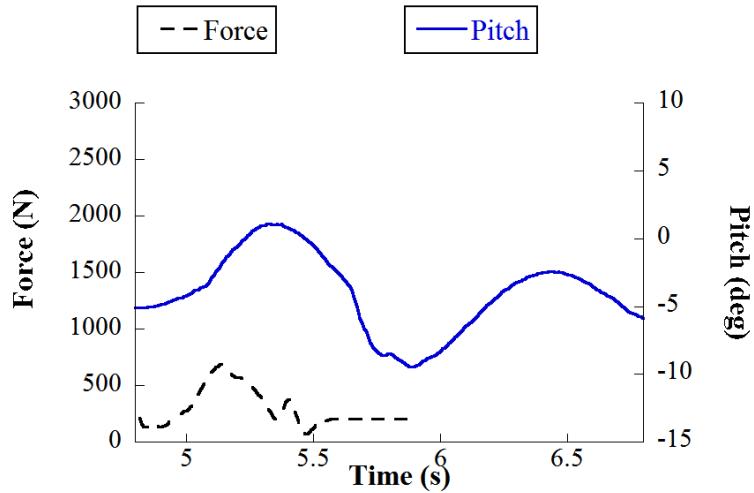
Figure 3.29: Pulse test pitch response - tense operator on a Segway i2.
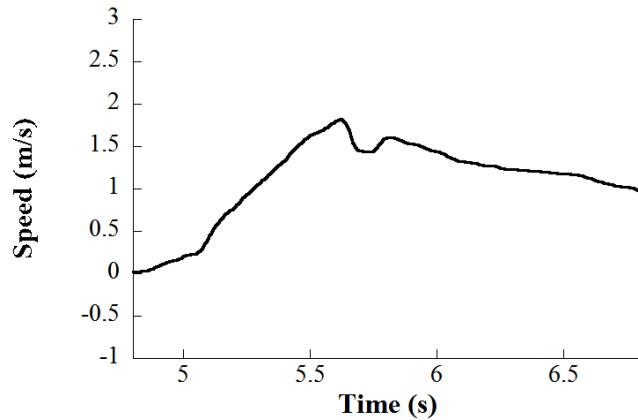
Figure 3.30: Pulse test speed response - tense operator on a Segway i2.

56

3.2.6 User lean on a Segway i2

Figure 3.31 shows the pitch angle and speed response of the Segway as the user leaned forward to accelerate. Initially, both the pitch and the speed decreased below their equilibrium values. When the user started to lean forward, the initial reaction of the vehicle was to tilt and move backwards so that the global center of mass remained at the same position. This is the expected behavior of any system without significant external forces being applied. In this case, the motor torques were very small at the beginning, because the torque input depends on the pitch angle error, which was initially small. However, as the Segway started to fall forward, the controller response increased, and the vehicle started moving forward to decrease the pitch error.

The opposite occurred when the person leaned backward in order to stop accelerating. As this action was performed the vehicle compensated by initially tilting forward. Finally, the motor torques became large enough to balance the system and reduce the speed to decrease the pitch angle error.
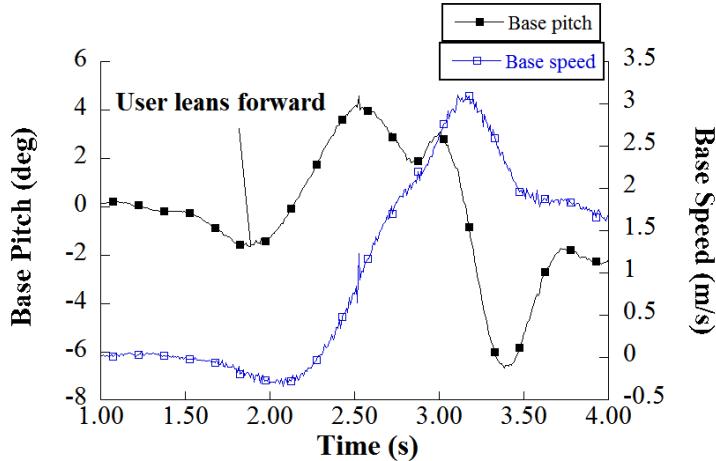
Figure 3.31: Pitch and speed response- i2 Segway with active user.

Figure 3.32 shows the pitch response for two user lean tests. Each test is identified by the maximum pitch it reached. Both responses can be divided into several phases. First, the vehicle tilted back when the user leaned forward. Following, the vehicle

started to fall forward, as is noted by the increasing pitch angle. After it reached a maximum value, it dropped back to a smaller angle. In this phase the user was adjusting his desired speed. Then, when the user decided to lean back and stop the vehicle, there was a slight increase (forward tilting) in the pitch angle as a reaction. After that, it started to fall backwards, until the user attempted to bring it to rest and stay at a balanced position by moving his body as needed. Figure 3.33 shows the speed for the two cases in Figure 3.32.
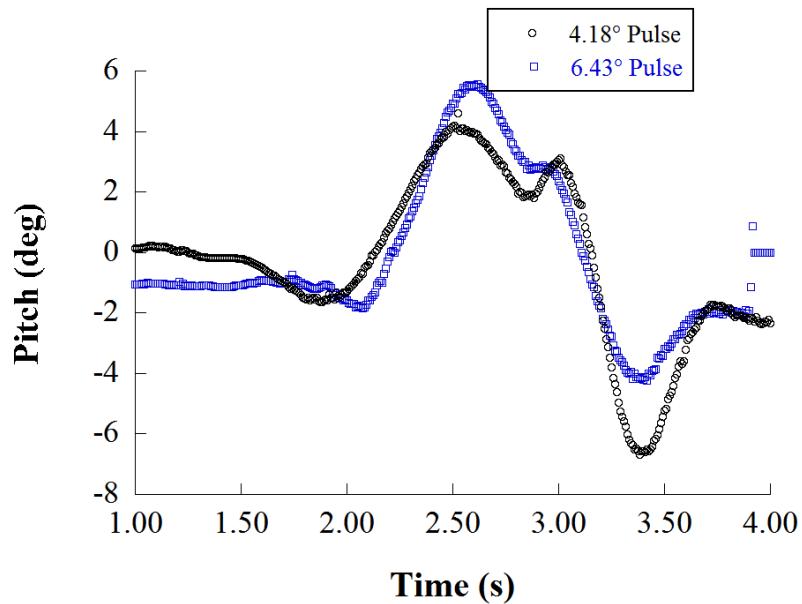
Figure 3.32: Pitch response - i2 Segway with active user.

It was observed from these graphs that the person is a very influential part of the control loop. In fact, the experiments when the user was just a passive element in the system showed that it oscillated significantly for some seconds. In this case the user motions are the control actions that can bring the system to a constant speed or to an absolute stop. The vehicle can reach a desired speed only if the human is an active part of the control loop.
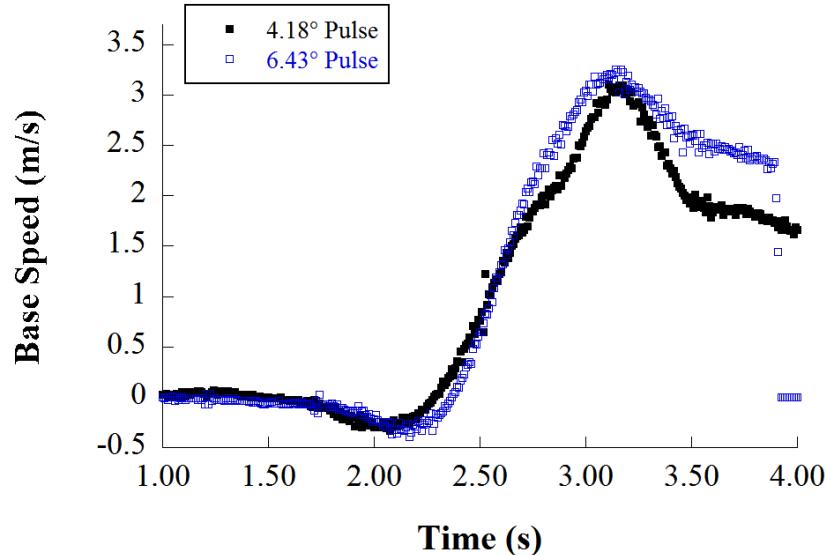
Figure 3.33: Speed response - i2 Segway with active user.

3.2.7 Turning tests at different speeds i2

In these tests the rider turned the handlebar at a fixed angle, and held that position for a period of time. This action is shown in Figure 3.34. This was done for various values of handlebar roll and the yaw turning rate of the Segway was measured. Figure 3.35 shows the handlebar roll angle and the resulting yaw rate of one experiment.

Figure 3.34: Spinning Test on a Segway i2.
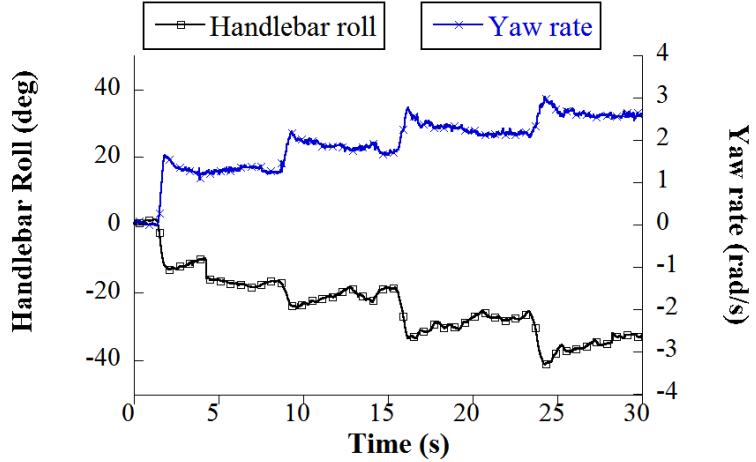
Figure 3.35: Turning rate at different handlebar roll inputs.

An average handlebar roll angle, as well as an average base yaw rate, were calculated from the intervals during which the operator attempted to keep the handlebar roll angle constant. Figure 3.36 shows the relationship between the yaw rate of the transporter and the roll angle of the handlebar. They increase in an almost linear relationship until a handlebar roll of about -0.5 rad, after which further tilting of the handlebar does not achieve a higher turning rate.
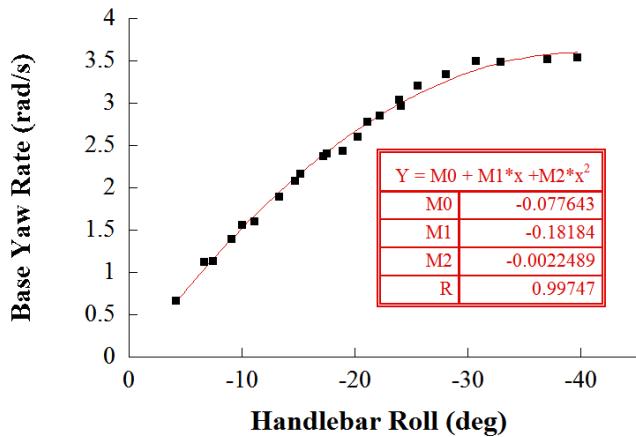
Figure 3.36: Turning rate vs handlebar roll angle - Segway i2.

3.2.8 Turning tests speed limit i2

In these tests, the operator rode the Segway at a certain speed and then turned suddenly. The purpose was to test if the Segway has a limit on its turning rate that avoids it from turning too fast at high that cause large centripetal accelerations which could cause the operator to fall off. The results of one experiment are shown in Figure 3.37. In this figure, the roll angle of the handlebar is the input command to the system. As the handlebar is tilted towards the left, increasing its roll angle, the turning rate increases. After a period of time, the handlebar roll angle is held constant which causes the yaw rate to remain almost constant.
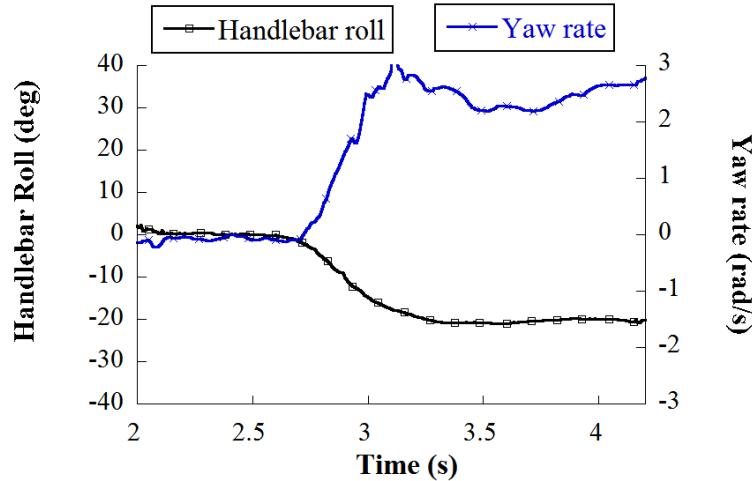
Figure 3.37: Handlebar roll angle and resulting yaw turning rate - Segway i2.

The process was repeated with different initial speeds. the rider attempted to keep constant for all the tests to make sure that the differences in the turning rate were only due to the initial speed. The results are shown in Figure 3.38. Figure 3.38 shows the turning rate at different speeds. There seems to be a small tendency of the turning rate to decrease as the speed increases, but it is not a strong correlation.
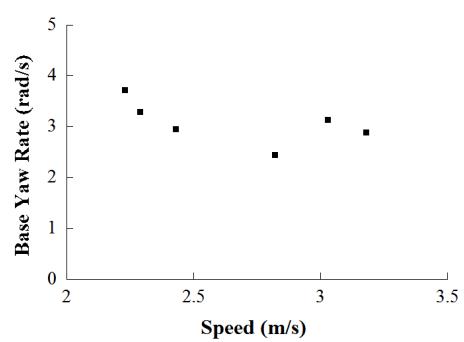
Figure 3.38: Base yaw rate at different initial speeds - full handlebar roll tilting.

3.2.9 Bump tests on a Segway i2

In these tests, the Segway was ridden over a brick. In one case the Segway was traveling at 1.5 m/s before hitting the block on the floor, and in the other, it was traveling at approximately 2 m/s. This was repeated several times for speeds near to those values.

Figure 3.39 shows the speed components of the Segway for the 2 m/s case. Shortly after 12 s, the Segway hit the bump. When the Segway started climbing over the bump, the speed in the horizontal (X) direction suddenly decreased slightly, while the speed in the lateral (Y) direction increased initially but then oscillates. This is an expected result from the right wheel climbing the brick while the left wheel continues traveling straight on the ground. There is also a small increase in the vertical (Z) speed of the vehicle. The reduction in the horizontal speed, and increases on the lateral and vertical speeds reach a maximum values simultaneously. Oscillation occurs in all speed components.
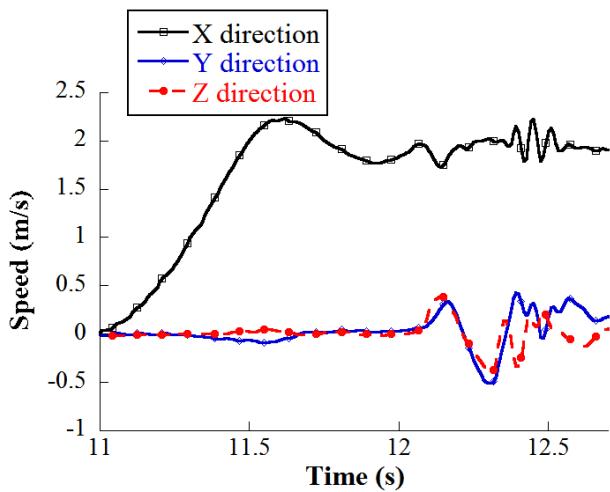
Figure 3.39: Medium speed travel over a brick - speed in x and y directions

Figure 3.40 shows the roll, pitch, and yaw angles of the Segway. As a result of the right wheel lifting off the ground, the Segway tilted towards the left. This explains the sudden decrease in the roll angle. As the right wheel climbed over the brick, the

left wheel continued to travel in contact with the ground. This makes the Segway's left wheel to move more distance in the XY plane than the right wheel. Therefore, the Segway turns towards the right, which is indicated by the decrease in the yaw angle.

Before the Segway traveled across the bump, the pitch angle can be seen to oscillate in Figure 3.40. This oscillation stopped at the same time when the disturbances in the roll and yaw angles were observed and resumes with a higher frequency after the Segway has crossed the bump. The initial oscillations are due to the rider attempting to reach a constant speed before crossing the obstacle. The period during which the obstacle is crossed takes around 0.2 s, which is a very small time for the user to actuate on the pitch angle. Towards the end, the oscillations are related to the instability of the Segway's right wheel while it is recovering traction with the ground. Oscillations at the same frequency were also observed in the X and Y speeds.
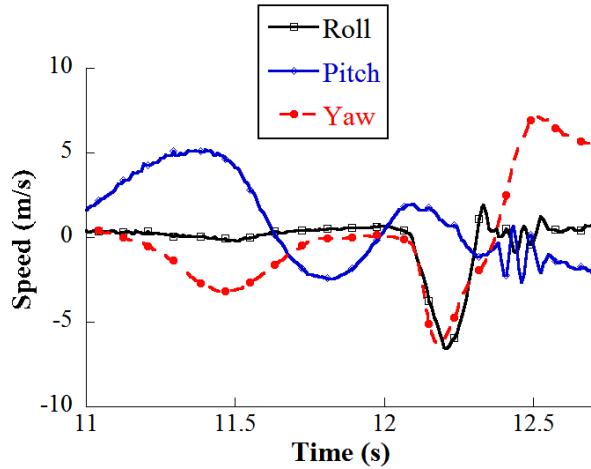
Figure 3.40: Medium speed travel over a brick - roll, pitch and yaw angles

Figure 3.41 shows the maximum roll angle of the Segway after crossing the brick. From the graph, it does not appear that the speed have an effect on how much the Segway tilts.
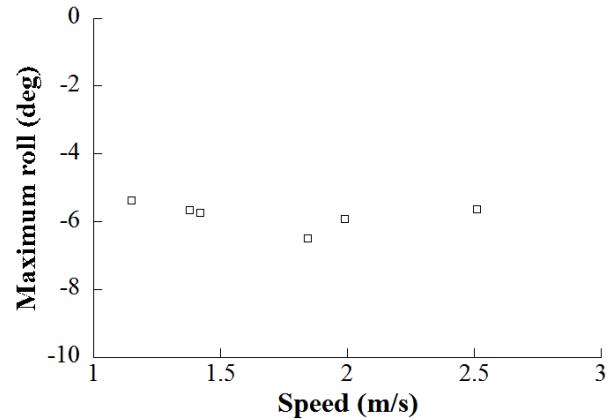
Figure 3.41: Maximum roll angle after crossing obstacle at different speeds.

3.3 Segway i167 tests results

The same experiments, except the bump tests, were carried out using a Segway i167, shown in Figure 3.42.

.

Figure 3.42: Segway i167.

3.3.1 Manual impulse on an unloaded Segway i167

Impulse response tests were carried out on a Segway i167 without a rider. The Segway i167 model has three settings that are enabled using different keys. The difference between the three settings is that the black key has the lowest speed limit; while the red key has the highest, and the yellow key has a speed limit in between those two.

The red key pitch angle manual "impulse" response is plotted in Figure 3.43 and the speed response is shown in Figure 3.44. The pitch response shows that the system's response is close to a linearly under damped response. The speed converges to a positive slope line as the pitch angle settles to zero, similar to the results observed in the i2 Segway tests. Also, the speed is higher with a higher initial pitch response (larger applied impulse). For a peak pitch range from 4.68° to 11.98°, the initial peak speed varied from 1.37 m/s to 2.95 m/s.
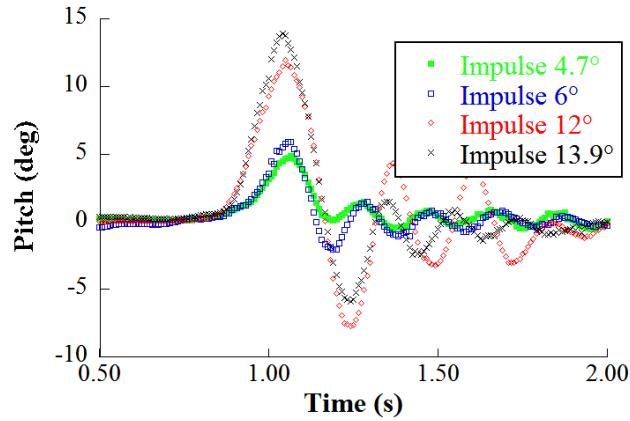
Figure 3.43: Pitch Responses - Red Key.
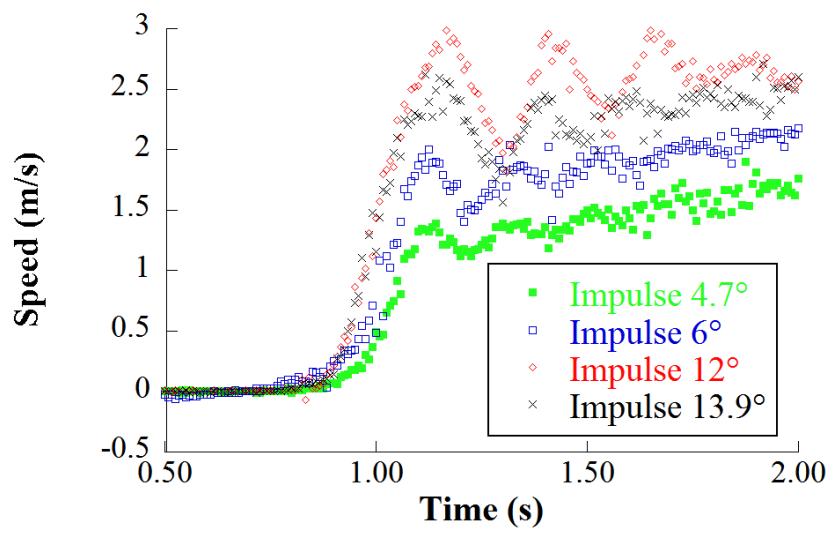
Figure 3.44: Pitch Responses - Red Key.

The pitch response for the medium-speed setting (yellow key) is shown in Figure 3.3.1. The frequencies are very similar for all three cases but it was noticed that at higher pulse magnitudes, the settling point of the angle decreases. The speed response is shown in Figure 3.46. It shows very similar responses for the three cases.

.
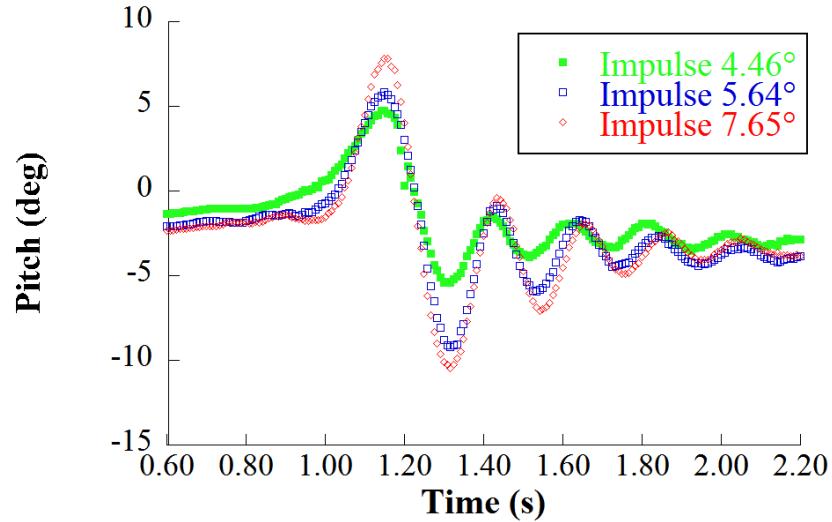
Figure 3.45: Pitch Responses - Yellow Key.
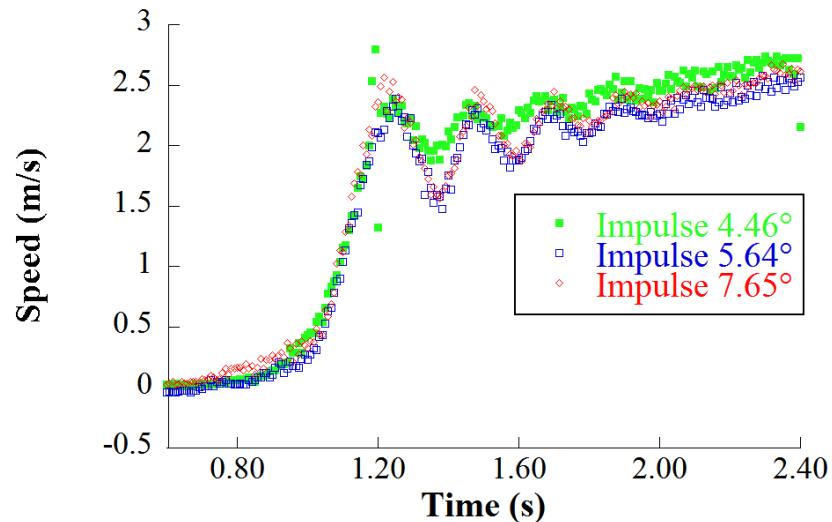
Figure 3.46: Speed Responses - Yellow Key.

The pitch response using the black key is shown in Figure 3.47. The speed response is shown in Figure 3.48. The initial peak speed range varied from 1.82 m/s to 2.65 m/s, and the peak pitch range was from 3.22° to 13.1°. This speed range is smaller than the one obtained in the red key case but larger than the yellow key case. In this case, the negative settling angle is more evident and the periods are larger than in the yellow and red key responses. Note that as a harder pulse is applied to the Segway, the settling pitch is lower.
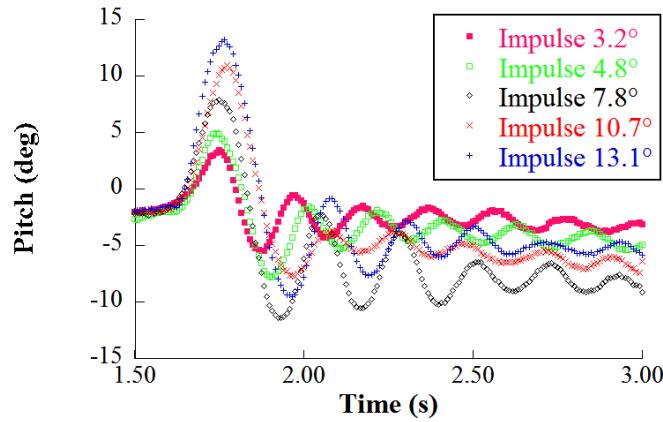
Figure 3.47: Pitch Responses - Black Key.
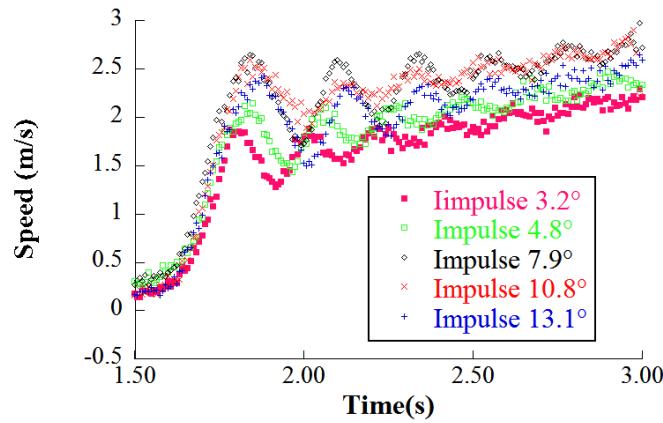
Figure 3.48: Speed Responses - Black Key.

The response properties were compared for all three keys. Figure 3.49 shows the oscillation periods for various peak angles using the different keys. The yellow and red keys do not show any clear tendency on how the period changes with increasing the

initial pitch maximum. However, as in the Segway i2 tests, that the period increases with bigger impulses when the black key is used.

Note that the Segway i167 oscillated with a wide range of frequencies for the same maximum pitch. While in Figure 3.15 the period could be found between 0.25 and 0.5 s, in this case, the periods went as low as 0.15 s, but above 0.4 s.
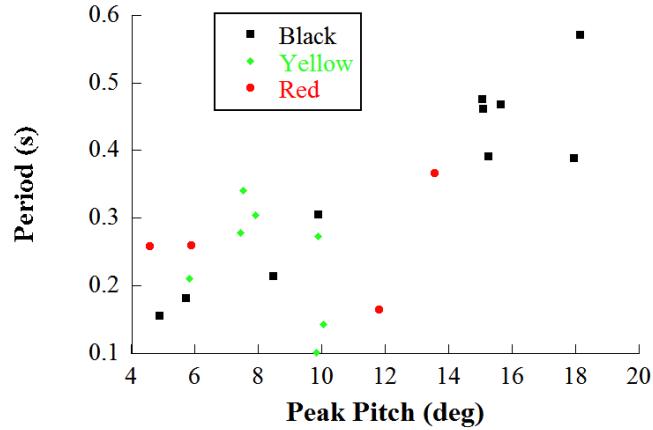
Figure 3.49: Damped Periods.

Figure 3.50 show that the damping ratio increases with increasing impulse amplitude. The black key produced significantly lower damping ratios than the yellow and red keys. However, as the impulse amplitude increases, the measurement of the damping ratio becomes less significant, because the damping ratio calculation comes from a linear approximation of the response. In contrast with the Segway i2 results, the damping ratio does exhibit an increasing trend with respect to the maximum angle of the pitch response.
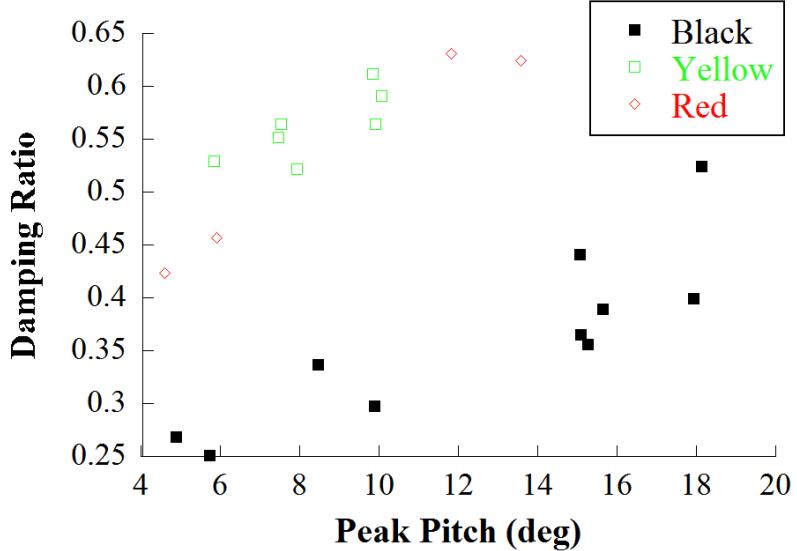
Figure 3.50: Damping Ratios.

Figure 3.51 shows the initial maximum speed for different impulse sizes. The yellow key produces a higher peak speed than the black key. However, the red key achieved the highest speed of all. The peak speed increases up to an angle value close to 12°, after which it does not increase any further. This differs from the Segway i2 experiments, where the speed kept increasing for cases above maximum pitch of 12°. In fact, the Segway i2 reached greater speeds than those of the Segway i167 experiment, regardless of the key that was being used.

.

Figure 3.52 shows the approximate acceleration about which the speed response oscillates as it settles over time. There is not a clear trend with respect to the maximum pitch. The red key was able to reach a very high acceleration in one case. Compared to the Segway i2 experiments, the Segway i167 exhibited greater accelerations, regardless of which key was being used.

These results reveal an important difference in how the two Segways limit their speed. The Segway i2 limits its speed by not allowing it to increase beyond a specified speed limit. While the speed stays below that value, the Segway i2 does not try to

71
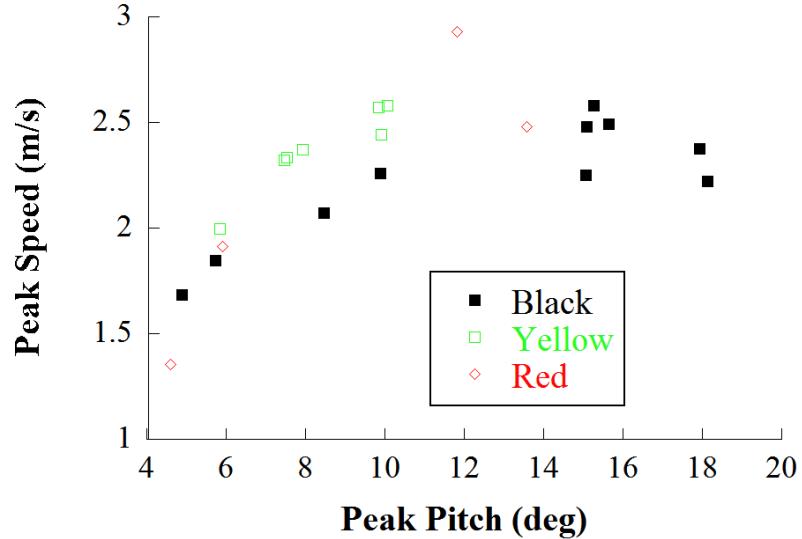
Figure 3.51: Peak Speed.

limit the speed in any sense. The Segway i167, on the other hand, exhibit different dynamics according to the key being used. This is revealed by the results that show it settles at a constant non-zero acceleration, but at different steady-state speeds.
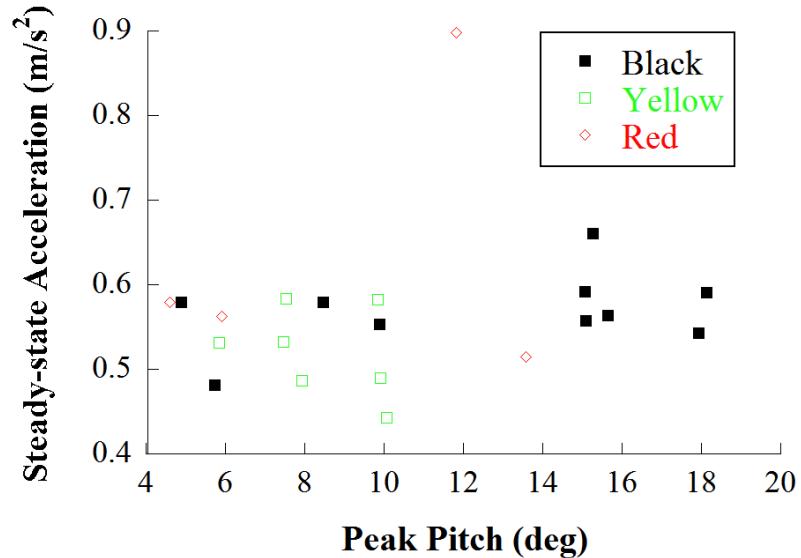
Figure 3.52: Steady-State Acceleration.

3.3.2 Manual impulse on a loaded Segway i167 - static user

The results obtained from the loaded Segway i167 response are very similar to the i2 Segway experiment results. The pitch angle response is shown in Figure 3.53. There is some noise in the measurements as seen in the figure, that occurred when the markers on the Segway got close to the workspace limits of the motion capture system. Figure 3.54 shows the speed responses.
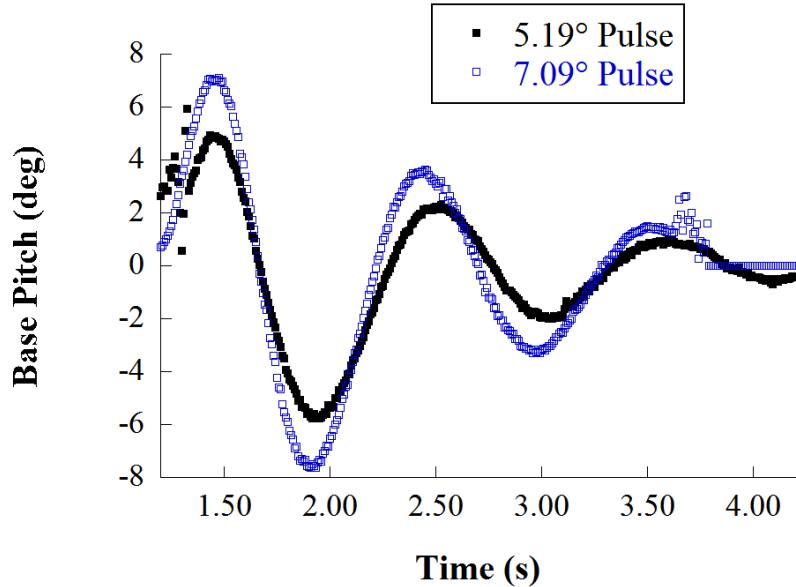
Figure 3.53: Pitch Response - loaded i167 Segway

Figure 3.55 shows the oscillation period for different amplitudes. The range over which the period varies is similar to the i2 loaded range. It also shows, as in the Segway i2 case, that the period decreases with an increasing pitch angle. However, it must be noted that in both cases, the range over which the period changes is too small.

Figure 3.56 shows the damping ratio for different pitch angles. In this case the damping decreases as the pitch angle increases, in contrast with the Segway i2 experiment. However, it must be noted that the range over with the damping varies is too small to consider this as a general rule. In this case, the damping is above 0.1 for the

73
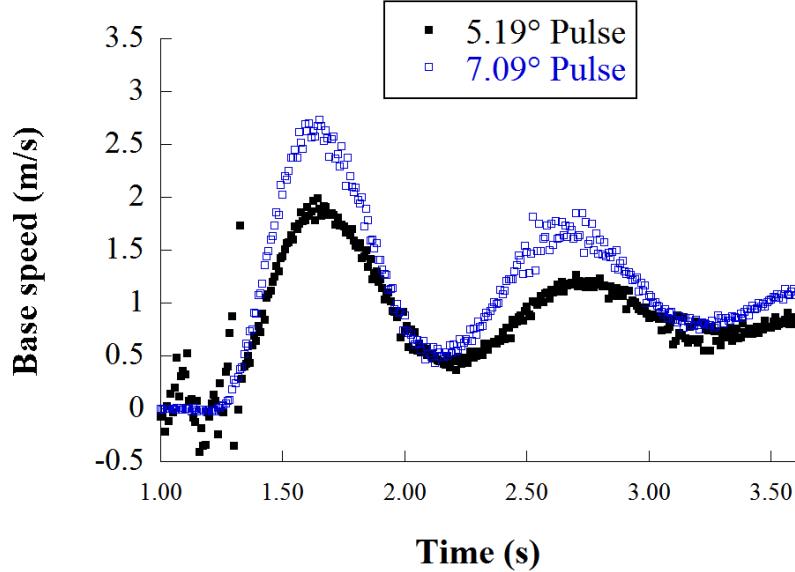
Figure 3.54: Speed response - loaded i167 Segway.

5° to 8° range, while for the same range in the Segway i2, the damping varied from 0.08 to 0.11.

Figure 3.57 shows the speed overshoot for different maximum pitch angles. This speed increases with an increasing pitch angle, which is a similar behavior to the one observed with the Segway i2. The maximum speeds are also similar for both Segways models.

3.3.3 Manual impulse on a Segway i167 - reactive user

Figure 3.58 shows the pitch angle response of a Segway-rider system after being pushed on the back with an "impulse". The speed response is shown in Figure 3.59. The 5.63° maximum pitch case resembles the Segway i2 case shown in Figure 3.25. In both cases there was an initial increase in the pitch angle and then a sudden reduction until a minimum was reached. Afterward, the pitch angle started increasing slowly for a while, which is slightly different from the i2 case, where the pitch angle was maintained constant for a period. Then, the pitch increased until it reached another maximum, and then settles down to zero. The similarities are more pronounced in
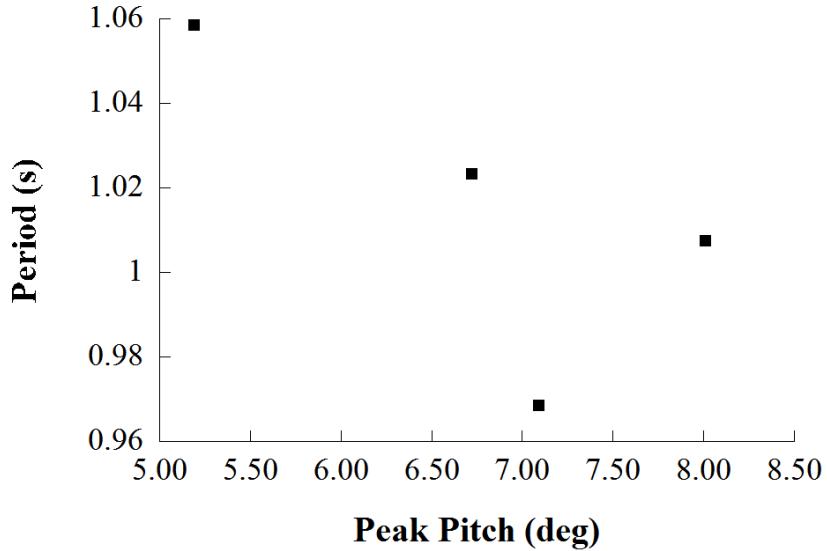
Figure 3.55: Period vs. Pitch amplitude - loaded i167 Segway.

the speed response, where both the i2 case mentioned above and the 5.63° i167 case have similar shapes.

The 7.4° case exhibits a different behavior from the two i2 cases studied before, as well as the 5.63° case just discussed. This is evidence of the numerous ways the user can act to stop the Segway. The main difference that the 7.4° case exhibits is that after reaching the maximum pitch, the pitch does not decrease directly towards a minimum negative value, but instead, decreases for a while, then stays constant for around 0.2 seconds, and then continues decreasing towards a minimum pitch angle. This indicates that the initial leaning back insufficiently, in order to stop the Segway within the space available. The user had to lean further back after noticing that the initial lean was insufficient. This appears in the speed response when the speed decreased after reaching the maximum speed first to a speed, and then at a faster rate. In this case, it also took more time to stop the Segway.

In these experiments, the user took around 2 seconds to bring the Segway i167 to a stop, which is less than the 2.5 seconds it had taken him to stop the Segway i2.

75
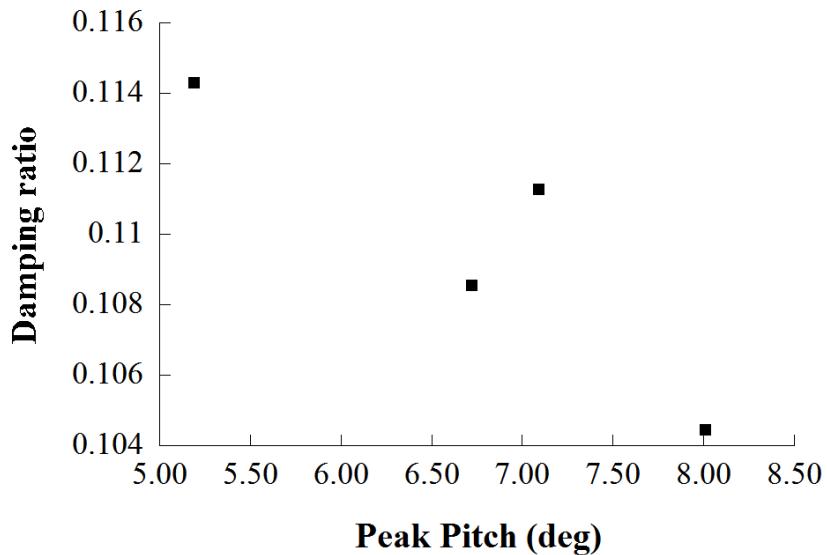
Figure 3.56: Damping Ratio vs. Pitch Amplitude - loaded i167

3.3.4 Weight dropping tests-relaxed operator i167

As in the Segway i2 tests, numerous dynamics effects in the response are due to voluntary or involuntary motions of the operator. Pitch responses of a "pulse" force applied on the Segway i167 being driven by a relaxed operator are shown in Figure 3.60. The speed response is shown in Figure 3.61. Contrary to the i2 tests, both pitch responses exhibit similar characteristics. They have an initial oscillation that extends for one cycle after which the pitch drops dramatically as the vehicle comes to a stop. This initial cycle is similar to the manual pushing experiments, except that its amplitude is smaller, and it exhibits a slightly smaller period of 0.8 s. Afterward, the pitch decreases towards a minimum value, then it settles in a smooth oscillation around 0°.

Compared to the Segway i2 relaxed operator experiments, the pitch response is smaller in this case; below 4°, compared to 8° on the Segway i2. There does not seem to be a significant difference in the force applied to account for this behavior, except possibly, the point at which it was applied. The speeds reached in both the Segway i167 and Segway i2 experiments are comparable.

76
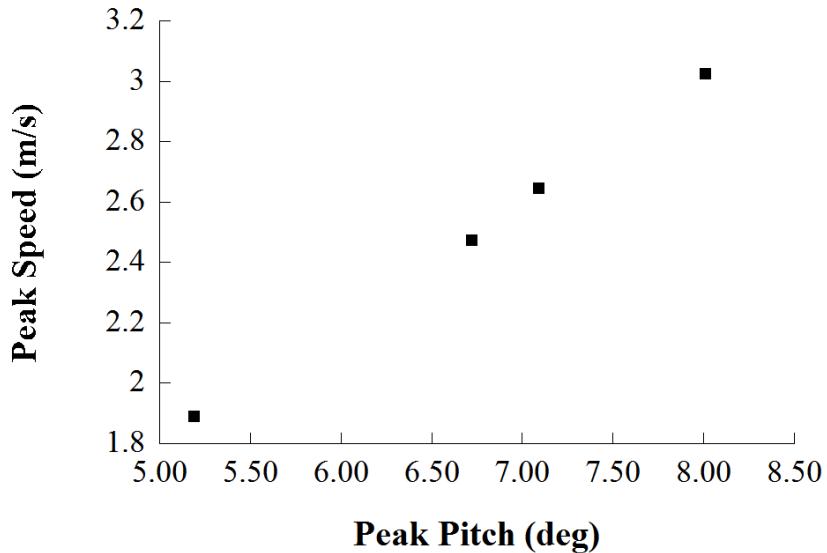
Figure 3.57: Peak speed vs. Pitch amplitude - loaded i167 Segway.

3.3.5   Weight dropping tests-tense operator i167

Figure 3.62 shows the pitch response of the Segway i167 with a tense rider to a pulse force. The speed response is shown in Figure 3.63. Initially, the speed increased while the force was being applied. During this phase, the human body can be regarded as a rigid body.

However, when the deceleration starts, there is a high frequency oscillation that can be noticed in the speed response. To some extent, this might be an indication of the operator controlling the deceleration rate. Initially, he leaned back to reduce the speed, but after noticing that he was stopping too quickly, he corrected his leaning to produce a smaller deceleration. This effect was also present in the Segway i2 tests.
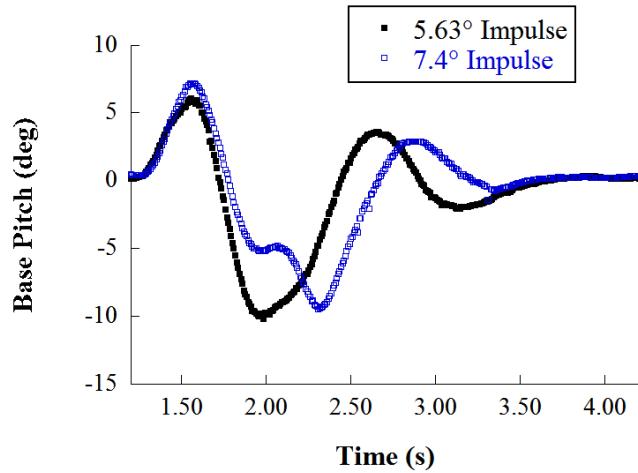
Figure 3.58: Active user resisting motion pitch response.
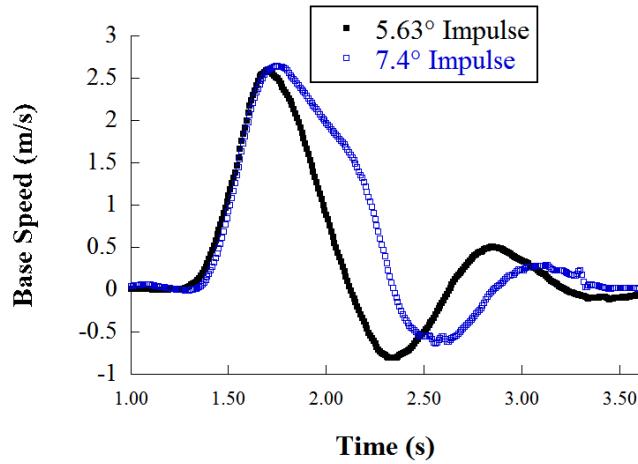
Figure 3.59: Active user resisting motion speed response.
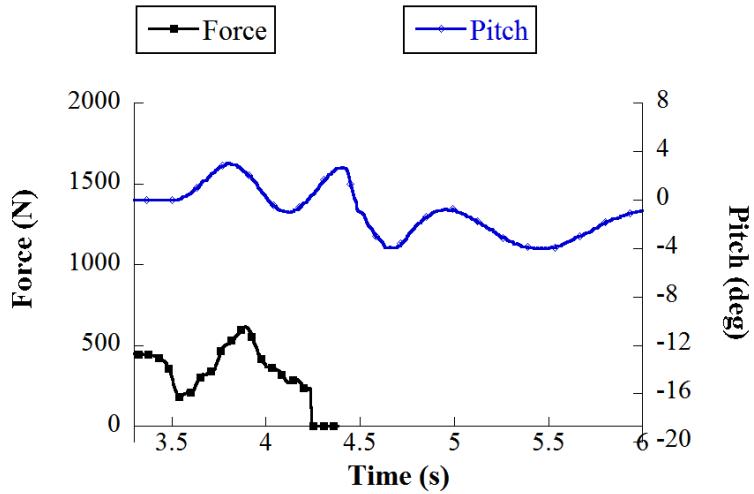
Figure 3.60: Pulse test pitch response - relaxed operator on a Segway i167.

78
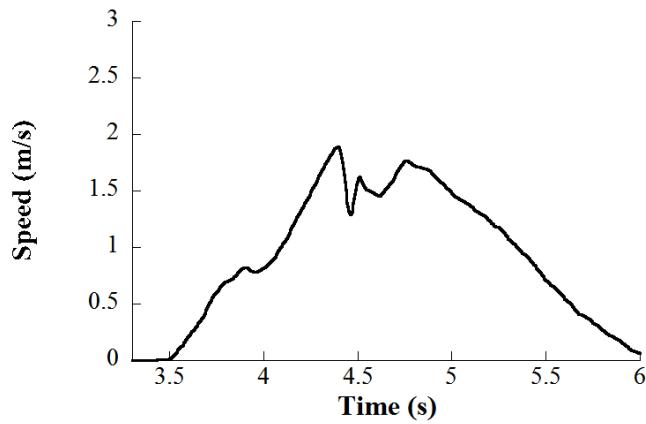
Figure 3.61: Pulse test speed response - relaxed operator on a Segway i167.
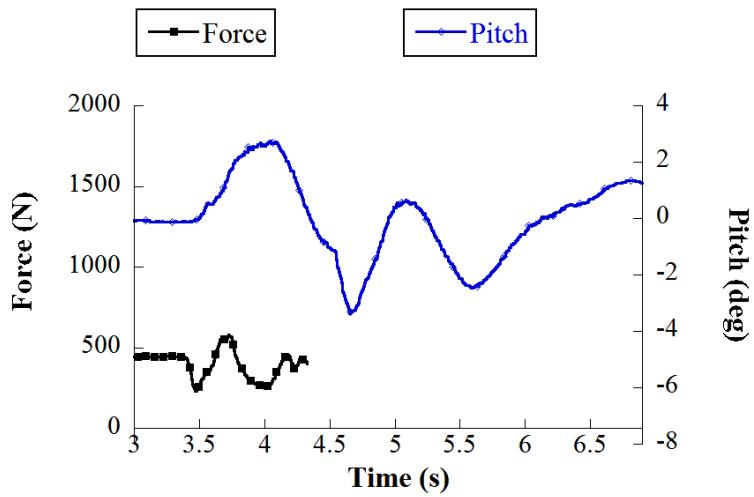
Figure 3.62: Pulse test pitch response - tense operator on a Segway i167
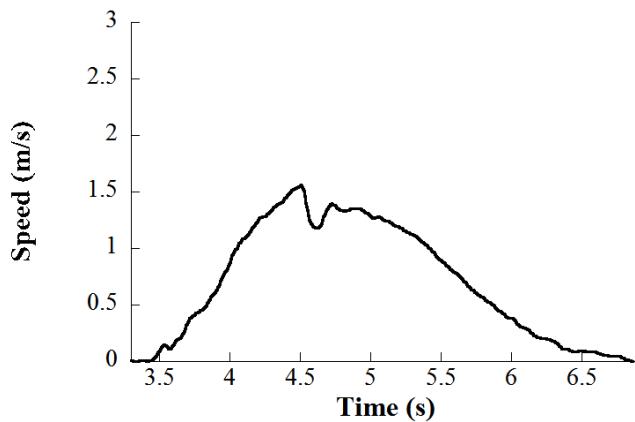
Figure 3.63: Pulse test speed response - tense operator on a Segway i167

3.3.6   i167 Segway no weight user pulse

Figure 3.64 shows the pitch and speed responses to a user motion intended to accelerate the Segway i167. Here, the deceleration phase was not recorded. This response is similar to the Segway i2 response in the initial reduction in the pitch angle as the user leans forward to start motion. Afterward, the user kept a constant speed by keeping the pitch angle near zero degrees. Figure 3.65 shows pitch angle responses for different user motion strengths.
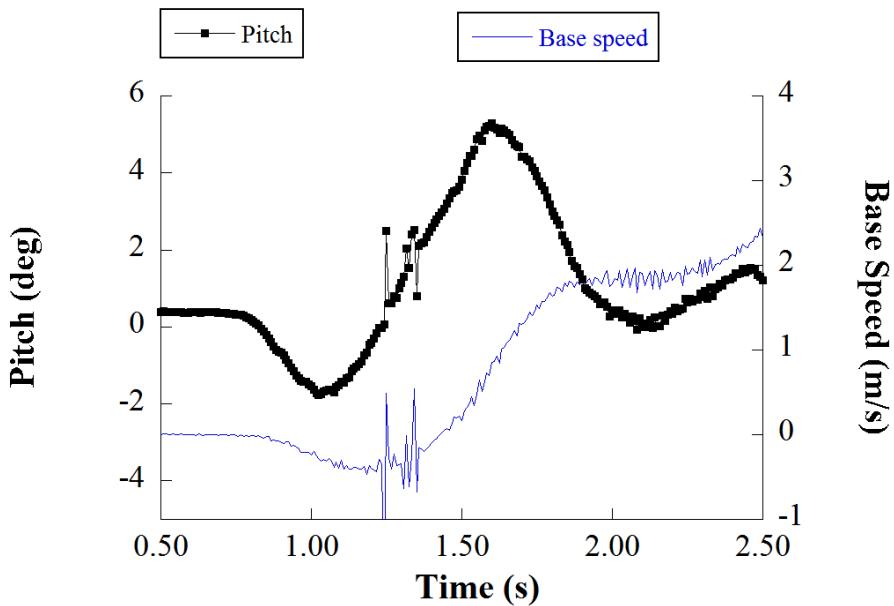
Figure 3.64: Pitch and speed response- i2 Segway with active user.

Figure 3.66 shows different speed responses for the same cases as in the pitch angle responses in Figure 3.65.Even though there is only one case significantly different from the rest, the 9.1° case, it shows how a stronger forward lean accomplishes a higher acceleration, and a larger initial back-tilting.

3.3.7   Turning tests at different speeds on a Segway i167

Figure 3.67 shows the response of the Segway as the grip on the right side of the handlebars is twisted. Comparing with the tilting of the handlebar in the Segway i2 case, the Segway i167 provides a more constant control of the turning rate. Figure 3.68
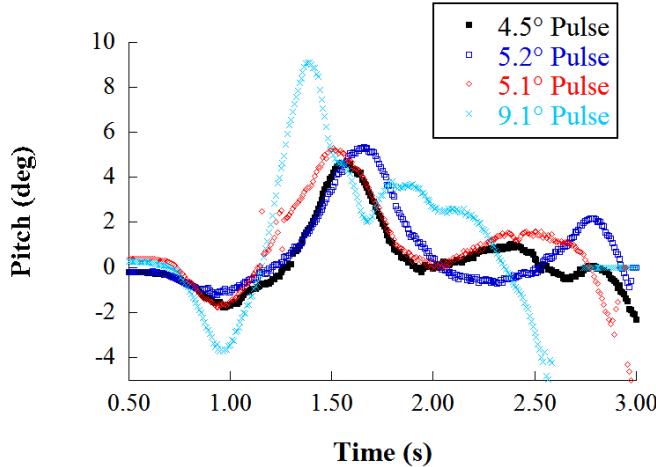
Figure 3.65: Pitch response - i167 Segway with active user.
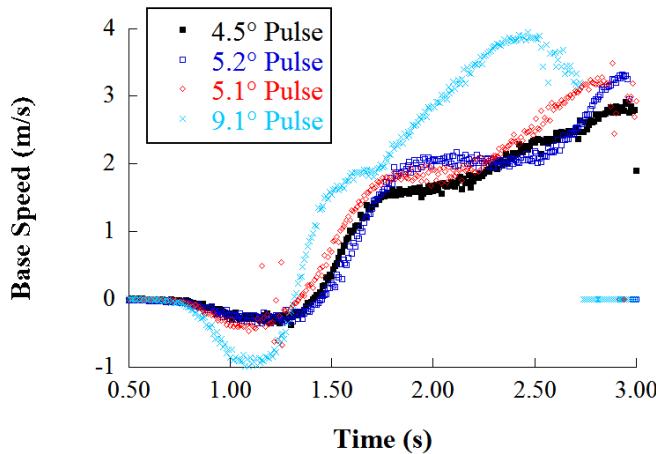
Figure 3.66: Speed response - i167 Segway with active user.

shows the relationship between the turning rate of the Segway and the rotation angle of the twisting grip. The Segway i167 has a lower turning rate limit, in comparison with the Segway i2.

3.3.8 Turning tests speed limit on a Segway i167

Figure 3.69 shows the results of a turning limit test. The twisting grip was turned completely and the resulting turning rate was recorded. Figure 3.70 shows the resulting turning rate at different initial speeds. This was repeated over a small range of initial speeds. In all cases, the resulting turning rate was very similar.
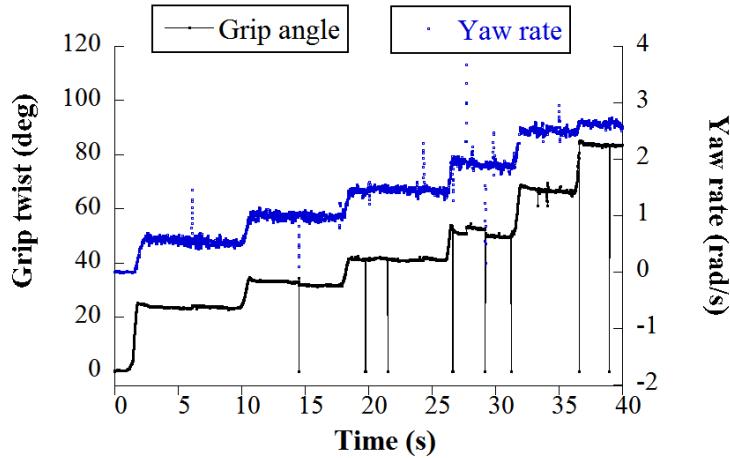
Figure 3.67: Turning rate at different grip twisting inputs.
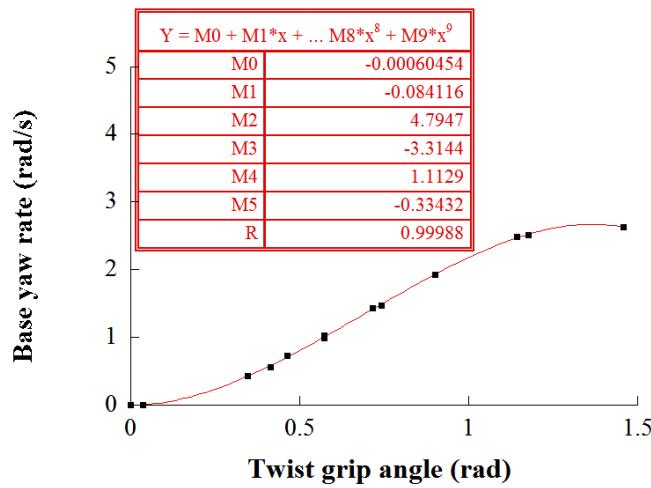
Figure 3.68: Turning rate vs handlebar roll angle - Segway i2.
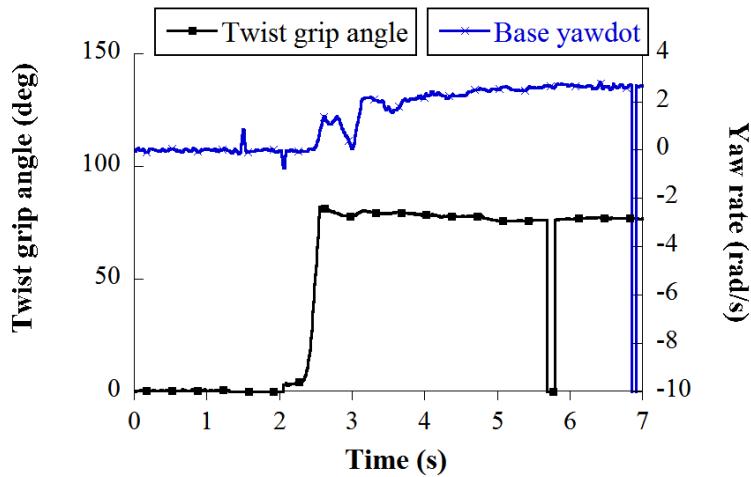
Figure 3.69: Handlebar roll angle and resulting yaw turning rate - Segway i167.

82
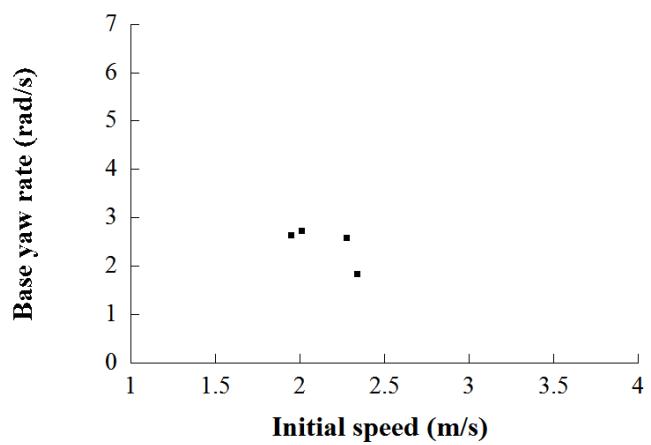
Figure 3.70: Base yaw rate at different initial speeds - full grip twisting.

CHAPTER IV

SIMULATION STUDIES

The first section of this chapter describes the process to develop a simulation of a TWIP with dynamic properties similar to those of a Segway carrying a human rider. The second section describes the simulation of different scenarios that could lead to a failure condition.

4.1 Dynamic properties

4.1.1 System parameters

In order to model the Segway personal transporter, it is necessary to obtain the physical properties of the system such as masses and inertias of the wheels and the base. The wheels were modeled as uniform-mass discs with diameter d_w and thickness w_w, as shown on the left side of Figure 4.1. The base was modeled as a rectangular prism with dimensions l_{pb} x w_{pb} x h_{pb}. The handlebar was modeled as an aluminum bar with length l_{ph}, outer diameter d_h and wall thickness of t_{ph}, with a point mass m_{pu} on its top. The mass m_{pu} has the effect of moving the location of the center of mass forward, similar to a real transporter. The geometry of these components are shown in Figure 4.1.

The mass moments of inertia of the base around its center of mass are given by:

$$I_{pbx} = \frac{1}{12} m_{pb} \left(w_{pb}^2 + h_{pb}^2 \right) \tag{4.1}$$

$$I_{pby} = \frac{1}{12} m_{pb} \left(h_{pb}^2 + l_{pb}^2 \right) \tag{4.2}$$

$$I_{pbz} = \frac{1}{12} m_{pb} \left(w_{pb}^2 + l_{pb}^2 \right) \tag{4.3}$$
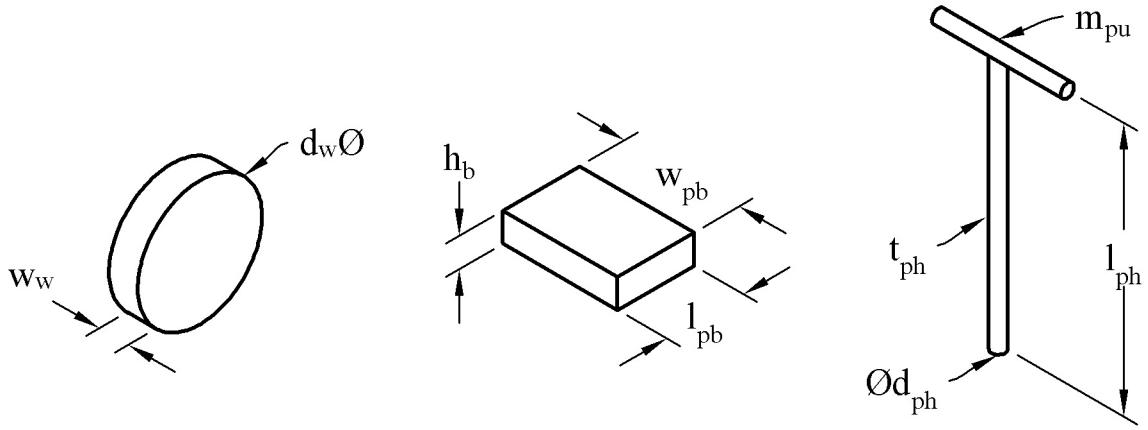
Figure 4.1: Base and wheel geometry

where m_b is the mass of the base. Meanwhile, the mass moments of inertia of the wheels are given by:

$$I_{wy} = \frac{1}{8}m_w d_w^2 \tag{4.4}$$

$$I_{wx} = I_{wz} = I_{xz} = \frac{1}{12}m_w \left(\frac{3}{4}d_w^2 + w_w^2\right) \tag{4.5}$$

where m_w is the mass of each wheel. The mass moments of inertia of the handlebar, not including the point mass m_u are given by

$$I_{phx} = I_{phy} = \frac{1}{12}m_{ph}\left[3\left(r_1^2 + r_2^2\right) + l_{ph}^2\right] \tag{4.6}$$

$$I_{phz} = \frac{1}{2}m_{ph}\left(r_1^2 + r_2^2\right) \tag{4.7}$$

where m_h is the mass of the handlebar and r_1 and r_2 are its inner and outer radii.

The approximate values of the masses and dimensions used to calculate the inertias are shown in Table 4.1.

The base, handlebar, and the upper point mass were combined into one body in order to speed up simulation time. This body's moments of inertia around its center of mass are given by I_{px}, I_{py}, I_{pz} with its center of mass located on the *(x,z)* plane at

Table 4.1: Estimated parameters of the components of the Segway.

Parameter	Value
m_{pb}	37 kg
m_w	4.5 kg
m_{ph}	0.489 kg
m_{pu}	0.5 kg
l_{pb}	0.65 m
w_{pb}	0.43 m
h_{pb}	0.2 m
d_w	0.4826 m
w_w	0.1 m
t_{ph}	$2 \cdot 10^{-3}$m
l_{ph}	1.1 m
d_{ph}	0.0508 m

point (x_p, z_p). Table 4.1.1 shows the resulting moments of inertia and the location of the center of mass of the base-handlebar assembly.

Table 4.2: Estimated parameters of the Segway.

Parameter	Value
I_{px}	1.67 kg·m^2
I_{py}	2.63 kg·m^2
I_{pz}	2.48 kg·m^2
I_{wx}	0.0693 kg·m^2
I_{wy}	0.131 kg·m^2
I_{wz}	0.0693 kg·m^2
x_p	0.0067 m
z_p	0.0171 m

Table 4.3 shows the estimated parameters of the human rider. The mass of the person riding the Segway, m_b, was known to be 85 kg. An average center of gravity for adult subjects with similar body type was found in the report *Moments of Inertia and Centers of Gravity of the Living Human Body* done by the U.S Air Force in 1964 [2]. Approximate inertia properties were extracted from the report *Moments of Investigation of the Inertial Properties of the Human Body* from 1975 [1]. The moments of inertia around the x, y, and z axes are I_{bx}, I_{by}, *and* I_{bz}. The height of the center of mass of the person from the floor is z_{wb}.

Finally, the location of the center of mass of the person in the x direction with respect to the axes of the Segway wheels was calculated so that the global center of mass of the Segway-person system was located directly over the wheel axes.

Table 4.3: Initial estimates of the human body parameters.

Parameter	Value
m_{b}	85 kg
I_{bx}	12.558 kg·m^2
I_{by}	15.0886 kg·m^2
I_{bz}	1.7424 kg·m^2
x_{wb}	-0.00378 m
z_{wb}	1.072 m

4.1.2 MotionGenesis model

The TWIP human transporter was modeled using MotionGenesis. The MotionGenesis code produces a MATLAB script that contains the differential equations of motion. Input torques on each of the wheels are defined in the MATLAB script in terms of the dynamic variables and parameters. The structure of the code is as follows:

1. Body and frame definition: The base and both wheels were defined as three independent bodies. Two coordinate frames were defined, a global coordinate frame named 'N', and a frame named 'S' that rotates an angle β around the y axis of the global coordinate system, as described in chapter 2. This second frame, shown in Figure 4.2, simplified the process of defining the relative rotation between the wheels and the base. Each body definition includes a specific frame of reference for that body.

2. Parameter definition: Geometric dimensions, masses, and inertias around the center of mass of each component were defined.

3. Dynamic variables definition: The variable names of input torques, system speeds, accelerations, and forces were defined.
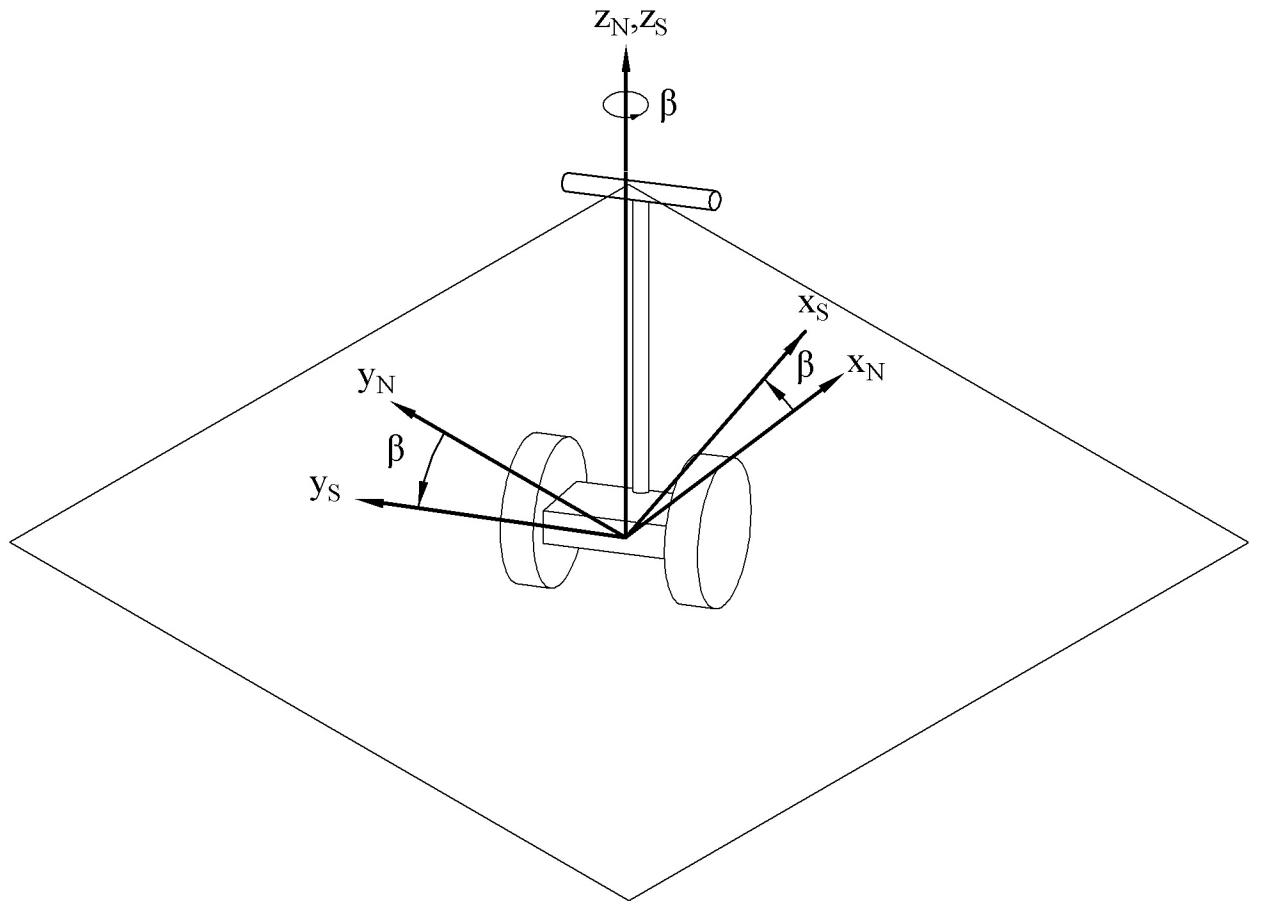
Figure 4.2: Rotating frame 'S' .

4. Point definition: Relevant system points were defined, specifically, wheel contact points with the ground and with the base, the center point of the base, and the point where the impulse force is exerted. The definition includes the body to which these points belong.

5. Body and frame rotation: Here, the rotation of frame 'S' with respect to frame 'N' was defined. Then, the rotation of the wheels and the base with respect to frame 'S' was defined.

6. Relative velocities: Once the angles were defined, the vectors between the points were defined to allow the calculation of relative velocities and accelerations.

7. Constraints definition: The no slip constraint of the wheels was defined.

8. Forces and torques: The gravitational force, the location of forces and torques between bodies, as well as those of the input forces and torques were defined.

9. Generate differential equations.

10. Define inputs and outputs: Numerical values of the parameters may be introduced here or in the resulting MATLAB code. The same applies to input torques and forces. The output definition specified which variables the MATLAB were logged into a data file during the simulation.

11. Produce MATLAB code.

4.1.3   MATLAB Simulation

The MotionGenesis program produces a MATLAB script that simulates the system dynamics. It consists of the following sections:

1. Variable definitions.

2. Assignment of numerical values to the geometric and mass parameters of each component, as well to the initial conditions of all the dynamic variables.

3. Assignment of numerical values to the parameters of the MATLAB numerical solver.

4. Differential equation solving script.

5. Function to evaluate the differential equations and provide the next set of values of the dynamic variables to be input into the next integration step. A space to enter the equations that rule the input torques and forces is provided here.

6. Print variables for each integration step into a log file.

A controller was added to stabilize the simulated pendulum. A paper written by the designers of the Segway describes a relatively simple control law that can be used to stabilize two-wheeled inverted-pendulum human transporters [32]. While the controller on the production version of the Segway is obviously more complex, this simple controller provides a good representation of the overall dynamic properties. The control law implemented in the simulation is given by:

$$\tau_l = K_p \left(\theta_p - \theta_{des}\right) + K_d \dot{\theta}_p - \tau_\beta \tag{4.8}$$

$$\tau_r = K_p \left(\theta_p - \theta_{des}\right) + K_d \dot{\theta}_p + \tau_\beta \tag{4.9}$$

$$\tau_\beta = K_{ff}\dot{\beta}_d + K_{\beta p}\left(\dot{\beta} - \dot{\beta}_d\right) + K_{\beta i}\int_0^t \left(\beta - \beta_d\right)dt \tag{4.10}$$

where K_p, is the proportional gain, and K_d is the derivative gain of the balancing controller. Meanwhile, K_{ff} is the feedforward gain, $K_{\beta d}$ is the proportional gain, and $K_{\beta i}$ is the integral gain of the yaw rate controller. τ_l and τ_r are the torques applied by the motors at each of the wheels, and τ_β is the yaw rate command torque. The desired balancing pitch is given by θ_{des}, which in this case was set to zero, and the measured pitch is θ_p. The desired yaw rate is $\dot{\beta}_d$ and the measured yaw rate is $\dot{\beta}$. The power output limit of the motors was set to 1500 W [12]. The yaw rate is measured by using the rotation speeds of both wheels and using the following equation:

$$\dot{\beta} = \frac{r\left(\dot{\theta}_r - \dot{\theta}_l\right)}{l} \tag{4.11}$$

4.1.4 Unloaded i2 Segway parameter adjustment

A manual pulse pitch response of an unloaded Segway is shown in Figure 4.3. The peak value in this graph was selected as an important parameter to match in the simulations. Even though the response is not exactly under damped, the parameters of an under damped response will be used here to characterize it. The frequency

was obtained by using the times at which the first positive and first negative peaks occur in the angular acceleration response. The damping ratio was obtained from the maximum and minimum pitch angles by using the following equation:

$$\ln\left(\frac{\theta_{max} - \theta_{ss}}{\theta_{ss} - \theta_{min}}\right) = \frac{\pi\zeta}{\sqrt{1 - \zeta^2}} \tag{4.12}$$

where θ_{max} is the maximum pitch, θ_{min} is the minimum pitch, θ_{ss} is the steady-state pitch, and ζ is the damping ratio.

The base speed is shown in Figure 4.4. Two characteristics should be noted from this plot: the value of the first local maximum speed and the steady-state acceleration. These two values were also selected as important parameters for the simulation to match. In summary, the simulation goals are:

1. Peak pitch value $= 8.19°$

2. Period $= 0.316$ s

3. Damping ratio $= 0.295$

4. Peak speed $= 2.474$ m/s

5. Steady-state acceleration $= 0.45$ m/s^2

4.1.4.1   Simulation results

Initially, the parameters were set to the values presented in tables 4.1 and 4.1.1. The parameters were adjusted using the System Identification Toolbox of MATLAB. Since the force was unknown, the speed and pitch data were cropped at the time of the maximum pitch. At this time, no external force is applied on the Segway. Therefore,
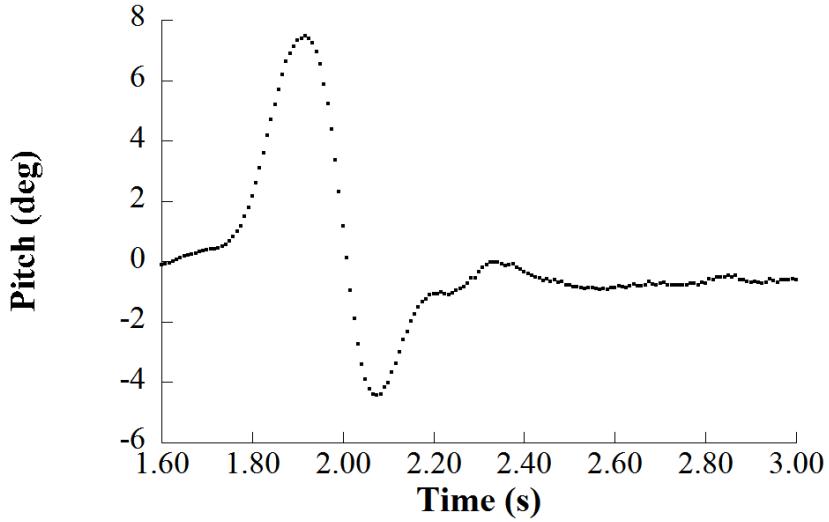
Figure 4.3: Experimental pitch response

numerical values of the system states at that time describe the system completely. The experimental pitch and speed responses were given to the identification routine as desired outputs. The identification toolbox tries different sets of parameters to optimize the error between the outputs obtained from the experiments and the ones obtained from the model.

First, the controller gains were manually set to values that would yield a stable behavior, which were K_p=1000 and K_d=30. Then, the parameters of the unloaded modeled were estimated as it was described in the previous section. Those parameters were introduced into the identification routine. Then, the routine was run several times until a satisfactory response was found. In each of these runs, different parameters were fixed to their initial values. The best result was obtained when the inertias of the wheels and the location of the center of mass of the unloaded Segway were allowed to change.
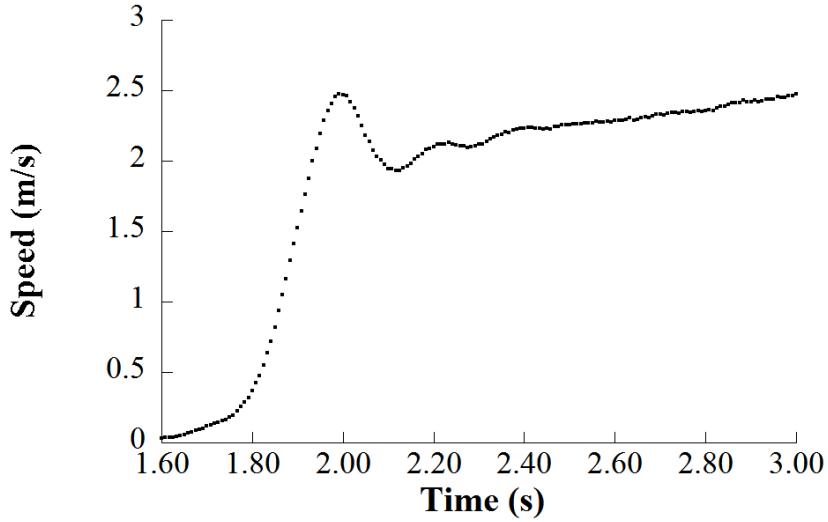
Figure 4.4: Experimental speed.

Table 4.1.4.1 shows the difference between the initial parameters estimations and the values used to match the experiments. The parameters not shown in Table 4.1.4.1 remained unchanged.

Table 4.4: Original and adjusted parameters of the unloaded Segway i2.

Parameter	Initial estimates	Adjusted	Difference %
I_{wy}	0.131 kg·m²	0.0682 kg·m²	48.1
x_p	0.0067 m	0.038092 m	468
z_p	0.0171 m	0.10551 m	517
K_p	1000	373	-
K_d	30	7.82	-

The comparison between the adjusted model pitch response and the experimental response from the chosen initial conditions is shown in Figure 4.5. As shown, the response matches pretty well before 0.2 s. After that, the experiment response shows more damping. This might occur because of the pitch limiting system of the vehicle. The speed responses of both the model and the simulation are shown in Figure

4.1.4.1. Table 4.1.4.1 shows the performance of the simulation in matching the desired response parameters.
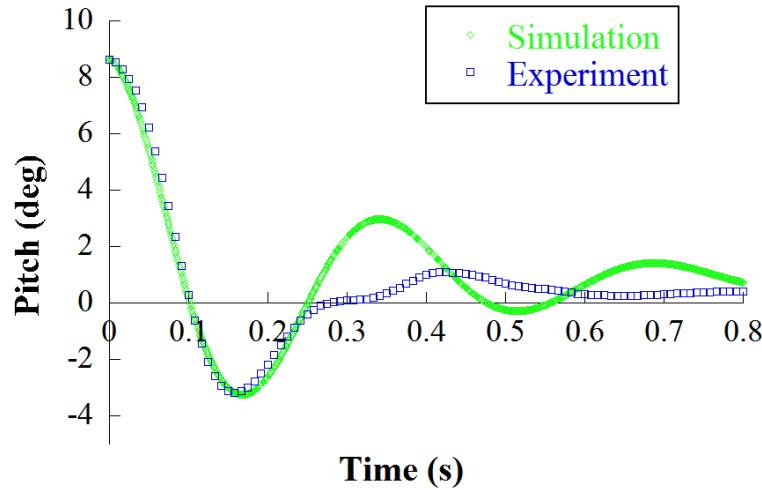
Figure 4.5: Experiment and Simulation pitch response
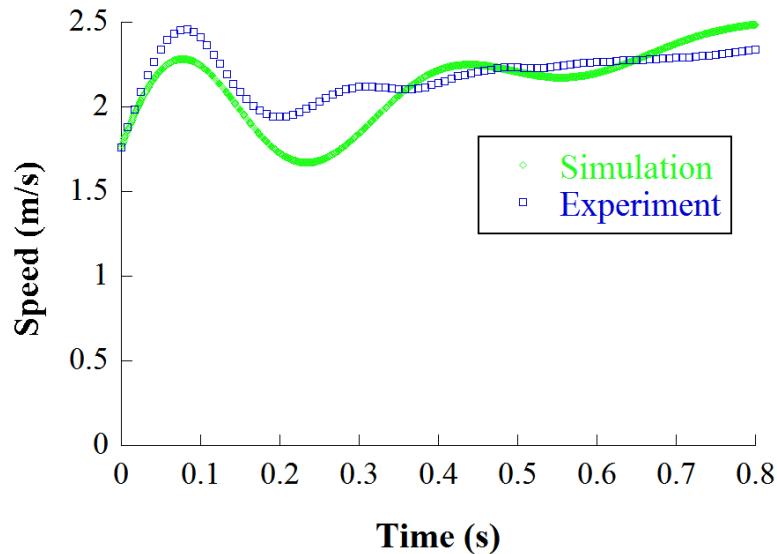
Figure 4.6: Experiment and Simulation speed

4.1.5 Loaded i2 Segway

Figure 4.7 shows a pitch angle response of a loaded Segway i2 after a manual pulse was applied to it. As in the previous case, the data was cropped at the maximum

Table 4.5: Simulation performance

Response characteristic	Desired	Actual	Error %
Peak pitch value	8.19°	8.19°	0
Period	0.316 s	0.342 s	8.2
# of oscillations	0.295	0.299	1.36
Peak speed	2.474 m/s	2.284 m/s	7.67
Steady state acceleration	0.45 m/s^2	0.925 m/s^2	105.5

pitch angle point. Figure 4.8 shows the speed response of the same manual pulse test. The pitch, its derivative, and the base speed values at that time were recorded as the initial conditions to be used in the parameter identification simulations.
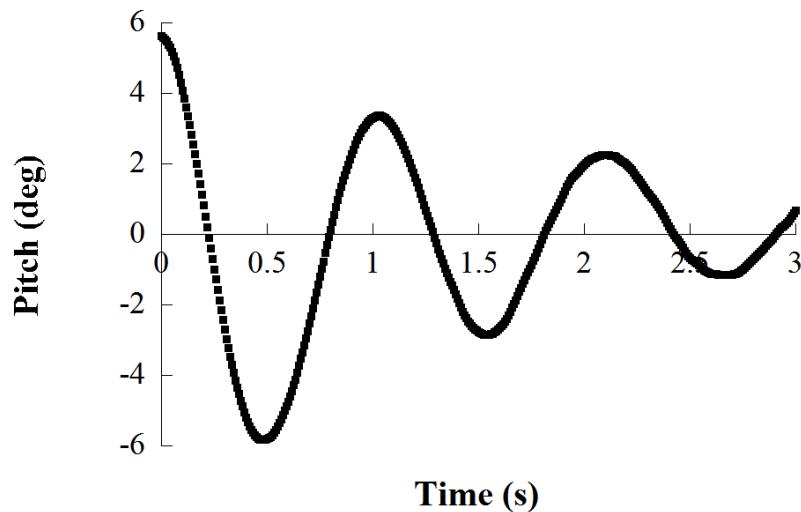
Figure 4.7: Pitch angle response of the loaded Segway i2.

In this case, the desired simulations parameters are:

- Damping ratio = 0.079

- Period = 1.03 s

- Maximum speed = 2.1 m/s

- Steady-state acceleration = 0 m/s^2

95
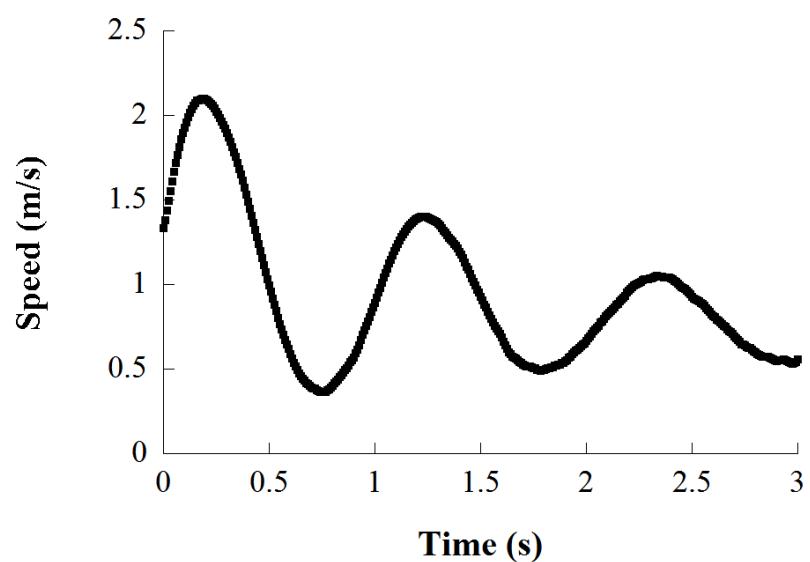
Figure 4.8: Speed response of the loaded Segway i2.

4.1.5.1 Loaded Segway simulation

As in the unloaded Segway case, the estimated parameters were introduced. The inertia of the human body in the y-axis and the relative location of its center of mass were allowed to be adjusted by the identification routine. The mass of the person was left as a fixed value. After several runs, a satisfactory response of the simulation was found. The resulting parameters are shown in Table 4.6.

Table 4.6: Original and adjusted parameters of the loaded Segway i2.

Parameter	Original	Adjusted	Difference %
I_{by}	12.558	16	27.4
x_{wb}	-0.00378	-0.043	1037
z_{wb}	1.072	1.2	11.9

Figure 4.9 shows the pitch response of both the simulation and the experiment. Figure 4.10 shows the speed response. From both figures it is evident that the simulation adjusts very well to the collected data.
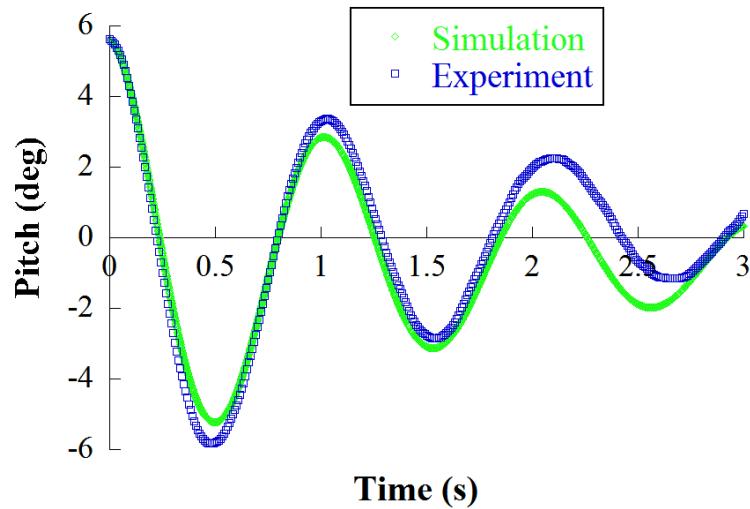
Figure 4.9: Pitch response comparison between simulation and experiment results.

Table 4.7 shows the performance criteria of the loaded simulation with respect to the experiment results.
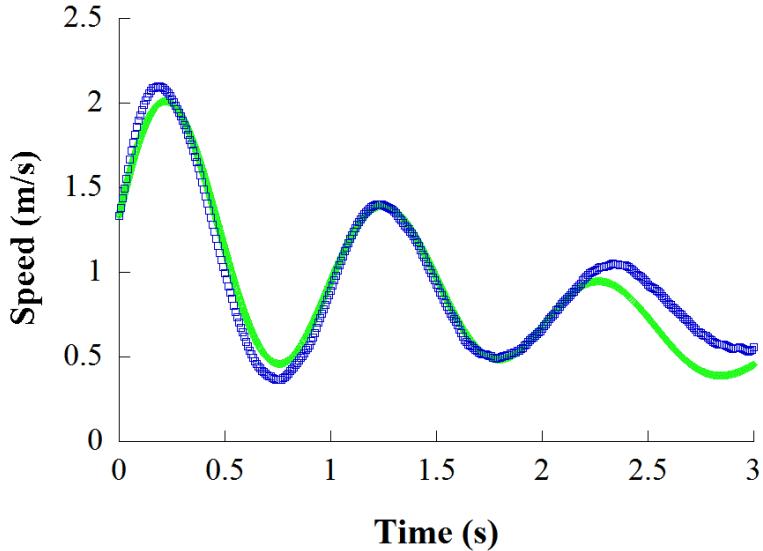
Figure 4.10: Speed response comparison between simulation and experiment results.

Table 4.7: Loaded Simulation Performance.

Response characteristic	Desired	Actual	Error %
Damping ratio	0.079	0.11	39.2
Period	1.03 s	1.02	0.97
Maximum speed	2.1	2.02	3.81

4.1.5.2 Loaded segway verification

The loaded Segway simulation was tested using a loaded pulse test where the force was applied by means of the weight-dropping mechanism. In this case, the force was known, so this same force was applied to the simulation and the results were compared with the experiments. Figure 4.11 shows the pitch response and Figure 4.12 the speed response. Even though the pitch response of the simulation matches reasonably well the response of the experiment, the speed responses do not look so similar. The reason for this is that during the experiments, the user leaned back to stop the Segway.

A new identification routine was carried out using the measured force as the input and the pitch and speed responses as desired outputs. The identification routine attempted to increase the inertia of the human body and the height of its center of

98
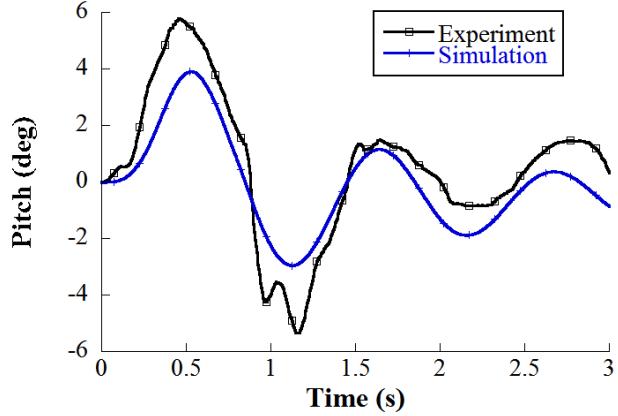
Figure 4.11: Pitch response comparison between simulation and experiment results.
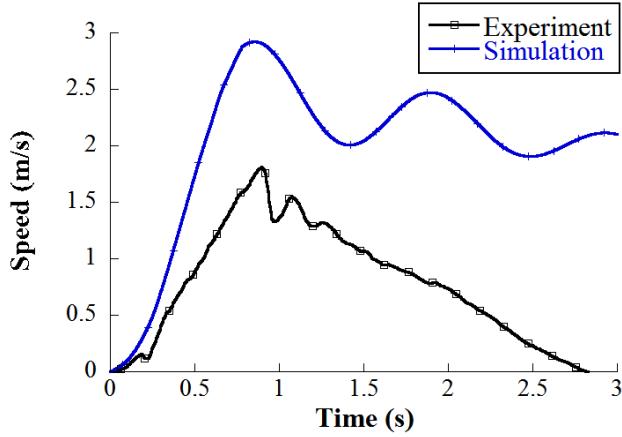
Figure 4.12: Speed response comparison between simulation and experiment results.

mass beyond realistic values, so they were set as fixed numbers. The only parameter set as not fixed was the location of the center of mass of the human body along the x-axis, x_{wb}. As a result, this parameter changed to -0.1011 m, compared to an initial value equal to -0.043 m. This means that, as discussed in Chapter 3, the center of mass of the person moved backwards as he tried to stop the Segway. The pitch and speed responses of the new adjusted simulation are shown in Figure 4.13.

99
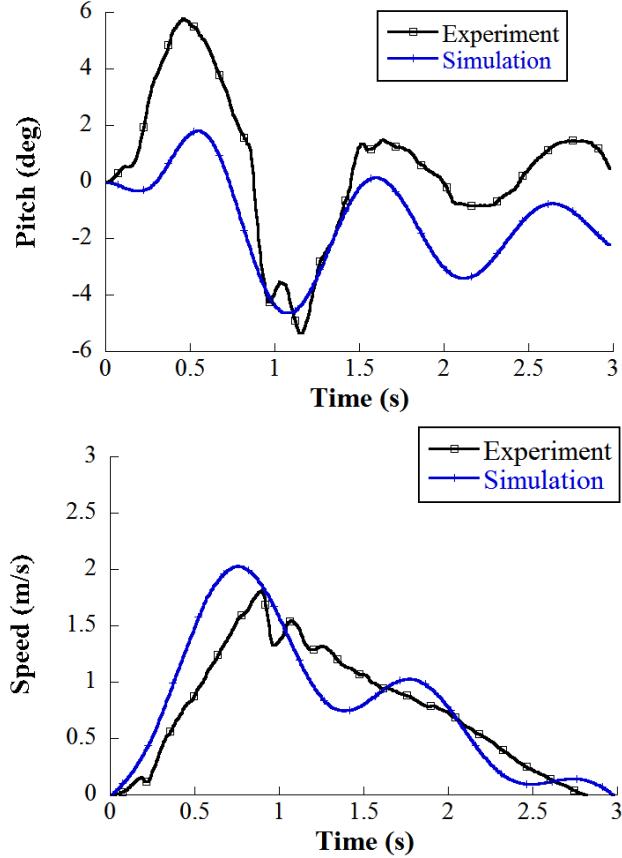
Figure 4.13: Pitch and speed response comparisons between simulation and experiment results.

4.1.6 Yaw rate controller

A set of data from a turning rate experiment was used to tune the yaw controller gains. Figure 4.14 shows the input handlebar roll. The experimental response to this input is shown in Figure 4.15.

An identification routine was set up in MATLAB to adjust the yaw controller gains, while the rest of the Segway and human body parameters were fixed. The yaw controller was described in equation 4.10. The initial estimates of the controller gains were all set to zero. After running the identification routine, the gains obtained were $K_{ff} = 39$, $K_{\beta p} = 243$, and $K_{\beta i} = 280$. Figure 4.16 shows the yaw rate response of the experiment and the simulation.
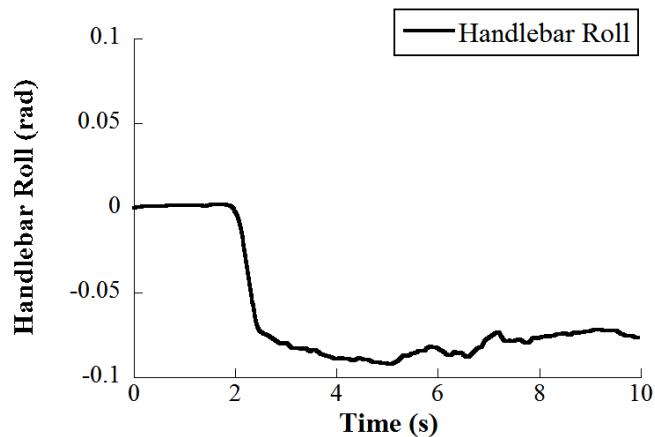
Figure 4.14: Handlebar roll input angle
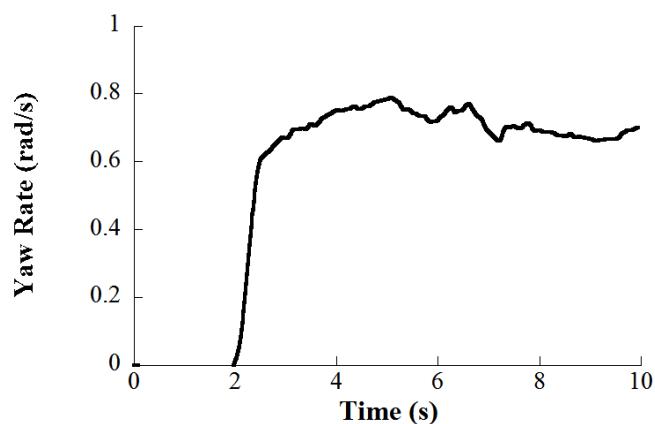
Figure 4.15: Yaw rate measured output.
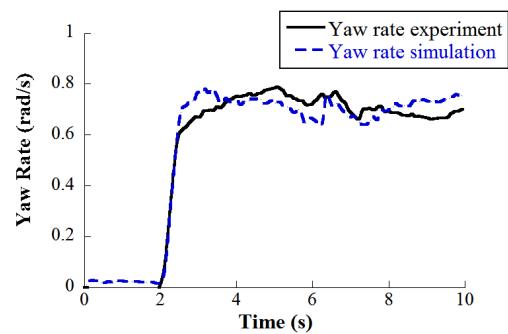
Figure 4.16: Experiment and Simulation yaw rate

4.2   Failure analysis[1]

Given the complex sequence of actions that must continually be performed for the Segway to maintain balance, the Segway has numerous failure modes. Most failures result in the rider falling off the device. However, other outcomes include i) the device running into the rider after the rider has fallen from the device, ii) the device running into a nearby pedestrian, or iii) the device damaging property. The list of failure modes is quite extensive, but a representative list is:

1. The device is not turned on. If the user attempts to mount the device when it is not turned on, then they will fall off because the system has no means to balance. This failure mode was made famous by President Bush in June 2003.

2. The device turns off unexpectedly because of low battery power. When the battery power runs low, the device is supposed to sense this condition and initiate a safety shutdown procedure during which the device makes loud beeping noises, vibrations, and attempts to slow the transporter to a very low velocity. However, sensing the available power in batteries is challenging, so under some conditions, the low-battery condition is not properly sensed and the machine turns off quickly - without going through the safety shutdown procedure.

3. The device turns off unexpectedly because of dangerous conditions. When an operator leans forward, the center of mass is moved in front of the wheel and the device starts to fall forward. In order to regain balance, the bottom of the machine must race forward and get the wheels out in front of the center of mass so that the system starts to tip backwards. If the forward pitching angle is too large, then the machine cannot accelerate the wheels fast enough to regain balance. The control system is programmed to detect this condition,

---

[1] *This section includes excerpts from "An Engineering Overview of the Segway Personal Transporter" by Dr. William Singhose.*

and many other conditions that are outside of the machine's ability to regain balance. Rather than increase the machine's speed in a futile attempt to regain balance, the machine turns off to limit the severity of the failure. A typical example is when the operator leans backward in order to break suddenly, but ends up going backwards, so to correct the situation he leans forward again, action which very often results in a very high forward pitching angle.

4. The device falls over because a wheel hits an immovable object. If a wheel contacts an object that stops the wheel from moving in a desired direction, then the machine cannot balance. Common examples of problematic obstacles include: doorjambs, chairs, and curbs.

5. The device falls over because a wheel loses traction. If a wheel loses traction, then it cannot apply the correct forces in order to balance the system. If the wheel spins excessively, then the machine will turn off - this is a case of dangerous conditions as previously discussed. Common ways to lose traction include: one wheel dropping off a curb or into a hole and passing over slick surfaces such as ice, sand, wet grass, and mud.

6. The device moves without rider in balance mode. If the rider steps off the device and does not hold it while it is in balance mode, the device will start moving forward. If this happens, the device might run into nearby objects causing damage. It can also run into a pedestrian, which can result in injury.

7. The device runs into the rider. This can happen when the rider steps off the device while pulling back the handle bar. This makes the device go backwards and run into the leg of the rider. This can also occur if a surface irregularity causes the rider to jump off to the front of the device.

8. The device becomes unstable when making turns. At certain combinations of speed and turning radii, centrifugal force shifts the weight towards one of the wheels, and less to the other. This can cause the device to roll over very suddenly, carrying with it a consequent loss of traction in one of the wheels. It does not need to travel at very high speeds for this to occur, as long as the turning radius is small enough.

Several failure conditions were simulated and the results are presented in the next sections. These consist of:

- Turning motion at different speeds and turning rates.

- Traveling along inclined surfaces at different pitch angles, speeds and slopes.

- Losing traction in one or both wheels.

- Applying disturbance forces in a wheel and in the base-handlebar set.

4.2.1   Turning

The turning motion occurs when the rider tilts the handlebar towards the left or the right. In the Segway i2, tilting the handlebar occurs simultaneously as the rider tilts his body. This sideways bending by the person is a natural result of the movements required to tilt the handlebar. This helps to maintain balance in the roll direction and counteracts the centrifugal effect of the turning motion on the human body. In the Segway i167, the yaw rate is commanded by a grip on the left handle and the user must actively tilt towards the side he is turning in order to maintain balance. Turning the grip only requires wrist motion, so the roll stability is reduced. The simulations presented in this section work under the following assumptions:

- All the basic assumptions presented in Chapter 2.

- The yaw command is assumed to be a step function.

104

A series of left turns (positive yaw rate) were simulated. Here, a sideways bending motion of the person riding the Segway was not accounted for. For that reason, these simulations are best to describe the turning motion of a Segway i167 or the turning of a Segway i2 at small yaw rates. Turning motion towards the left (positive yaw rate) was simulated for different initial speeds and different initial pitch angles. The yaw rate, pitch, speed, and normal force on the wheels were recorded to study what effect does changing the initial speed and pitch have on them. First, the effect of the vehicle's initial speed is studied.

The effect of the travel speed on the turning motion of the Segway was studied using an initial pitch angle of 0°, or the angle at which the simulation balances. The transporter balances actually around a pitch of 1.2° with respect to the 'S' frame, but in the following sections this case will be labeled as 0°. This angle was chosen because it represents any case in which the vehicle is traveling at constant speed. Figure 4.17 shows the yaw rate response of the Segway when a desired yaw command of 1 rad/s is given to the model at different initial speeds. As noticed, the initial speed of the vehicle doesn't seem to affect the yaw dynamics of the Segway.

Figure 4.18 shows the pitch response. Similarly to the yaw response, the initial speed doesn't affect the tilting dynamics of the Segway in the forward/backward direction. Furthermore, since the Segway was initially balanced, the pitch angle remained very close to its balanced position. This is consistent with the dynamic equations of the vehicle, and assumes absolutely no external disturbances during the turning motion. Therefore, it is expected that in a real turning test, the pitch angle would not remain as stable as in these simulations.

Figure 4.19 shows the normal force between the left wheel and the ground. Initially, the normal force seems to be only affected by the posture of the vehicle, and was the same for all initial speeds. However, as the vehicle turned left, the normal
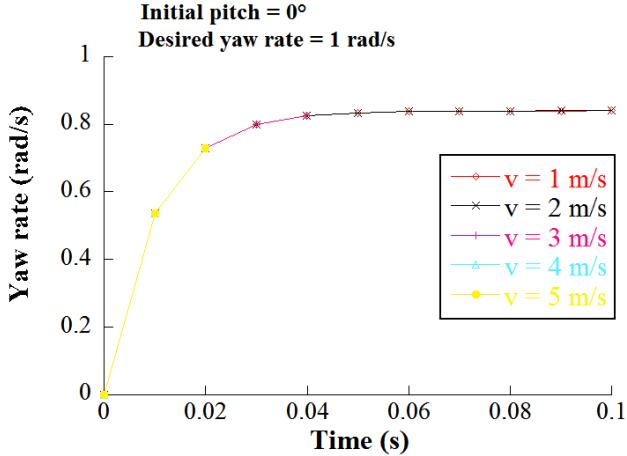
Figure 4.17: Yaw rate response at different initial speeds - turning simulations.
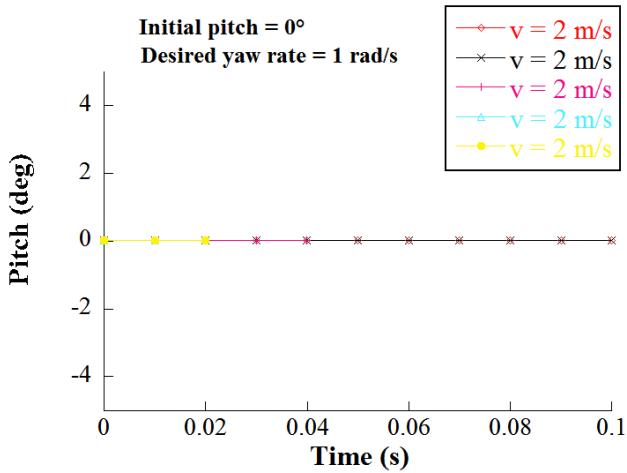
Figure 4.18: Pitch response at different initial speeds - turning simulations.

force decreased. When the initial speed was 3 m/s or higher, the force actually decreased to zero. Hence, at speeds above 3 m/s, the right wheel lost contact with the ground and the simulation was terminated. It is important to note that as a consequence of this, the right wheel loses traction and the no-slip constrain ceases to be valid. Because the yaw rate is measured by using the rotation speeds of both wheels, losing contact with the ground can render the yaw rate dynamics unstable, making the situation worse. From Figure 4.19 it can also be noted that the loss of contact with the ground occurs in less that 0.04 s, which is a very small frame of time for the user to react. This normal force is given by:

106

$$F_{nlz} = 0.5g(m_b + m_p + 2m_w) - 0.5(I_{by}\dot{\beta}\dot{\theta}_p + I_{py}\dot{\beta}\dot{\theta}_p + I_{wy}\dot{\beta}\dot{\theta}_l + I_{wy}\dot{\beta}\dot{\theta}_r + ra(2m_w v\dot{\beta} +$$

$$m_b(v\dot{\beta} + z_{wb}(2\cos(\theta_p)\dot{\beta}\dot{\theta}_p + \sin(\theta_p)\ddot{\beta}) - x_{wb}(2\sin(\theta_p)\dot{\beta}\dot{\theta}_p - \cos(\theta_p)\ddot{\beta})) - m_p(2x_{wp}\sin(\theta_p)\dot{\beta}\dot{\theta}_p$$

$$- v\dot{\beta} - x_{wp}\cos(\theta_p)\ddot{\beta} - z_{wp}(2\cos(\theta_p)\dot{\beta}\dot{\theta}_p + \sin(\theta_p)\ddot{\beta}))) - \sin(\theta_p)(I_{bx}\sin(\theta_p)\dot{\beta}\dot{\theta}_p - z_{wb}m_b w\ddot{\theta}_p -$$

$$I_{bz}(\sin(\theta_p)\dot{\beta}\dot{\theta}_p - \cos(\theta_p)\ddot{\beta})) - \cos(\theta_p)(I_{pz}\cos(\theta_p)\dot{\beta}\dot{\theta}_p - x_{wb}m_b w\ddot{\theta}_p - m_p w(z_{wp}\dot{\theta}_p^2 + x_{wp}\ddot{\theta}_p) -$$

$$I_{px}(\cos(\theta_p)\dot{\beta}\dot{\theta}_p + \sin(\theta_p)\ddot{\beta}) - m_p z_{wp}(v\dot{\beta} + x_{wp}\cos(\theta_p)\ddot{\beta} + z_{wp}(2\cos(\theta_p)\dot{\beta}\dot{\theta}_p + \sin(\theta_p)\ddot{\beta}))) -$$

$$\cos(\theta_p)(I_{bz}\cos(\theta_p)\dot{\beta}\dot{\theta}_p - z_{wb}m_b w\dot{\theta}_p^2 - I_{bx}(\cos(\theta_p)\dot{\beta}\dot{\theta}_p + \sin(\theta_p)\ddot{\beta}) - z_{wb}m_b(v\dot{\beta} + z_{wb}(2\cos(\theta_p)$$

$$\dot{\beta}\dot{\theta}_p + \sin(\theta_p)\ddot{\beta}) - x_{wb}(4\sin(\theta_p)\dot{\beta}\dot{\theta}_p - \cos(\theta_p)\ddot{\beta}))) - \sin(\theta_p)(x_{wb}m_b w\dot{\theta}_p^2 + I_{px}\sin(\theta_p)\dot{\beta}\dot{\theta}_p +$$

$$m_p w(x_{wp}\dot{\theta}_p^2 - z_{wp}\ddot{\theta}_p) + x_{wb}m_b(v\dot{\beta} + z_{wb}\sin(\theta_p)\ddot{\beta} - x_{wb}(2\sin(\theta_p)\dot{\beta}\dot{\theta}_p - \cos(\theta_p)\ddot{\beta})) - I_{pz}(\sin(\theta_p)$$

$$\dot{\beta}\dot{\theta}_p - \cos(\theta_p)\ddot{\beta}) - m_p x_{wp}(2x_{wp}\sin(\theta_p)\dot{\beta}\dot{\theta}_p - v\dot{\beta} - x_{wp}\cos(\theta_p)\ddot{\beta} - z_{wp}(4\cos(\theta_p)\dot{\beta}\dot{\theta}_p +$$

$$\sin(\theta_p)\ddot{\beta}))))/w$$
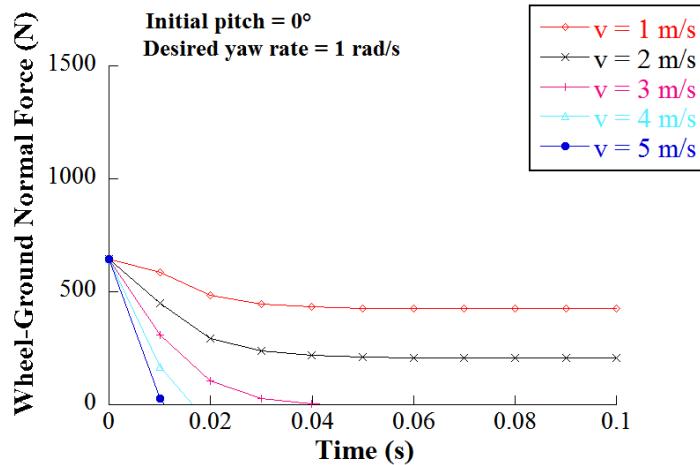
Figure 4.19: Left wheel-ground normal force at different initial speeds - turning simulations.

Figure 4.20 shows the speed of the vehicle. Given that the pitch angle remains stable during the turning motion, the speed also does, and remains constant at its initial value. This, as in the pitch response, is an idealization from a real scenario where there are always unknown disturbance forces. It is important to note that the limit speed of the Segway of 12.5 mph (marked with green lines on Figure 4.20) was not exceeded.
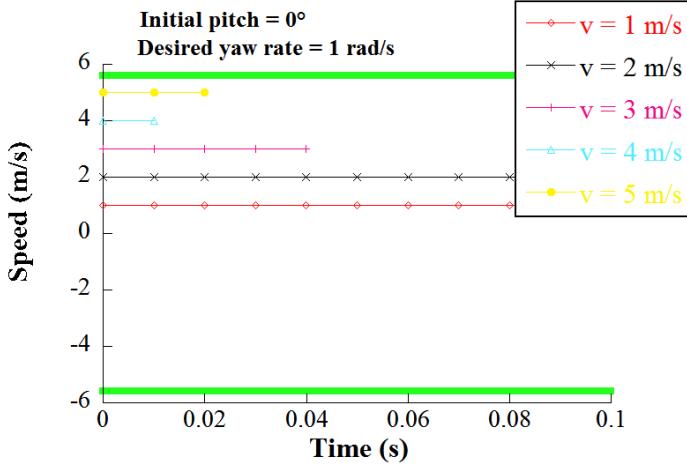
Figure 4.20: Speed response at different initial speeds - turning simulations.

Next, the initial speed was fixed to 1 m/s, a desired yaw rate of 0.5 rad/s was used. Next,the initial pitch angle was varied between -20° and 20°. Figure 4.21 shows the normal force between the left wheel and the ground. In the 10° and 20° initial pitch cases, the force became negative almost instantly. It is not likely that this would be the case in a real system where the wheels are deformable. If the elasticity of the wheels was taken into account, the response would approximate more closely to a real scenario. However, these simulations are helpful to get an idea of how difficult it is to yield the Segway unstable when making turns. In the cases where the initial pitch angle was negative, the force initially increased and then dropped and oscillated around the upright balancing value. As the pitch angle increased in the negative direction, the force reached lower minimum values.

Figure 4.22 shows the yaw rate response of the vehicle. The simulations were cropped at the moment when the normal force of the wheel reached zero. The pitch angle affects the speed and stability of the yaw rate controller. A larger negative angle caused more overshoot and a slower response.

Figure 4.23 shows the pitch angle response. As expected, a larger initial pitch angle caused oscillations with higher amplitudes and with a slightly changing period.

108
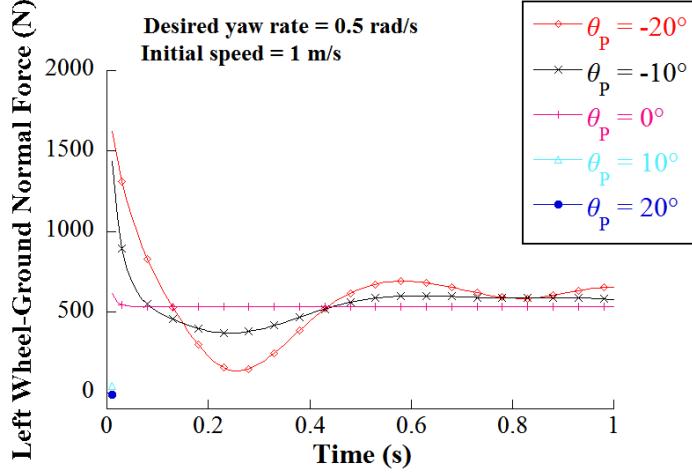
Figure 4.21: Left wheel-ground normal force at different initial pitch angles - turning simulations.
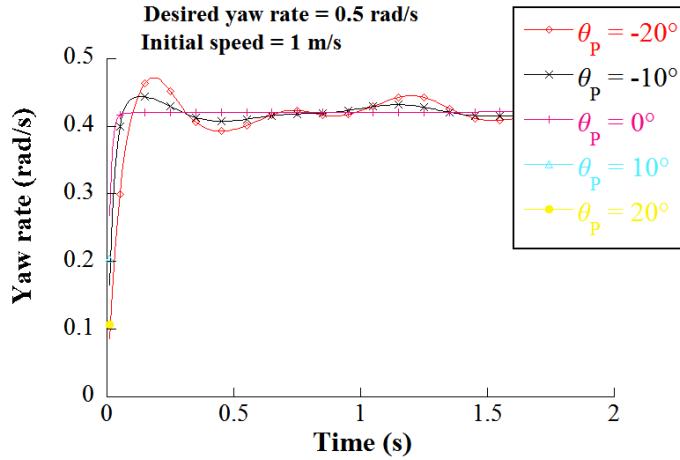
Figure 4.22: Yaw rate response at different initial pitch angles - turning simulations.

However, in none of the cases the pitch went outside of the limit range from -40° to 40°, shown as the green lines in Figure 4.23.

Figure 4.24 shows the speed response of the vehicle. Even though the initial speed was the same for all cases, the speed was affected by the initial pitch angle. Larger pitch angles, whether positive or negative, caused more speed oscillation. In spite of this, the speed limits of the Segway were never exceeded.
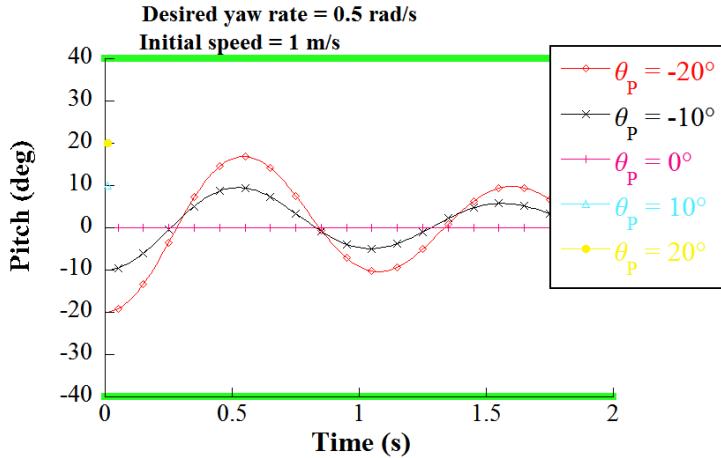
Figure 4.23: Pitch response at different initial pitch angles - turning simulations.
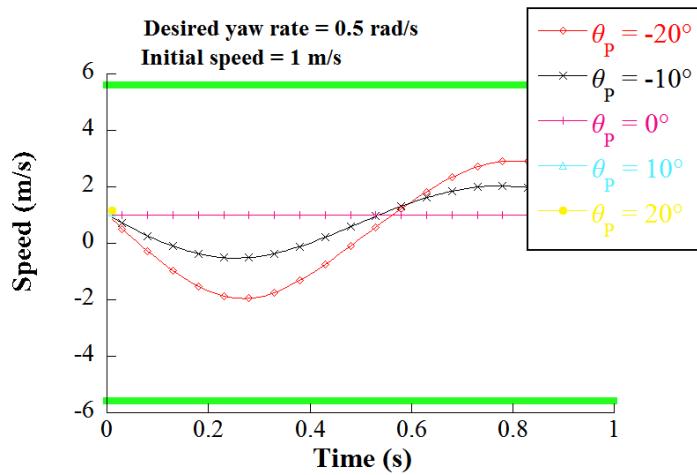
Figure 4.24: Speed response at different initial pitch angles - turning simulations.

Even though only relatively low yaw rates and low speeds were simulated, the Segway can lose roll stability in some of these conditions. At higher speeds and yaw rates, it will be more likely to lose stability in the roll direction.

4.2.2 Inclined surface

When a Segway travels along an inclined surface, like any other vehicle, the torque requirements to achieve balance will inevitably change. The Segway needs additional torque to advance uphill or to remain at rest. In this section, the effect of traveling along inclined surfaces with different slope angles is studied. Several simulations were carried on with a range of different initial pitches and initial speeds.

A new dynamic model was developed to include the possibility of traveling along an inclined surface. Here, the simulation was restricted to travel only up or down the hill, without any possibility to perform turning motion, in order to simplify the analysis. Figure 4.25 shows the system of coordinates defined to represent the system. The Newtonian reference frame is 'N'. The frame 'Slope' is rotated an angle θ_{Slope} with respect to the frame 'N' and its 'x' axis is parallel to the inclined surface. The coordinate system 'S' was defined in previous models as an auxiliary frame that rotates with respect to frame 'N' around the z_N axis. In this case, the frames 'S' and 'Slope' are parallel. The reference frame 'P' rotates along with the human-pendulum system an angle of θ_P with respect to frame 'Slope'. The rotation angle of the pendulum with respect to frame 'N' is given by:

$$\theta_{P/N} = \theta_P + \theta_{Slope} \tag{4.13}$$
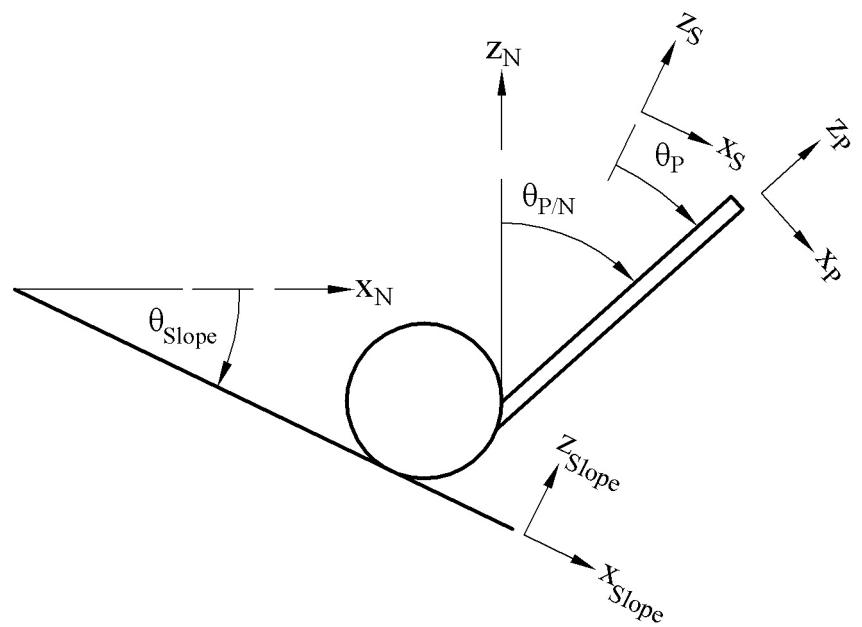
Figure 4.25: Segway model traveling over an inclined surface.

The dynamic equations that take into effect the inclination of the ground surface are:

$$\ddot{\theta}_p = ((gm_b(x_{wb}cos(\theta_{slope} + \theta_p) + z_{wb}sin(\theta_{slope} + \theta_p)) - 2T_y + gm_p(x_{wp}cos(\theta_{slope} + \theta_p) + z_{wp}sin(\theta_{slope} + \theta_p)))(m_b + m_p + 2m_w + (2iy)/r^2) - (m_b(z_{wb}cos(\theta_p) - x_{wb}sin(\theta_p)) + m_p(z_{wp}cos(\theta_p) - x_{wp}sin(\theta_p)))((2T_y)/r + \dot{\theta}_p^2(m_b(x_{wb}cos(\theta_p) + z_{wb}sin(\theta_p)) + m_p(x_{wp}cos(\theta_p) + z_{wp}sin(\theta_p))) + gm_bsin(\theta_{slope}) + gm_psin(\theta_{slope}) + 2gm_wsin(\theta_{slope})))/((m_b + m_p + 2m_w + (2iy)/r^2)(iby + ipy + m_b(x_{wb}^2 + z_{wb}^2) + m_p(x_{wp}^2 + z_{wp}^2)) - (m_b(z_{wb}cos(\theta_p) - x_{wb}sin(\theta_p)) + m_p(z_{wp}cos(\theta_p) - x_{wp}sin(\theta_p)))^2)$$

$$\dot{v} = ((I_{by} + I_{py} + m_b(x_{wb}^2 + z_{wb}^2) + m_p(x_{wp}^2 + z_{wp}^2))((2T_y)/r + \dot{\theta}_p^2(m_b(x_{wb}cos(\theta_p) + z_{wb}sin(\theta_p)) + m_p(x_{wp}cos(\theta_p) + z_{wp}sin(\theta_p))) + gm_bsin(\theta_{slope}) + gm_psin(\theta_{slope}) + 2gm_w sin(\theta_{slope})) - (m_b(z_{wb}cos(\theta_p) - x_{wb}sin(\theta_p)) + m_p(z_{wp}cos(\theta_p) - x_{wp}sin(\theta_p)))(gm_b(x_{wb}cos(\theta_{slope} + \theta_p) + z_{wb}sin(\theta_{slope} + \theta_p)) - 2T_y + gm_p(x_{wp}cos(\theta_{slope} + \theta_p) + z_{wp}sin(\theta_{slope} + \theta_p))))/((m_b + m_p + 2m_w + (2I_y)/r^2)(I_{by} + I_{py} + m_b(x_{wb}^2 + z_{wb}^2) + m_p(x_{wp}^2 + z_{wp}^2)) - (m_b(z_{wb}cos(\theta_p) - x_{wb}sin(\theta_p)) + m_p(z_{wp}cos(\theta_p) - x_{wp}sin(\theta_p)))^2)$$

Since the pitch angle of the Segway was defined with respect to the frame 'Slope', the control law was modified, since the pitch angle to be controlled is the absolute pitch $\theta_{P/N}$. The new control law is given by:

$$\tau_y = K_p\theta_{P/N} + K_d\dot{\theta}_{P/N} \tag{4.14}$$

Assuming that the person stands in an upright posture on the Segway, with respect to axis z_P, the normal force between him and the transporter was found to be:

$$F_{fz} = 0.5m_b[gcos(\theta_{Slope} + \theta_p) + sin(\theta_p)\dot{v} - z_{wb}\dot{\theta}_p^2 - x_{wb}\ddot{\theta}_p] \tag{4.15}$$

In summary, these simulations work under the following assumptions:

- All the basic assumptions presented in Chapter 2.

113

- A rigid body model of the human rider is used.

- The ground is an inclined plane of constant slope.

- The pitch angle is measured with respect to the upright posture of the vehicle.

- The simulation vehicle follows a straight trajectory along the line of greatest slope.

Figure 4.26 shows the pitch response for different slope angles. A positive slope means that the Segway is going downhill while a negative one means that the Segway is going uphill. The initial speed for all tests was 1 m/s and the initial pitch with respect to frame 'N' was 0°. On a flat surface, the simulated transporter remained balanced, since there are no disturbances at all. When the slope angle becomes positive the pitch response shifts below the initial pitch angle. This means that when going downhill, the Segway needs to tilt backward in order to achieve balance. When the slope is negative the pitch angle increases, which indicates that when the transporter climbs a slope it needs to tilt forward to increase the torque applied on the wheels.
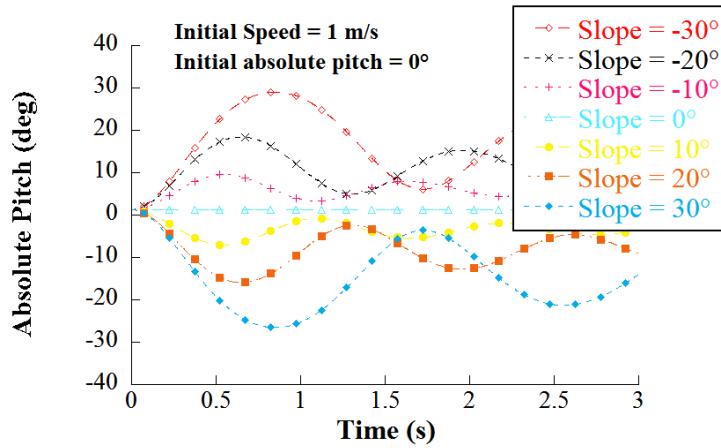
Figure 4.26: Pitch response at different slopes - slope simulations.

Figure 4.27 shows the speed response of the Segway. When the slope is positive, or the transporter is traveling downhill, the speed increases. As can be noticed in

114

Figure 4.27, in the case of a slope angle of -30°, the speed almost reached the speed limit. In the same figure, it can be seen that when the slope was positive (uphill trajectory), the speed decreased over time. Here it is assumed that the person is standing passively on the Segway, so it is easy to imagine that the person might need to tilt forward at a higher angle to keep the Segway going uphill in a real scenario. The Segway might not be able to climb pronounced positive (downhill) slopes, since as it was seen in Figure 4.26, without the operator doing any motion, the Segway already reached pitch angles of 30°. If the operator tried to lean further, the load on the motors might be to large to balance the transporter effectively.
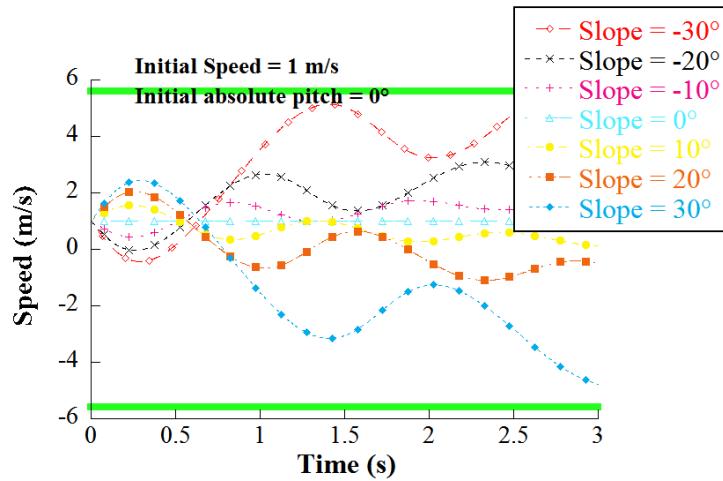
Figure 4.27: Speed response at different slopes - slope simulations.

Figure 4.28 shows the force between the person and the Segway as it travels along the inclined surface. Even though the amplitude and frequency of the force were affected by the slope angle, the force never went dangerously closely to zero.

The effect of the initial speed was also studied. Figure 4.29 shows the pitch response after setting the initial speed at different values. The initial pitch angle was set to 0° and the slope angle was 30°. As seen in Figure 4.29, the pitch is not affected by the initial speed of the vehicle.
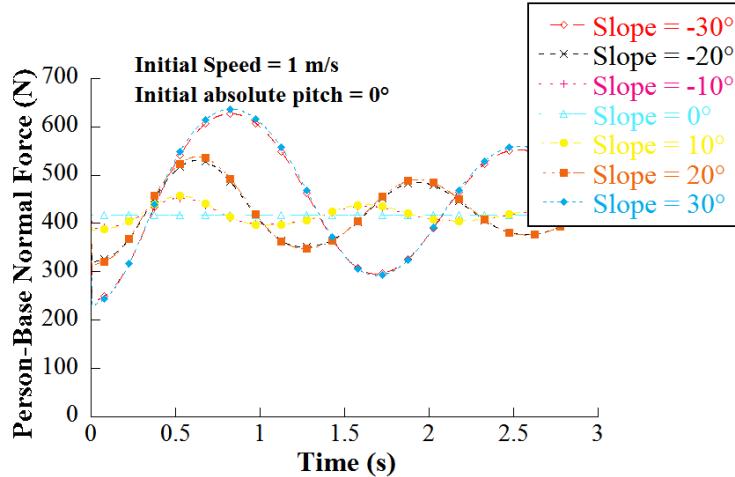
Figure 4.28: Base-person normal force at different slopes - slope simulations.
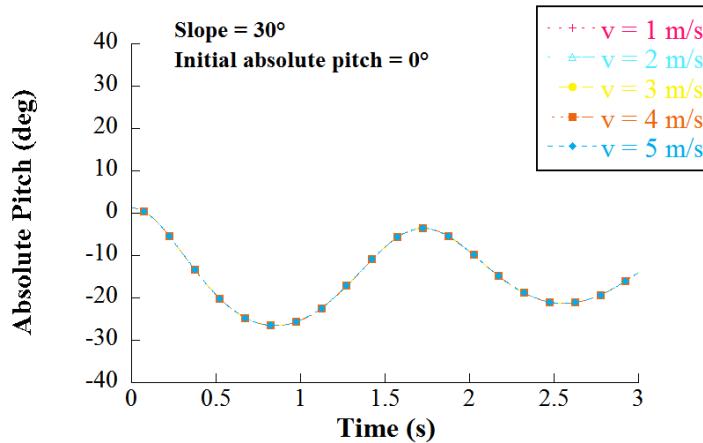
Figure 4.29: Pitch response at different initial speeds - slope simulations.

Figure 4.30 shows that the speed response has the same dynamic characteristics for all cases, except that they are shifted vertically according to the initial value. The 5 m/s case shows that even if the Segway starts going downhill at a speed within its limits, this speed can be easily increased beyond that value within less than 0.5 s. Going beyond the speed limit of the Segway for a very long period of time can be dangerous.

Figure 4.31 shows the normal force at different speeds. In all cases the force stayed well above 0.
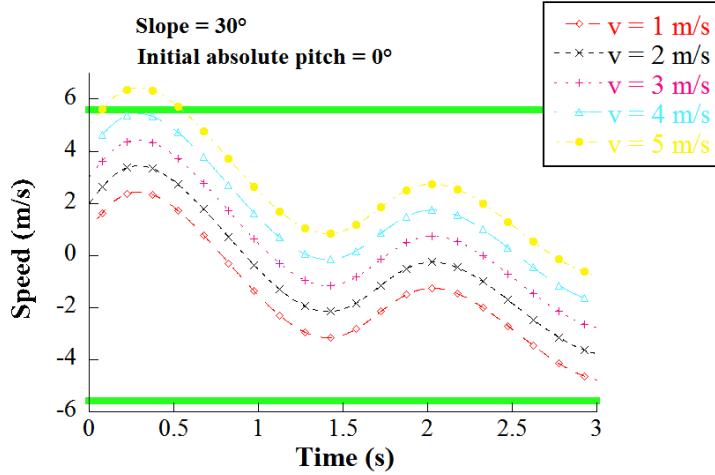
Figure 4.30: Speed response at different initial speeds - slope simulations.
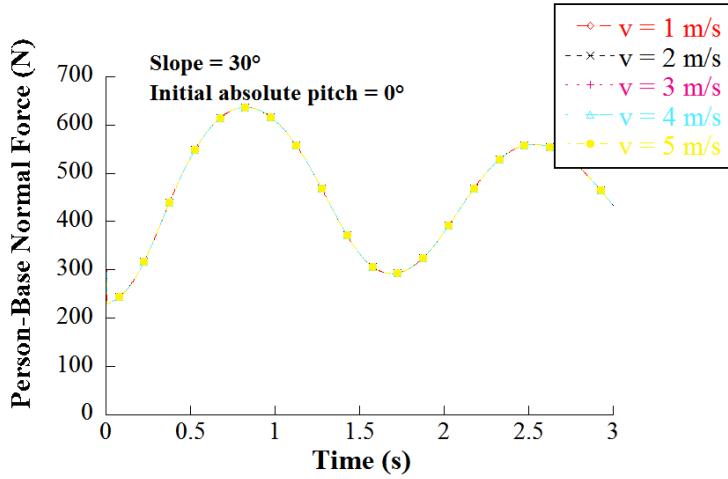
Figure 4.31: Base-person normal force at different initial speeds - slope simulations.

The effect of changing the initial pitch angle was studied for both the uphill and downhill case. For the downhill case, the initial speed was set to 2.5 m/s and the slope angle to 20°. Figure 4.32 shows the pitch response for different cases. The amplitude of the pitch response increased as the initial pitch angle is increased. This means that if the transporter enters a downhill while accelerating the risk of going beyond bounds of the admissible pitch is greater. It also shows, as in the 20° case, that the pitch angle can change drastically in a very short period of time.
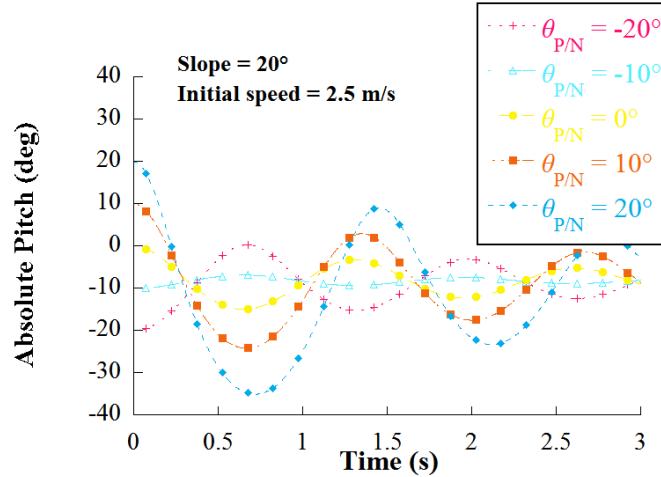
Figure 4.32: Pitch response at different initial pitch angles - downhill slope simulations.

Figure 4.33 shows the speed as the simulated Segway went downhill. The higher the initial pitch angle was, the greater was the reached speed. In the case where the initial pitch was 20°, the speed went above the speed limit of the transporter within less than 0.5 s into the simulation. This is consistent with the previous observation in that it is risky to go downhill while accelerating (tilting forward).
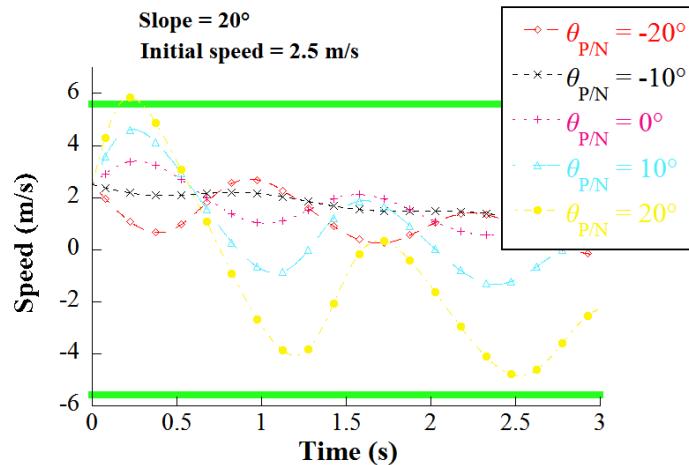
Figure 4.33: Speed response at different initial pitch angles - downhill slope simulations.

Figure 4.34 shows the forces between the rider and the Segway, assuming that the rider has no movement relative to it. In the case of the 20° initial pitch, the force

decreased considerably. This is a result of the initial increase of the speed as shown in Figure 4.33 and initial reduction of the pitch as shown in Figure 4.32. In other words, the Segway initially accelerated while it rotating backwards. This combination of movements caused the force between the rider and the Segway to decrease.
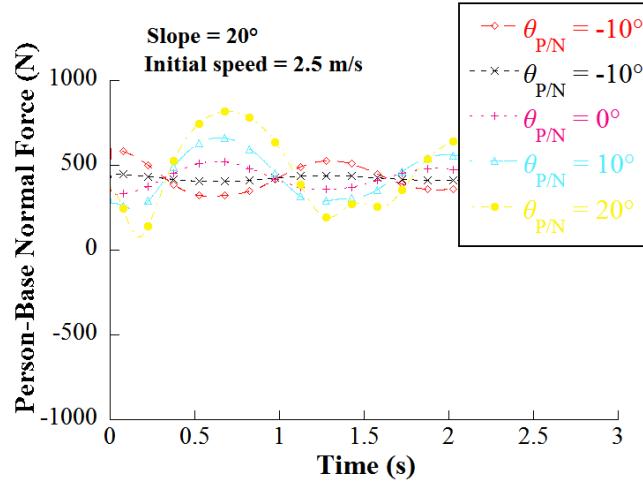
Figure 4.34: Base-person normal force response at different initial pitch angles - downhill slope simulations.

The effect of changing the initial pitch angle was also studied for a transporter going uphill. Figure 4.35 shows the pitch response. As seen, as the initial pitch angle was reduced, the pitch response reached a greater maximum value. In one case it even got close to the pitch limit. This was a result of the Segway slowing down as it went uphill due to the force of gravity. The decrease in speed caused it to tilt forward.

Figure 4.36 shows the speed response. It is seen that when the transporter was initially tilted forward, the speed oscillated slightly as it traveled uphill. However, when it was initially tilted backwards, the speed decreased. This caused the transporter to tilt forward. As a reaction, the motors increased the speed in order to try to keep it balanced.

Figure 4.37 shows the force between the person and the Segway. In the cases where the initial pitch was negative, the force decreased very closely to zero in a very short period of time. When the Segway started going uphill it slowed down and the
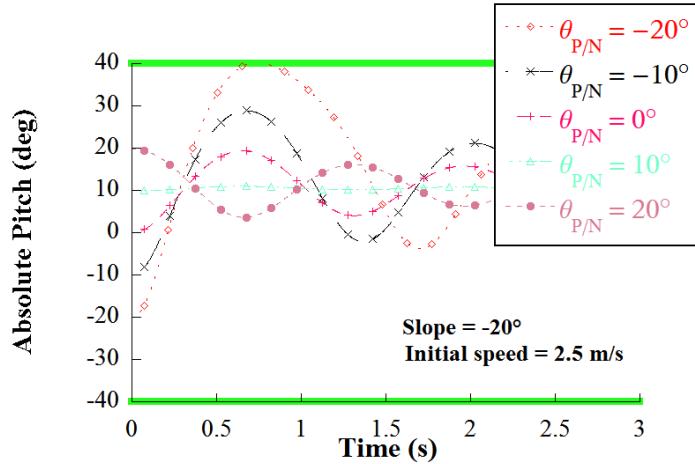
Figure 4.35: Pitch response at different initial pitch angles - uphill slope simulations.
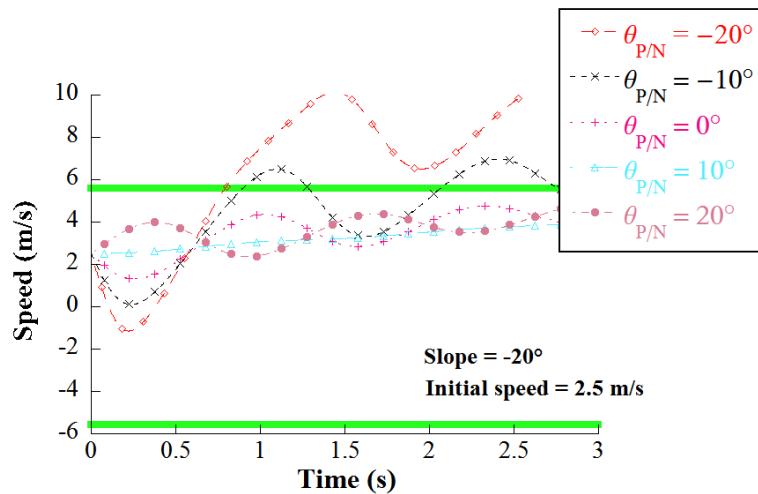
Figure 4.36: Speed response at different initial pitch angles - uphill slope simulations.

pitch angle increased. As this happened, the inertia of the person resisted this motion and tried to keep going forward. As a consequence, the contact force between the body and the vehicle was reduced.
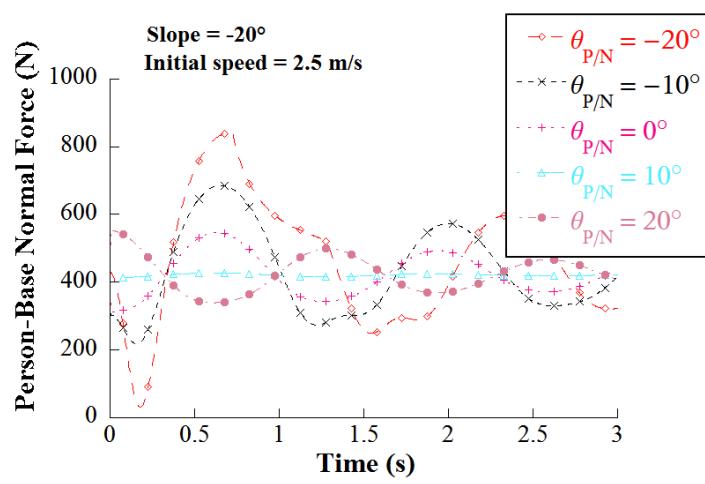
Figure 4.37: Base-person normal force response at different initial pitch angles - uphill slope simulations.

4.2.3 Slipping

When designing a controller for an inverted pendulum system it is assumed that there is no slip between the wheel and the ground. This produces the kinematic constraint that is given by:

$$v = r\dot{\theta} \qquad (4.16)$$

where v is the speed of the center point of the wheel, r is its radius and $\dot{\theta}$ is its angular speed. However, when there is slip, this constraint no longer applies and the performance of the controller can degrade.

Two-wheeled inverted pendulums can travel along two dimensional paths by modifying the angular speeds of both wheels. So if it wants to move towards the right, then the left wheel is spun at a higher rate than the right wheel. In order to adjust the turning rate, the controller measures the current turning rate and compares it with the desired turning rate to produce torques on the wheels according to this error, as explained by equation 4.10.

In a Segway Human Transporter the controller approximates the turning rate by using the following equation [20, 19]:

$$\dot{\beta} = \frac{r\left(\dot{\theta}_r - \dot{\theta}_l\right)}{l} \qquad (4.17)$$

where $\dot{\beta}$ is the turning rate, l the distance between the center points of the two wheels, and $\dot{\theta}_l$ and $\dot{\theta}_r$ are the angular speeds of the left and right wheel [32]. However, this turning rate is only accurate when there is no slip between the wheels and the ground. Therefore, if one wheel gets stuck in a slick surface and starts spinning faster without moving, the controller might sense that the turning ratio is too high and try to accelerate the other wheel to compensate for this. This would produce a turning

motion towards the wheel that is slipping. If the right wheel slips, and the left wheel maintains its current speed, the vehicle ends up turning towards the right.

The modeling of the friction force between a turning wheel and a ground surface is a complex subject in itself. The friction force required to maintain a no slip condition or a specified slip velocity depends on the acceleration and normal forces at a certain time. Here, the effect on the vehicle dynamics when the no slip condition is suddenly lost is studied. First, the wheel slip is defined as:

$$s = \frac{\dot{\theta}_w r - v}{v} \tag{4.18}$$

where $\dot{\theta}_w$ is the angular speed of the wheel, r is the radius of the wheel, and v is the speed at the hub of the wheel of the wheel.

The friction force acting at the contact point between the wheel and the ground is given by:

$$F_f = \mu F_n \tag{4.19}$$

where μ is the traction coefficient and F_n is the normal force between the wheel and the ground. The friction forces are represented as F_{frx} and F_{flx} in Figure 4.38.

In the literature, different friction force models can be found. However, the most widely used is the so called Magic Formula, or Pacejka model [37]. In this model, the friction coefficient depends on the slip. Different curves have been adjusted for different surface-tire interactions and are specific for each of them. In this study, the objective is to identify how the presence of wheel slip affects the dynamics of the vehicle. For this purpose, 3 fictitious surfaces where simulated using the Magic Formula: a high-friction, a medium-friction and a low-friction surface. According to Pacejka, the friction coefficient can be described by the following set of equations:

$$C = 1 + \left[1 - \frac{2}{\pi} \left(\arcsin \left(\frac{y_a}{D} \right) \right) \right] \tag{4.20}$$
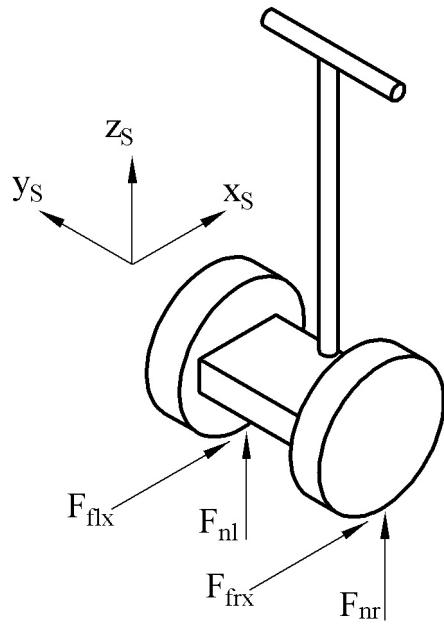
Figure 4.38: Friction forces acting on the wheels of the Segway.

$$E = \frac{\left[Bx_m - \tan\frac{\pi}{2c}\right]}{Bx_m - \arctan(bx_m)} \tag{4.21}$$

$$\mu = D\sin\left[C\arctan(Bs - E(Bs - \arctan(Bs)))\right] \tag{4.22}$$

where D is the maximum friction coefficient, x_m is the slip at which the maximum friction coefficient occurs, B is the slope of the curve at the origin, and y_a is the friction coefficient at high slips.. Although the Pacejka model can be applied for the self aligning torque and transverse friction forces, here the analysis is limited only to the force in the longitudinal direction, namely, the x-axis. It is assumed that there is no aligning moment (no slip angle), nor lateral forces actuating between the wheel and the ground. Only a vertical normal force, and a longitudinal friction force actuate between the wheel and the ground.

Based on the curves found in the works by Pacejka [37], different parameters were tested until three different friction models were obtained. These are shown in Figure 4.39. Table 4.8 shows the parameters used to generate each of the curves.
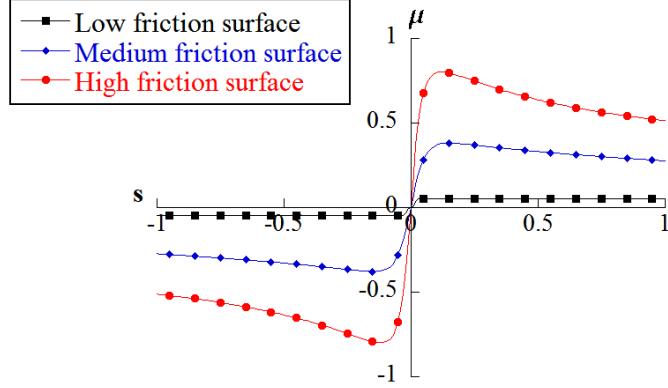
Figure 4.39: Fictitious friction curves.

Table 4.8: Parameters of the friction curves.

Curve	B	D	y_a	x_m
Low-friction	6.25	0.05	0.049	0.04
Medium-friction	9.5	0.38	0.01	0.15
High-friction	14	0.8	0.27	0.12

A new set of dynamic equations was generated in which the no slip constrain of the wheels was relaxed. This means that the contact point of the wheel with the ground has a non-zero velocity, which is called v_s. The new kinematic restriction is described by:

$$\dot{\theta}_w = \frac{v - v_s}{r} \tag{4.23}$$

The relative velocities of each wheel's contact point with the ground were defined as generalized velocities and a new dynamic model was developed. A simplified dynamic model was develop to study the effect of friction on both wheels while traveling in a straight path. A more complete model, that allows for the vehicle to turn left or

125

right, was used to study the effect of one of the wheels losing traction. These models are discussed in the next sections.

In summary, the simulations presented in this section work under the following assumptions:

- The basic assumptions presented in Chapter 2 except the wheels can no slip on the ground.

- A Rigid body model of the human rider.

- The vehicle can rotate at any desired yaw rate independent of the speed.

- Contact between the wheels and the ground is never lost, so the simulation vehicle cannot tilt sideways.

- There is no self-aligning torque between the wheel and the ground.

- The friction force acts in the longitudinal direction of the wheel, without a transverse component.

- In the two-wheel slipping simulations, both wheels are subject to the same friction model of the surface.

- In the one-wheel slipping simulations, the non slipping wheel rolls without sliding on the ground.

Simulations of a Segway traveling in a straight line were carried on to see how the dynamics of the system change when the wheels are allowed to slip on the ground. The effect of different surfaces, different initial speeds and different initial pitch angles are studied. It is assumed that initially, the Segway is not slipping and that there is perfect matching between the linear speed of the wheel hub and its angular speed.

Since the Segway is traveling along a straight path and the traction surface is the same on both wheels, a simplified model that does not turn left of right was developed. This allowed simulations to be carried in less time. The dynamic equations are:

$$\ddot{\theta}_p = r^2((m_b + m_p + 2m_w)(2T_y - gm_b(x_{wb}\cos(\theta_p) + z_{wb}\sin(\theta_p)) - gm_p(x_{wp}\cos(\theta_p) +$$
$$z_{wp}\sin(\theta_p))) - 2F_f(m_b(x_{wb}\sin(\theta_p) - z_{wb}\cos(\theta_p)) + m_p(x_{wp}\sin(\theta_p) - z_{wp}\cos(\theta_p))) -$$
$$(m_b(x_{wb}\cos(\theta_p) + z_{wb}\sin(\theta_p)) + m_p(x_{wp}\cos(\theta_p) + z_{wp}\sin(\theta_p)))(m_b(x_{wb}\sin(\theta_p) - z_{wb}$$
$$\cos(\theta_p)) + m_p(x_{wp}\sin(\theta_p) - z_{wp}\cos(\theta_p)))\dot{\theta}_p^2)/(2I_y(I_{by} + I_{py} + m_b(x_{wb}^2 + z_{wb}^2) + m_p(x_{wp}^2 +$$
$$z_{wp}^2)) - r^2((m_b + m_p + 2m_w + 2I_y/r^2)(I_{by} + I_{py} + m_b(x_{wb}^2 + z_{wb}^2) + m_p(x_{wp}^2 + z_{wp}^2)) -$$
$$(m_b(x_{wb}\sin(\theta_p) - z_{wb}\cos(\theta_p)) + m_p(x_{wp}\sin(\theta_p) - z_{wp}\cos(\theta_p)))^2));$$

$$\dot{v} = r^2((m_b(x_{wb}\sin(\theta_p) - z_{wb}\cos(\theta_p)) + m_p(x_{wp}\sin(\theta_p) - z_{wp}\cos(\theta_p)))(2T_y - gm_b(x_{wb}$$
$$\cos(\theta_p) + z_{wb}\sin(\theta_p)) - gm_p(x_{wp}\cos(\theta_p) + z_{wp}\sin(\theta_p))) - 2(I_{by} + I_{py} + m_b(x_{wb}^2 + z_{wb}^2) +$$
$$m_p(x_{wp}^2 + z_{wp}^2))F_{fz} - (I_{by} + I_{py} + m_b(x_{wb}^2 + z_{wb}^2) + m_p(x_{wp}^2 + z_{wp}^2))(m_b(x_{wb}\cos(\theta_p) +$$
$$z_{wb}\sin(\theta_p)) + m_p(x_{wp}\cos(\theta_p) + z_{wp}\sin(\theta_p)))\dot{\theta}_p^2)/(2I_y(I_{by} + I_{py} + m_b(x_{wb}^2 + z_{wb}^2) + m_p(x_{wp}^2 +$$
$$z_{wp}^2)) - r^2((m_b + m_p + 2m_w + 2I_y/r^2)(I_{by} + I_{py} + m_b(x_{wb}^2 + z_{wb}^2) + m_p(x_{wp}^2 + z_{wp}^2)) -$$
$$(m_b(x_{wb}\sin(\theta_p) - z_{wb}\cos(\theta_p)) + m_p(x_{wp}\sin(\theta_p) - z_{wp}\cos(\theta_p)))^2))$$

$$\dot{v}_s = -r^4((F_{fz} - T_y/r)((m_b + m_p + 2m_w + 2I_y/r^2)(I_{by} + I_{py} + m_b(x_{wb}^2 + z_{wb}^2) + m_p(x_{wp}^2 +$$
$$z_{wp}^2)) - (m_b(x_{wb}\sin(\theta p) - z_{wb}\cos(\theta p)) + m_p(x_{wp}\sin(\theta p) - z_{wp}\cos(\theta p)))^2)/(I_y(2I_y(I_{by} +$$
$$I_{py} + m_b(x_{wb}^2 + z_{wb}^2) + m_p(x_{wp}^2 + z_{wp}^2)) - r^2((m_b + m_p + 2m_w + 2I_y/r^2)(I_{by} + I_{py} +$$

$m_b(x_{wb}^2 + z_{wb}^2) + m_p(x_{wp}^2 + z_{wp}^2)) - (m_b(x_{wb}\sin(\theta p) - z_{wb}\cos(\theta p)) + m_p(x_{wp}\sin(\theta p) - z_{wp}\cos(\theta p)))^2))) - ((m_b(x_{wb}\sin(\theta p) - z_{wb}\cos(\theta p)) + m_p(x_{wp}\sin(\theta p) - z_{wp}\cos(\theta p)))(2T_y - gm_b(x_{wb}\cos(\theta p) + z_{wb}\sin(\theta p)) - gm_p(x_{wp}\cos(\theta p) + z_{wp}\sin(\theta p))) - (I_{by} + I_{py} + m_b(x_{wb}^2 + z_{wb}^2) + m_p(x_{wp}^2 + z_{wp}^2))(2T_y/r + (m_b(x_{wb}\cos(\theta p) + z_{wb}\sin(\theta p)) + m_p(x_{wp}\cos(\theta p) + z_{wp}\sin(\theta p)))\dot{\theta}p^2))/(r^2(2I_y(I_{by} + I_{py} + m_b(x_{wb}^2 + z_{wb}^2) + m_p(x_{wp}^2 + z_{wp}^2)) - r^2((m_b + m_p + 2m_w + 2I_y/r^2)(I_{by} + I_{py} + m_b(x_{wb}^2 + z_{wb}^2) + m_p(x_{wp}^2 + z_{wp}^2)) - (m_b(x_{wb}\sin(\theta p) - z_{wb}\cos(\theta p)) + m_p(x_{wp}\sin(\theta p) - z_{wp}\cos(\theta p)))^2))))$

The normal force between any of the wheels and the ground is given by:

$$F_{nz} = 0.5\mathrm{g}(m_b + m_p + 2m_w) + 0.5sin(\theta_p)(x_{wb}m_b\dot{\theta}_p^2 + m_p(xwp\dot{\theta}_p^2 - zwp\ddot{\theta}_p))$$
$$-0.5z_{wb}m_bcos(\theta_p)\dot{\theta}_p^2 - 0.5z_{wb}m_bsin(\theta_p)\ddot{\theta}_p \qquad (4.24)$$
$$-0.5cos(\theta_p)(x_{wb}m_b\ddot{\theta}_p + m_p(zwp\dot{\theta}_p^2 + xwp\ddot{\theta}_p))$$

Since there is no turning, it is safe to assume that the rider does not lean sideways. Assuming no rider motion, which is valid for the first instants after a disturbance occurs, the normal force between the rider and the transporter is given by:

$$F_{fz} = -0.5m_b(gcos(\theta_p) + sin(\theta_p)\dot{v} - z_{wb}\dot{\theta}_p^2 - x_{wb}\ddot{\theta}_p) \qquad (4.25)$$

First the effect of changing the initial speed was studied. The initial pitch angle was set to 10° and a medium-friction surface was used. The initial speed was changed for each case between 1 m/s and 4 m/s. Figure 4.40 shows the pitch response of the Segway. The initial speed does not play an important role in how well the Segway is able to balance itself. It is important to note that the Pacejka model does not account for the speed, whereas other models do. However, this effect is more noticeable at high speeds found in other types of vehicles [8].
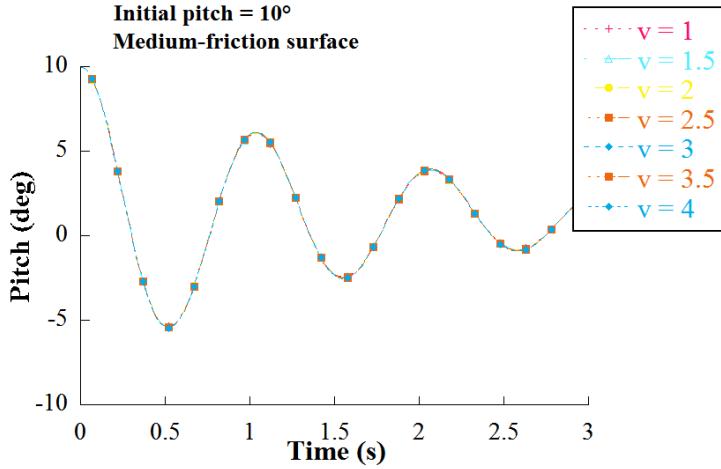
Figure 4.40: Pitch response at different initial speeds - loss of traction on both wheels.

Figure 4.41 shows the speed of the transporter. The dynamic characteristics of the response are not affected by the initial speed. However, the response translates according to the initial value along the speed axis of the graph.
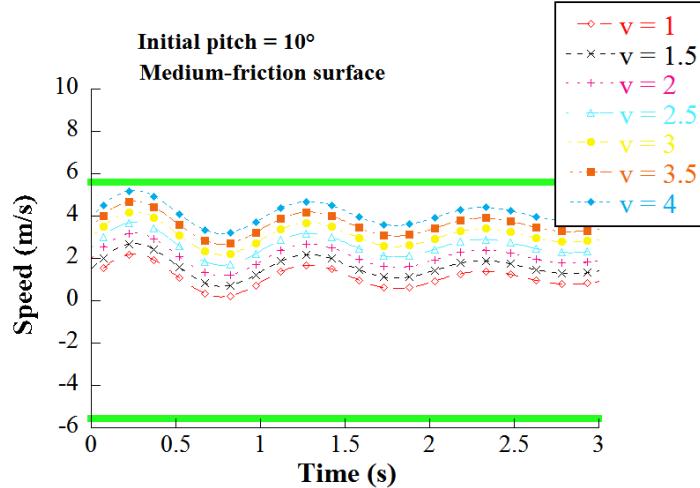
Figure 4.41: Speed response at different initial speeds - loss of traction on both wheels.

Figure 4.42 shows the normal force between the rider at the transporter. Even though there is some oscillation at the beginning, the value of the force does not decrease significantly, so the contact between the person and the vehicle is kept strong.

129
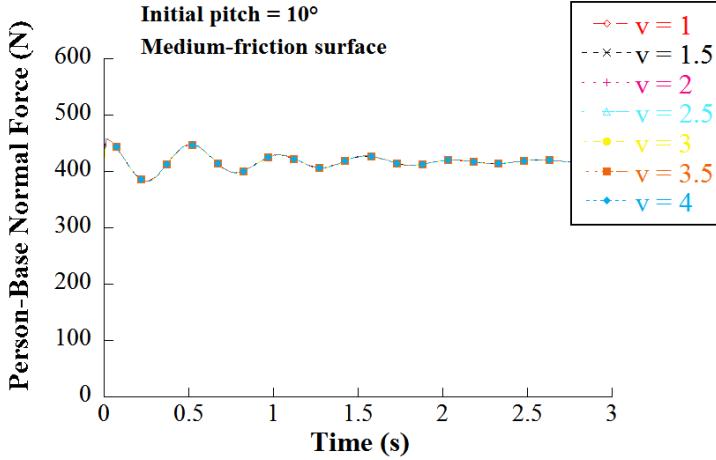
Figure 4.42: Person-base normal force response at different initial speeds - loss of traction on both wheels.

Following, the effect of different initial pitch angles is studied. The speed of the vehicle was set to 3 m/s and a medium-friction surface was used. The pitch angle was varied between 10° and 15°. The pitch response is shown in Figure 4.43. It shows that when the initial pitch is below 12° the vehicle balances without a problem. However, at higher pitch angles it becomes unstable. If the rider does not compensate for this, as in this simulation, the pitch increases past its safe limit. This shows the results of the available traction force being too small for the vehicle to change its speed fast enough and keep the system balanced. This is confirmed by the results in Figure 4.44 where in spite of the pitch increasing or decreasing away from the balanced position, the speed remained nearly constant.

Figure 4.45 shows the contact force between the Segway and the person. At higher pitch angles the force decreased and even dropped down to zero. This is a result of the tilting of the vehicle as well as the pitch angular speed. However, it must be noted that this occurred one second after it started traveling along the slick surface, which should be enough time for the rider to produce a different dynamic response by his reaction.
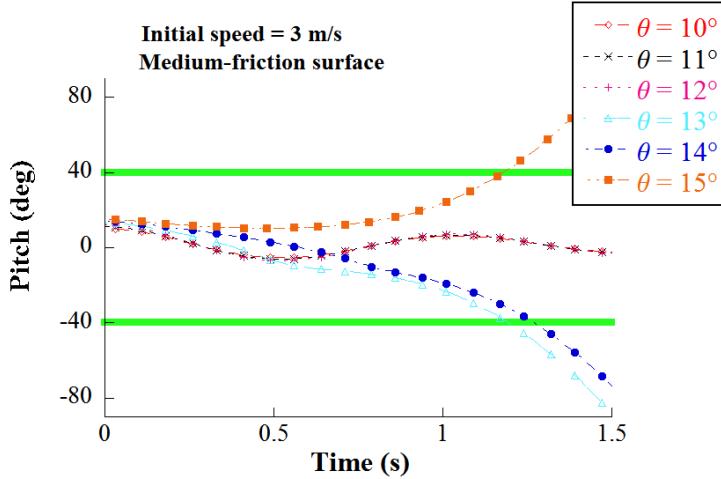
Figure 4.43: Pitch response at different initial pitch angles - loss of traction on both wheels.

The effect of different traction surfaces was studied. The simulation was done at an initial speed of 3 m/s and initial pitch of 15° and repeated with low, medium and high friction surfaces. Figure4.46 shows the pitch response for each surface. In the high friction surface, the vehicle was able to keep its balance. The medium and low friction surfaces didn't provide the necessary traction needed to control the pitch angle.

Figure 4.47 shows the speed response of the transporter. It shows how the speed initially increases in the high friction surface more than it does in the medium friction case. In the high traction case there is more available traction on the wheels so the transporter can be balanced. In the low friction case, the traction force is so low that the speed actually decreases and only increases back after 0.75 s.

Both the medium and low friction simulations were terminated earlier because contact between the Segway and the rider was lost, as shown in Figure 4.48. In the low friction case, contact was lost at 0.75 s of simulation time while it took around 1.25 s for this to happen in the medium friction case.
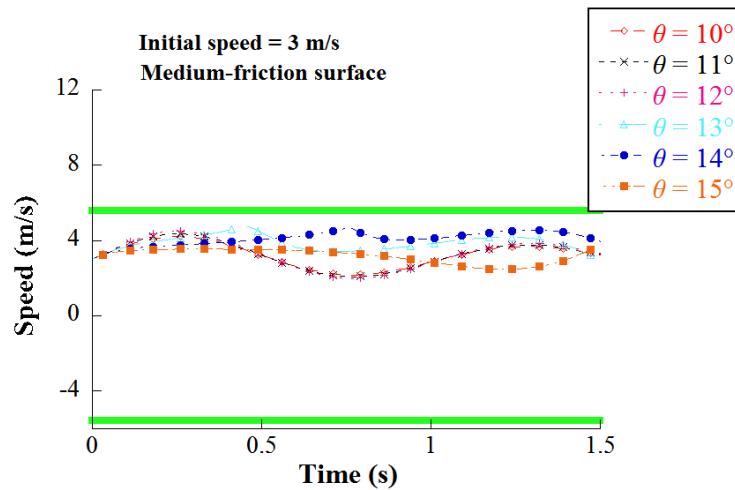
Figure 4.44: Speed response at different initial pitch angles - loss of traction on both wheels.
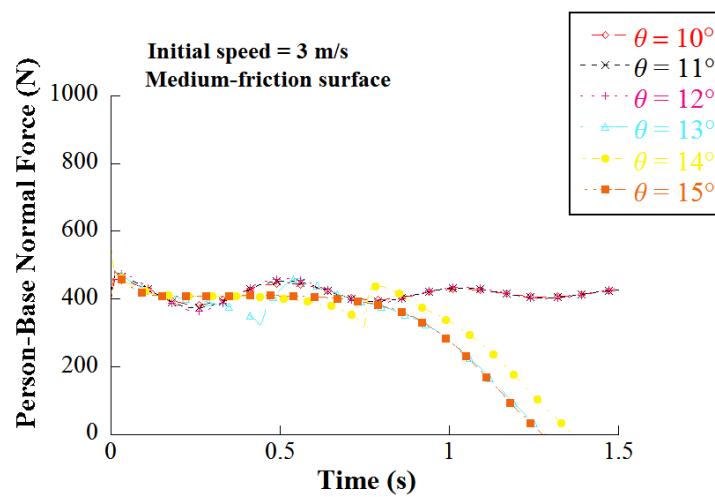
Figure 4.45: Base-person normal force response at different initial pitch angles - loss of traction on both wheels.
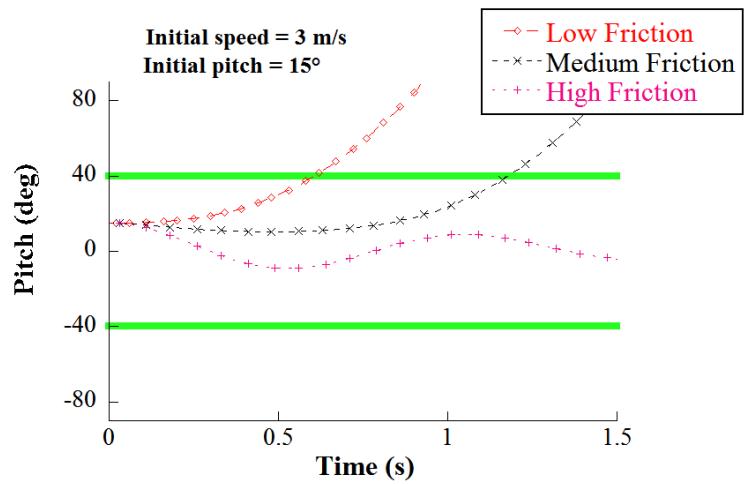
Figure 4.46: Pitch response at different traction forces - loss of traction on both wheels.
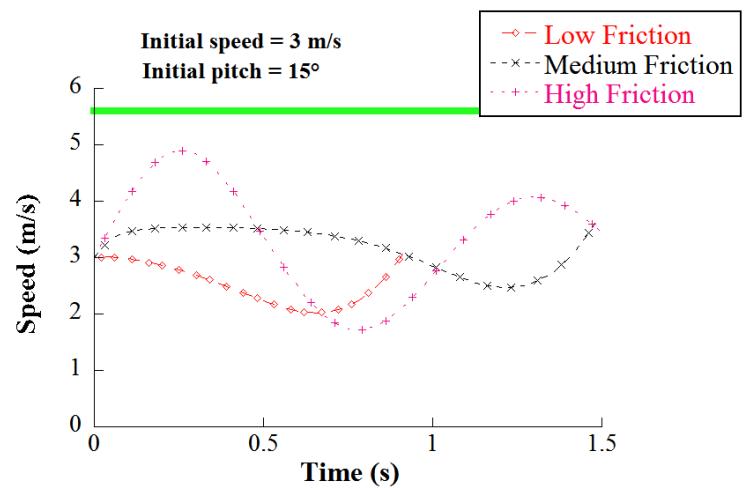
Figure 4.47: Speed response at different traction forces - loss of traction on both wheels.
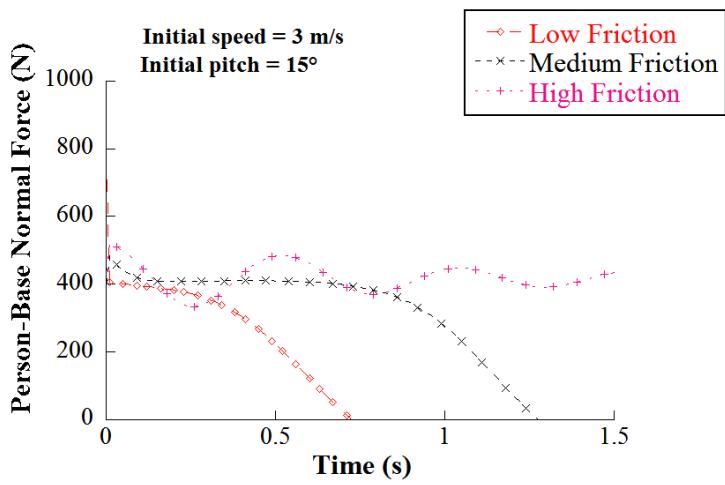
Figure 4.48: Person-base normal force response at different traction forces - loss of traction on both wheels.

A different set of simulations were run to study the effect of only one of the wheels losing traction with the ground. To do this, the no slip constrain was applied only to the left wheel, while the right slip was allowed to slip. Therefore, the angular speeds of the wheels are, given by:

$$\dot{\theta}_r = \frac{-(v_s - v - w\dot{\beta})}{r} \tag{4.26}$$

$$\dot{\theta}_l = \frac{(v - w\dot{\beta})}{r} \tag{4.27}$$

where v is the speed at the midpoint between both wheels, w is half the distance before both wheels, r is the radius of the wheels, and $\dot{\beta}$ is the turning rate of the vehicle.

The slip on the right wheel is given by:

$$s = \frac{\dot{\theta}_r r - (v + w\dot{\beta})}{v + w\dot{\beta}} \tag{4.28}$$

The relative velocity of the right wheel's contact point with the ground was defined as a generalized speed. This resulted in the dynamic equations that can be found in Appendix A.

Simulations were run with the initial conditions matching a situation in which the transporter would not be slipping. That means that the initial condition of the right wheel's angular speed was related to the wheel's hub speed by the no slip constrain. The effects of the initial speed, initial pitch angle and the traction surface were studied.

A set of simulations with an initial pitch angle of 5°, using a medium friction surface were performed at different initial speeds. Figure 4.49 shows the contact force between the right wheel and the ground for these cases. It is important to note that

the force initially decreases. For initial speeds of 2 m/s or higher the force becomes zero in less than 0.25 s. That is, the right wheel loses contact with the ground only after 0.25 s. This time is smaller as the speed increases. The simulations were terminated at the moment that contact with the ground was lost.
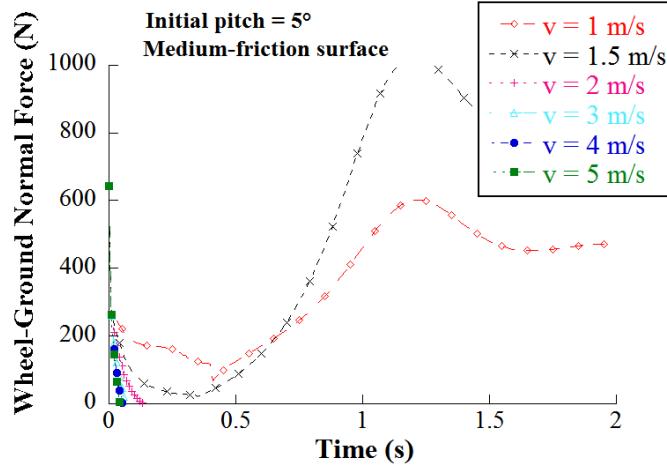
Figure 4.49: Wheel-ground normal force response at different speeds - loss of traction on the right wheel.

Figure 4.50 shows the pitch response of the transporter for different initial speeds. It shows that in the cases where the simulation was not terminated early due to loss of contact between the wheel and the ground, the controller was able to achieve balance in the pitch direction. Another visible effect was that the amplitude of the oscillation increased with higher initial speeds.

Figure 4.51 shows the speed response. In the cases were the simulation was not terminated due to wheel-ground contact loss, the speed stayed within close bounds to its initial value. An increase in initial speed only caused the entire speed response to translate in the positive direction of the speed axis.

Figure 4.52 shows the yaw rate response for each initial speed case. It is seen that at the start, when the no-slip constrain between the right wheel and the ground is lost, the transporter starts to turn towards the right (negative yaw rate). The graph also shows that the left turning rate increased as the initial speed increased. A static
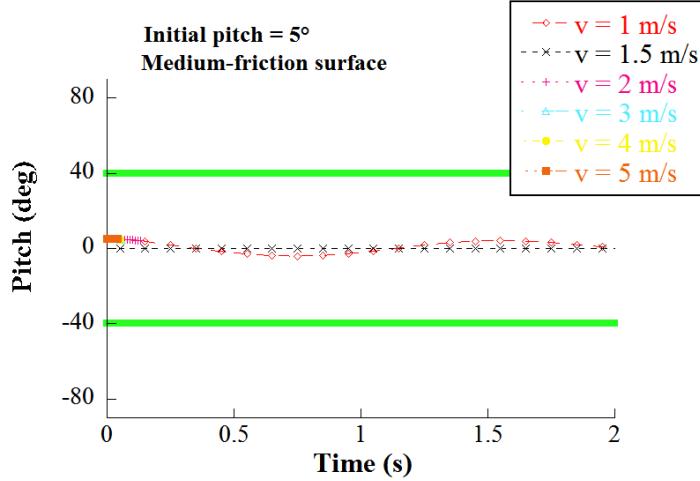
Figure 4.50: Pitch response at different speeds - loss of traction on the right wheel.
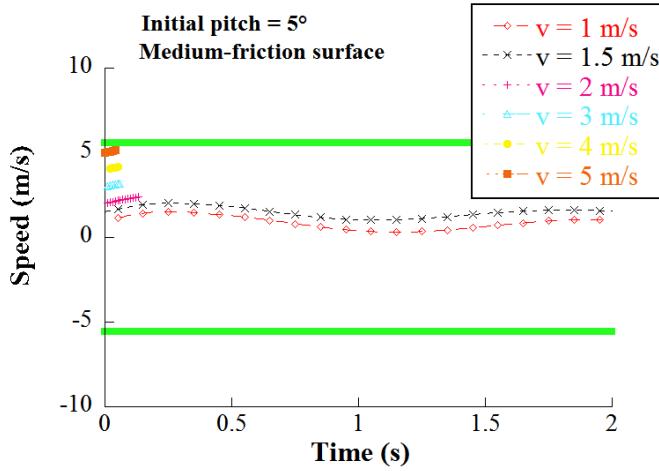
Figure 4.51: Speed response at different speeds - loss of traction on the right wheel.

analysis of a mass with two supports on the ground traveling along a circular trajectory yields that the normal force on the right support is given by $m_{vehicle}\left(g + \frac{1}{2w}v\dot{\beta}\right)$. Therefore, the force is reduced as the turning rate negatively increases. This means that the results shown in Figure 4.52 and Figure 4.49.

The effect of the initial pitch angle is studied next. A medium friction surface was used and the initial speed was set to 1.5 m/s. Higher speeds did not allow to study different characteristics in the dynamic response because the Segway would lose contact with the ground very early in the simulation. Figure 4.53 shows the
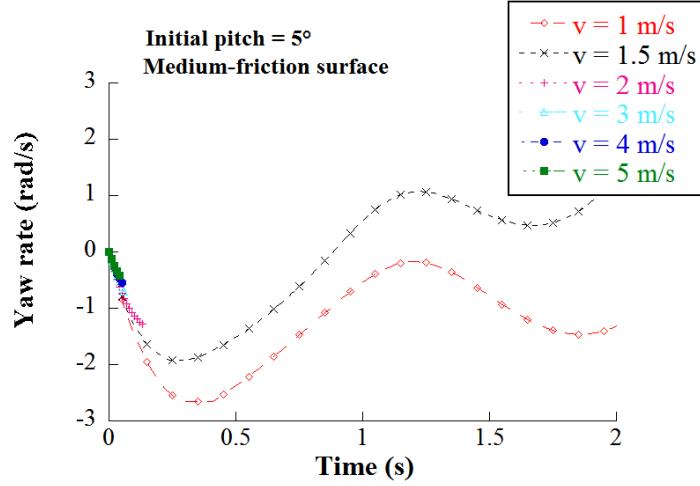
Figure 4.52: Yaw rate response at different speeds - loss of traction on the right wheel.

pitch response for different angles. The 10° case was terminated almost from the start because the normal force dropped to instantly, as will be discussed later. The 0° and 8° cases were also terminated early. It must be noted, though, that the real equilibrium angle of the pendulum is 1.2°. This means that an initial pitch just 1.2° below the balanced position, like 0°, caused the device to fail.

Figure 4.53 shows that in all cases were ground contact was not terminated early, the pitch oscillation amplitude increased as the initial pitch was increased.
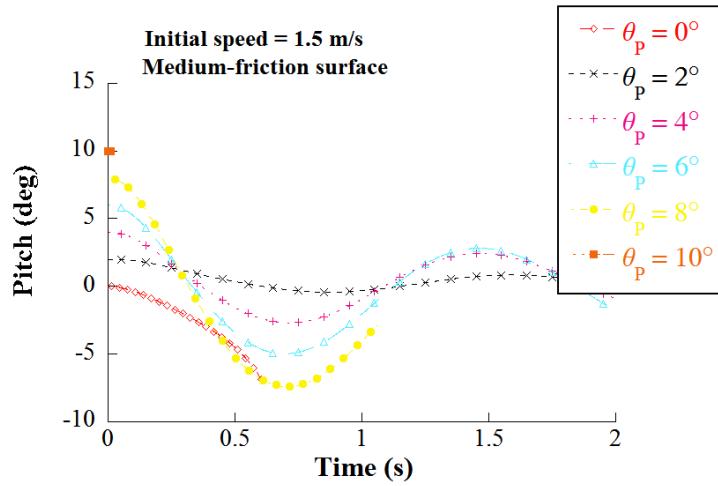
Figure 4.53: Pitch response at different initial pitch angles - loss of traction on the right wheel.

Figure 4.54 shows the speed response at different initial pitches. It shows that regardless of the initial pitch, the speed remained very close to the initial value. The same effect that was observed when the initial speed was modified.
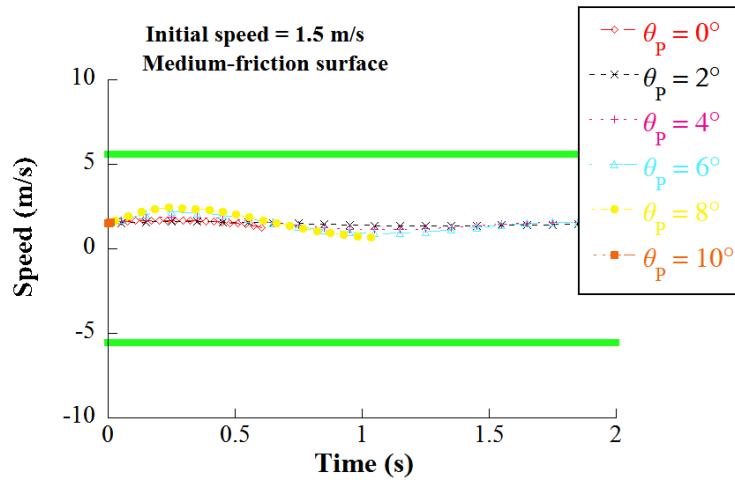
Figure 4.54: Speed response at different initial pitch angles - loss of traction on the right wheel.

Figure 4.55 shows the yaw rate response for different initial pitch angles. All the yaw rates initially decrease (the vehicle turns to the right), except for the 0° (turns to the left). So the difference between the initial pitch and the equilibrium pitch affects the yaw rate both in magnitude and direction. If the transporter is tilted forward, losing traction in the right wheel will cause the vehicle to turn right. To the contrary, it will turn left if it is tilted backwards. In none of the cases presented here was the transporter able to stabilize in the yaw direction within simulation time.
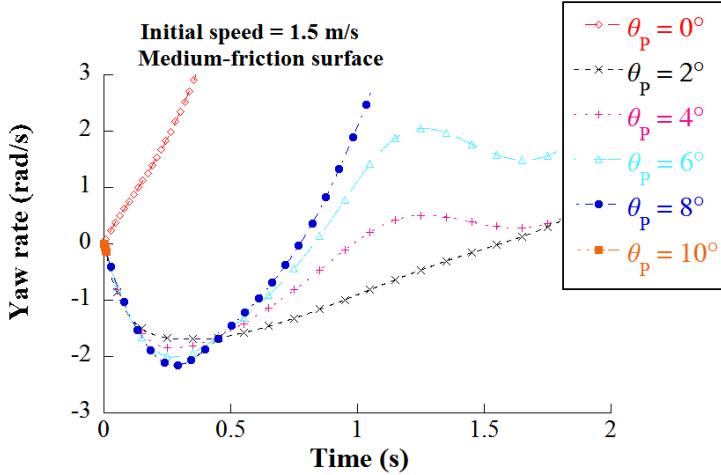
Figure 4.55: Yaw rate response at different initial pitch angles - loss of traction on the right wheel.

Figure 4.56 shows the normal force between the right wheel and the ground. For almost all cases, it decreased abruptly at the beginning of the simulation. In the 10° initial pitch case it almost instantly drops to zero. In the other cases, except for an initial pitch of 0°, it gets very close to zero but then increases back. It is interesting to note that in the 8° the normal force on the right wheel didn't go below zero, and the contact loss occurred in the left wheel instead, as shown in Figure 4.57. In the 0° initial pitch case (which is less than the equilibrium pitch), the force initially increased but then decreased below zero afterward, and contact with the ground was lost. Figure 4.57 shows that contact was not lost in the left wheel during the simulation of the 0° initial pitch case.

Next, the initial pitch was set to 4° and the intiial speed to 3 m/s. Then, simulations were run using different traction surfaces. The simulations were terminated when the contact force of any of the wheels with the ground dropped to zero. Figure 4.58 shows the pitch response. In all cases the pitch did not increase significantly away from the equilibrium pitch. The low and high friction cases failed before the simulation time ended. However, the medium friction case didn't. This indicates that

140
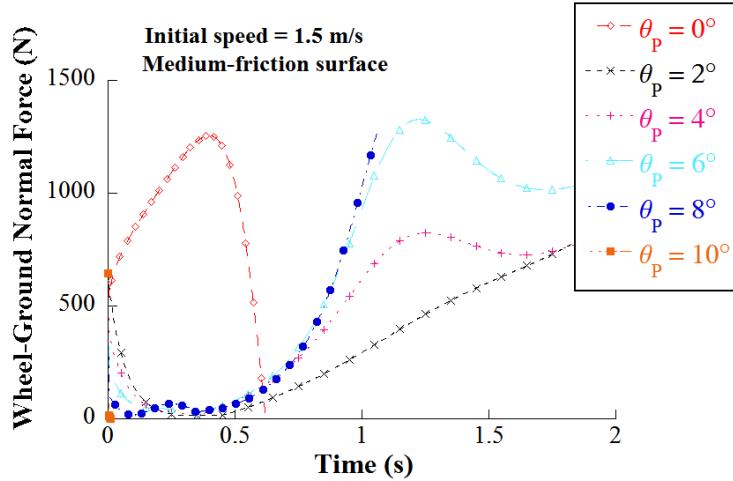
Figure 4.56: Wheel-ground normal force response at different initial pitch angles - loss of traction on the right wheel.

besides the friction coefficient magnitude, other characteristics of the friction model might play a role.

Figure 4.59 shows the speed response for the same cases. The speed does not deviate considerable from its initial value.

Figure 4.60 shows the yaw rate response. At the beginning, the yaw rate became negative (the vehicle turns to the right). It was noted that the higher the friction force, the higher was the right turning rate. However, after reaching a minimum, the yaw rate increases and the turning rate becomes positive (turning to the left). Then the turning rate kept increasing until the contact between the left wheel and the ground is lost. It is interesting to note that the high friction curve intersected with both the medium and low friction cases. The important fact to note is that the loss of traction in one of the wheels yields unstable responses in the yaw direction.

The normal force between the right wheel and the ground is shown in Figure 4.61.

It is important to note also that at higher pitch angles and higher speeds failure occurs earlier in time. The previous simulations were repeated at an initial pitch of 4° and initial speed of 3 m/s. Figure 4.62 shows the right wheel contact forces with
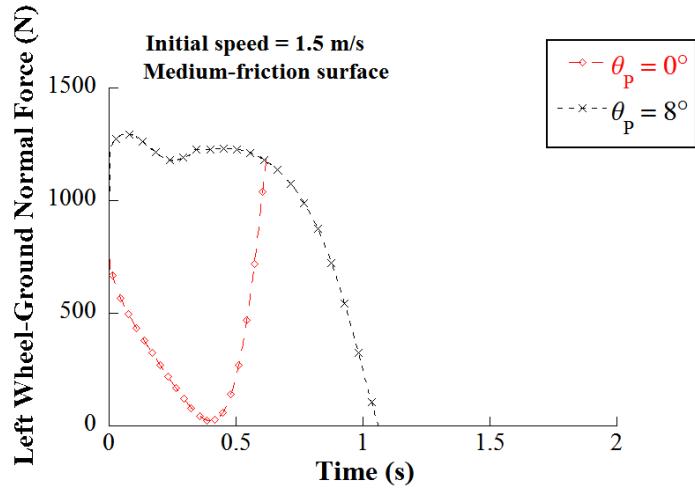
Figure 4.57: Left wheel-ground normal force response at different initial pitch angles - loss of traction on the right wheel.

the ground. It shows how just a slight increase in pitch and speed made the vehicle lose traction within tenths of seconds.
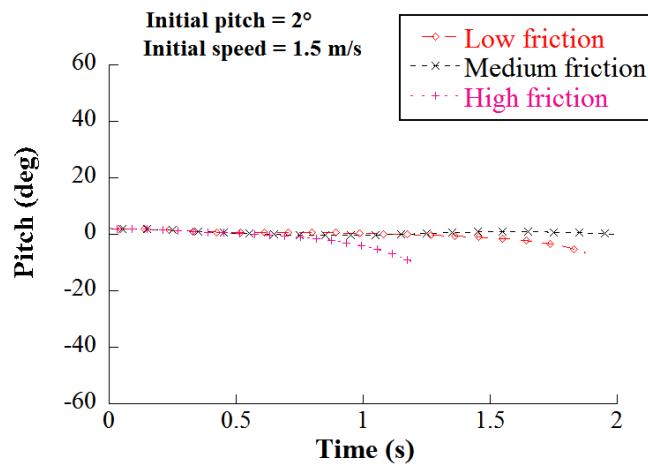
Figure 4.58: Pitch response at different traction forces - loss of traction on the right wheel.
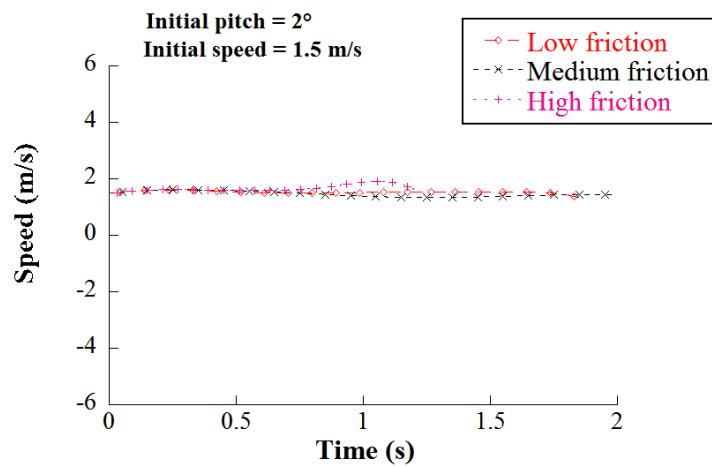
Figure 4.59: Speed response at different traction forces - loss of traction on the right wheel.
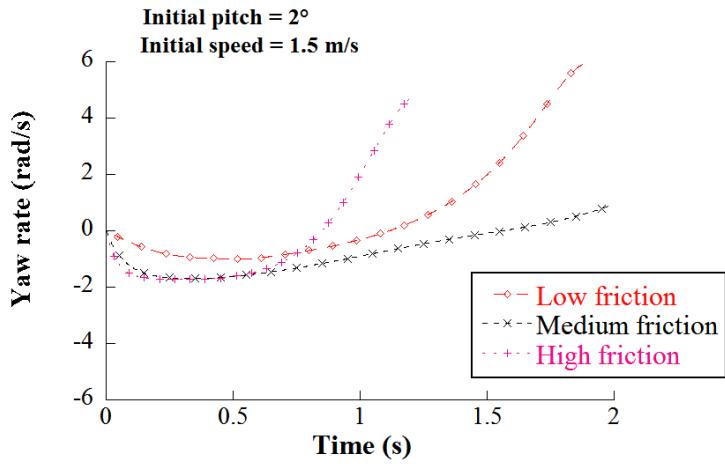
Figure 4.60: Yaw rate response at different traction forces - loss of traction on the right wheel.
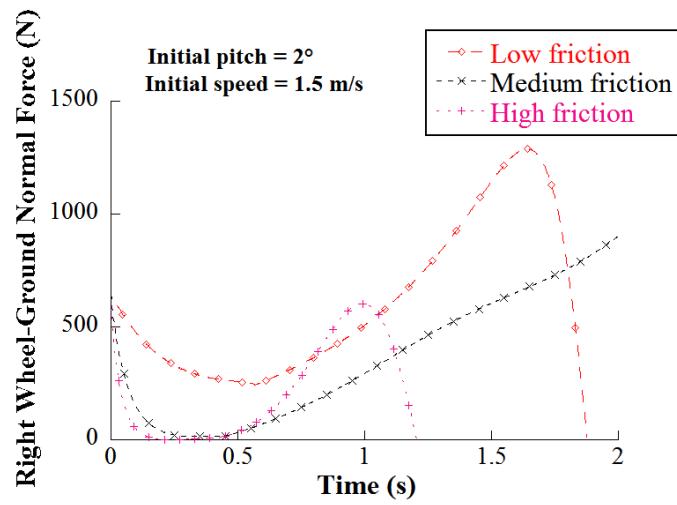
Figure 4.61: Right Wheel-ground normal force response at different traction forces - loss of traction on the right wheel.
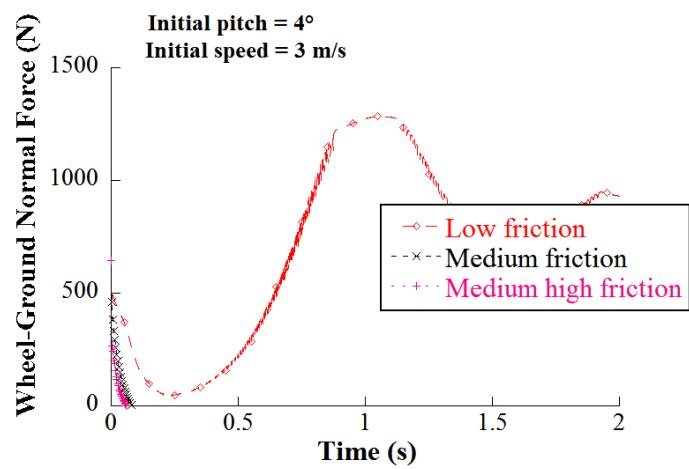
Figure 4.62: Right Wheel-ground normal force response at different traction forces - loss of traction on the right wheel at higher speeds and pitches.

4.2.4   Disturbance forces simulations

Two types of disturbance forces where applied on the model of the transporter. These forces were: a disturbance force applied on the handlebar of the Segway, and a disturbance force applied on the left wheel of the Segway. These simulations are described in more detail in the following sections.

In summary, the limitations of the disturbance force simulations are:

- All the assumptions presented previously in Chapter 2 regarding the two-wheeled inverted pendulum.

- In the central disturbance force cases, the force was a step function with a duration of 0.02 s and applied horizontally on the handlebar.

- A rigid body model of the human rider.

4.2.4.1   Central Disturbance

A force was applied on the handlebar of the Segway model, as shown in Figure 4.63. Because the base of the Segway, the handlebar, and the person experience no relative motion with respect to each other, the force was located on the pendulum body by using a vector from the midpoint between the wheels .

Different initial pitch angles and speeds conditions were assumed and the applied force was varied from 0 N to 5000 N. The force was a constant pulse with a duration of 0.2 s. The initial pitch angles were -40°, -20°, 0°, 20° and 40°. The initial speeds were 0 m/s, 2 m/s and 4 m/s. The force was applied on the handlebar at a height of 1 m from the base of the Segway. The transporter falls forward as the pitch angle increases.

The criteria for failure are:

- Speed above 12.5 mph

- Pitch angle above within $\pm 40°$

146

- Ground-Segway normal equal zero.

- Segway-rider normal forces equal zero.

The times at which these failure conditions were detected were plotted against the magnitude of the disturbance force. When no failure condition occurred before the simulation ended, no failure time was recorded for that case.
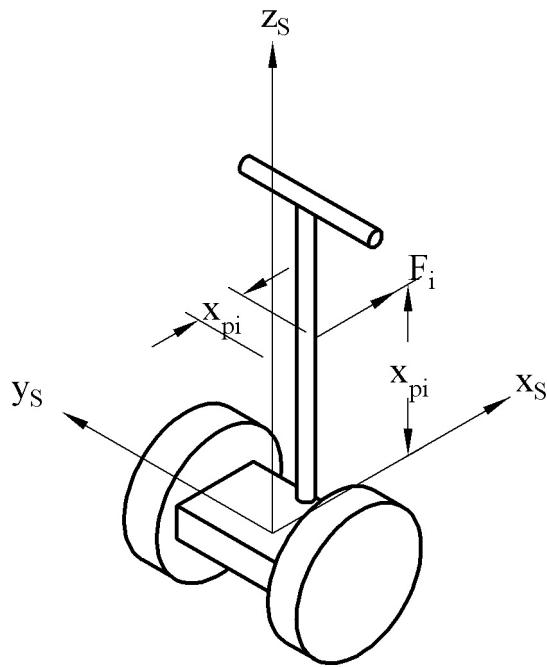
Figure 4.63: Disturbance force acting on the handlebar of the Segway.

Figure 4.64 shows the maximum oscillation amplitude of the pendulum. Each graph corresponds to one initial speed, and each curve corresponds to a specific initial pitch angle for that particular speed. At low forces, the maximum pitch angle increases gradually with an increase in the applied force. In the case where the initial pitch is -20°, this increase occurs until the force approaches values between 2kN and 3 kN. For these forces, the maximum pitch exceed 90°. This means is that when the force is strong enough, the Segway hits the ground before being able to regain balance. In the case of the -40° initial pitch, this happened at around 3000 N. For

147

the other cases at 0 m/s initial speed, the Segway was able to regain balance before hitting the ground.

Comparing the 2m/s case with the 4 m/s shows that as the speed of the Segway increases, a smaller force is needed to destabilize it. For example, in the case corresponding to an initial pitch of 20° and an initial speed of 2 m/s a force of around 2.5 kN destabilized the transporter, while at 4 m/s initial speed, the force was only 2 kN. Both cases showed that a negative initial pitch value makes it easier for the transporter to become unstable.
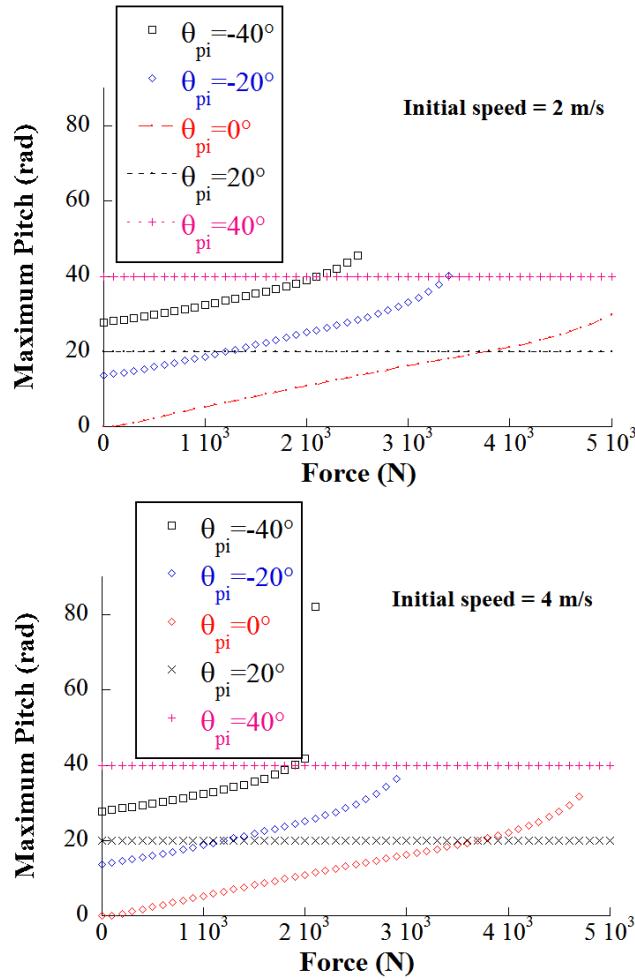
Figure 4.64: Maximum Pitch vs. Force.

Figure 4.65 shows the period of oscillation for the same sets of initial conditions and the same forces as previously described. The oscillation period increases steadily

before the pitch exceeds the value at which the transporter would hit the ground. Both graphs on Figure 4.65 show that at higher pitch values, the oscillation period remains constant, regardless of the force being applied. However, very negative initial pitch values cause the period to increase significantly as the applied force gets stronger.
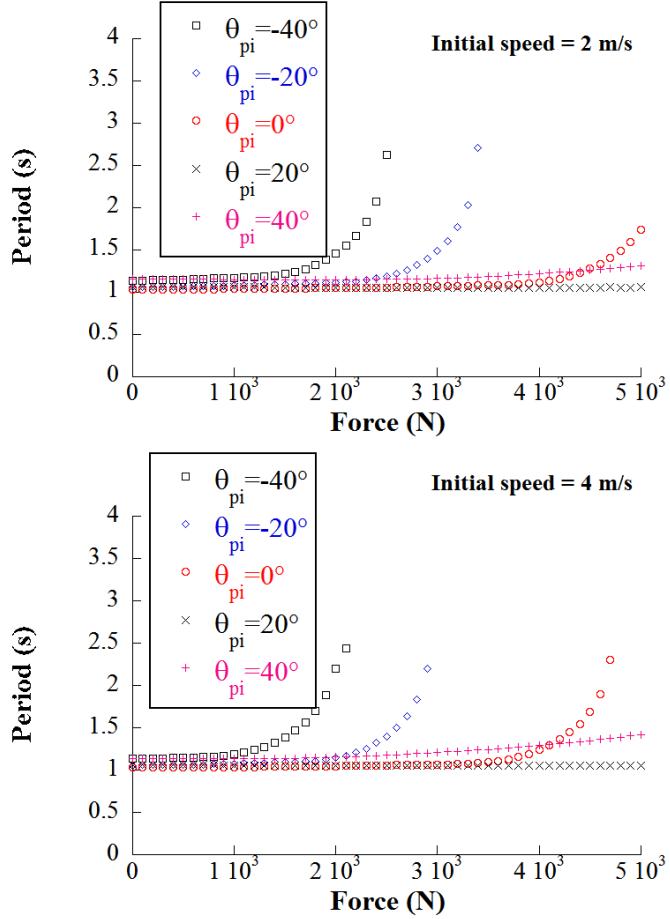
Figure 4.65: Oscillation vs. Disturbance.

Figure 4.66 shows the time at which the maximum pitch is reported. The cases where the model Segway hit the ground before regaining balance are identified by the data before the end of the graph. As shown in these curves, the maximum pitch always occurred between 0.5 and 1 s after the force was applied. This means that for a strong enough force, the Segway will crash against the ground in less than 1 second.

The maximum pitch time depends on the initial pitch. As the initial pitch increases, the time of the maximum pitch also increases. This can be observed in both graphs in Figure 4.66. The initial speed does not significantly affect how long it takes for the maximum pitch to be reached. Changing the initial speed only translates the curves towards the left on the Force axis.

150
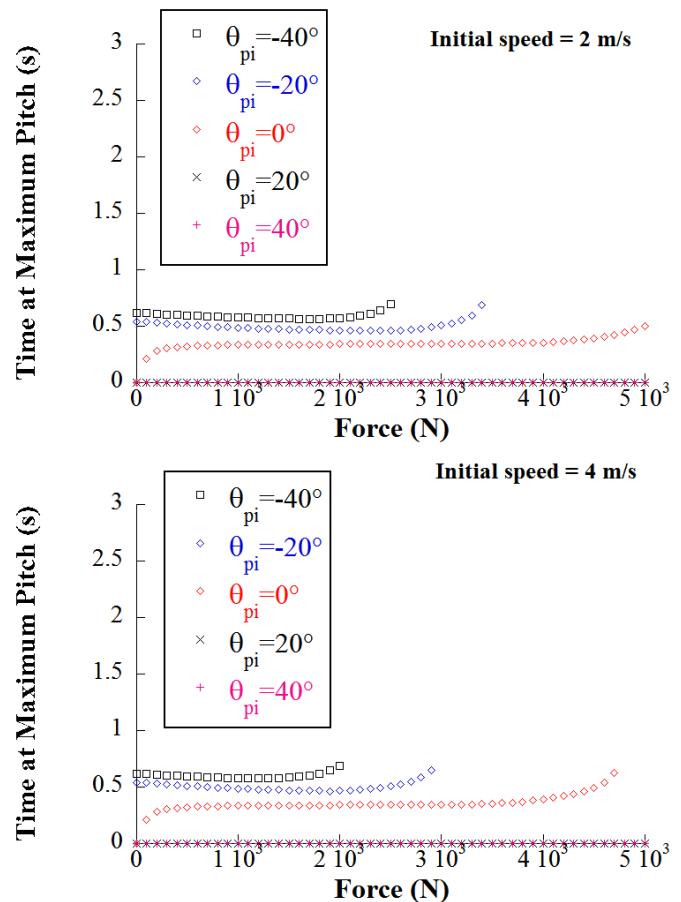
Figure 4.66: Time at which maximum pitch occurs.

Figure 4.67 shows the time at which the pitch limit angle of 40° is reached after the disturbance force is applied. When the initial speed was 2 m/s, this limit was only reached for initial pitch angles of -20° and -40°. In the case where the initial speed was 4 m/s, the 0° initial pitch angle case also exceeded the pitch limit. The pitch limit angle was reached slightly before the maximum pitch angle. This can be observed by comparing curves in Figure 4.66 with those in Figure 4.67.
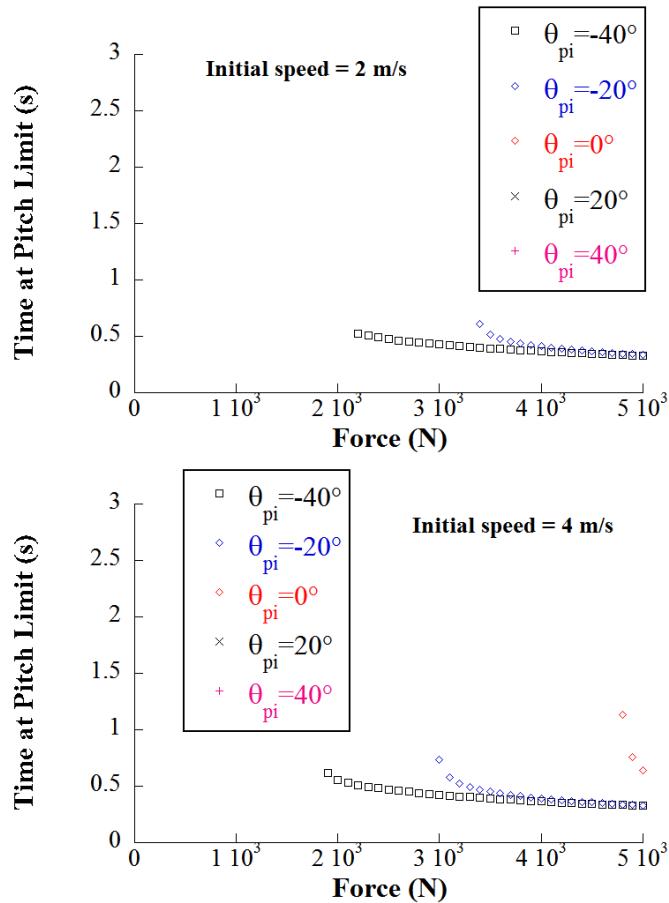
Figure 4.67: Time at which pitch limit is reached.

Figure 4.68 shows the time at which the Segway speed limit of 12.5 mph was reached. The speed limit is reached at smaller forces and at shorter times than the pitch limit. The speed limit is reached when the initial pitch angle is positive. Remember that the controller compensates for positive pitch by accelerating the vehicle. At negative pitch angles, the speed does not increase significantly with the applied

force. At higher speeds, a smaller force is needed in order for the vehicle to reach the speed limit. This can be observed by comparing both graphs in Figure 4.68.
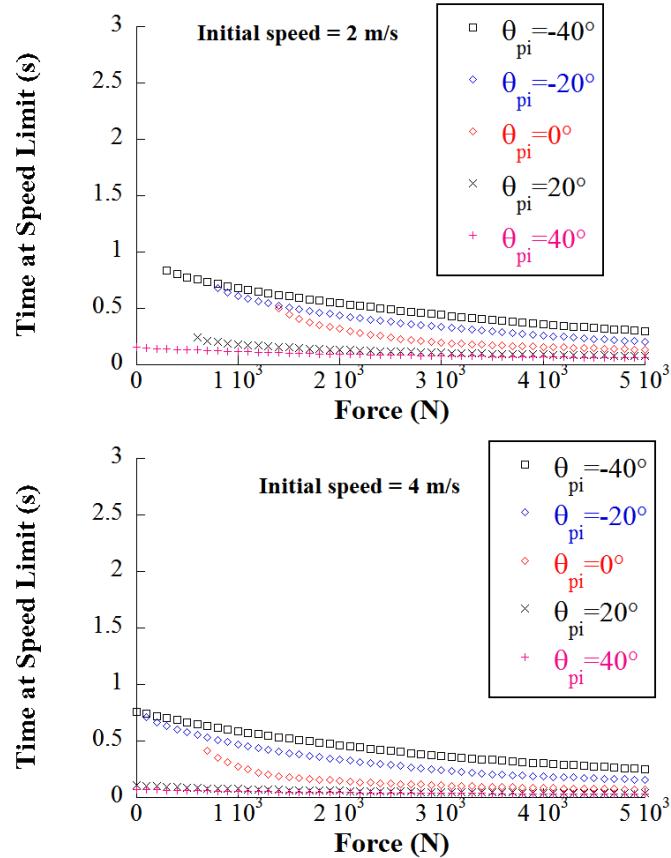
Figure 4.68: Time at which speed limit is reached.

Figure 4.69 shows the failure time for each case. Failure time is the earliest time during the simulation at which a condition of failure arose, whether it was an excess pitch angle, high speed limit, a zero contact force between the vehicle and ground, or a zero contact force between the vehicle and rider. In most cases, the failure cause was exceeding the speed limit.
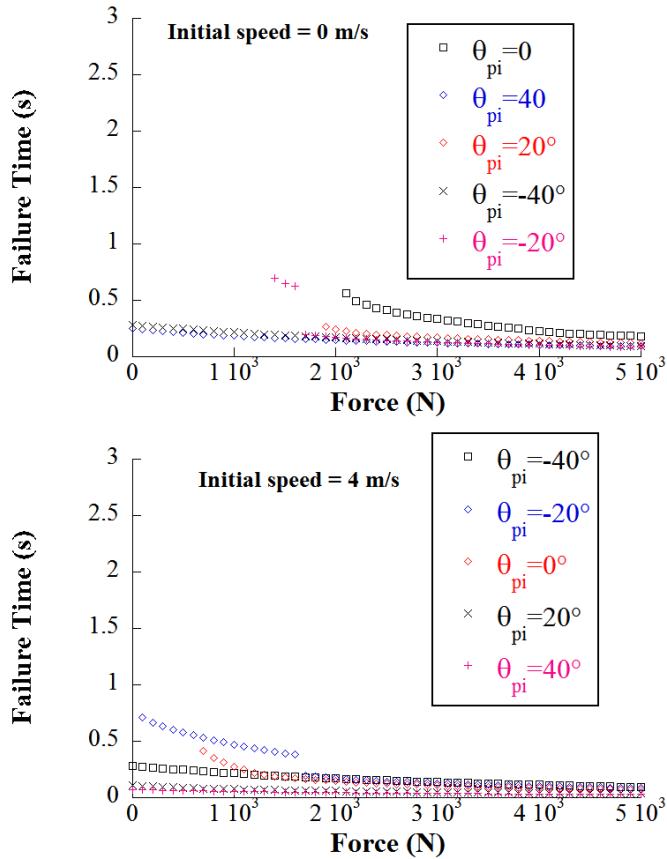
Figure 4.69: Time at Failure.

Figure 4.70 shows the distance traveled by the Segway before a condition of failure occurred. It can be noticed, in most cases, how the distance traveled increases as the force increases. However, a point is reached for each case when the distance drops dramatically. This means a condition of failure occurred very quickly. In the simulation code, the failure time also accounted for the points at which wheel-ground and rider-base dropped to zero. These are the cases when the Segway fell down.

The way to determine this is if any normal force is found to be zero before the pitch limit, or the maximum pitch was reached. This indicates a normal force of zero while the Segway still trying to balance itself. The reason why this can occur is that the person is not only standing on the Segway but is also rotating as it falls down. If this rotation is fast enough, the person will be thrown off the Segway. This happens because the contact force is a compression force, and cannot pull the person towards the vehicle. If the vehicle also accelerates in a direction opposite to which it is rotating, the effect can be aggravated.

Figure 4.71 shows the time at which the normal forces between the base of the Segway and the rider become zero. It is assumed that the rider does not do any relative movements with respect to the Segway. It shows that for some initial pitch angles, -40°, -20° and 40°, these normal forces become zero at around 0.25 s after the disturbance was applied. As noticed in Figure 4.64, for forces below 2000 N, the Segway did not crash to the ground, and the pitch did not exceed 90° (~1.57 rad), which means that the person lost support from the Segway before the Segway was completely tilted down.
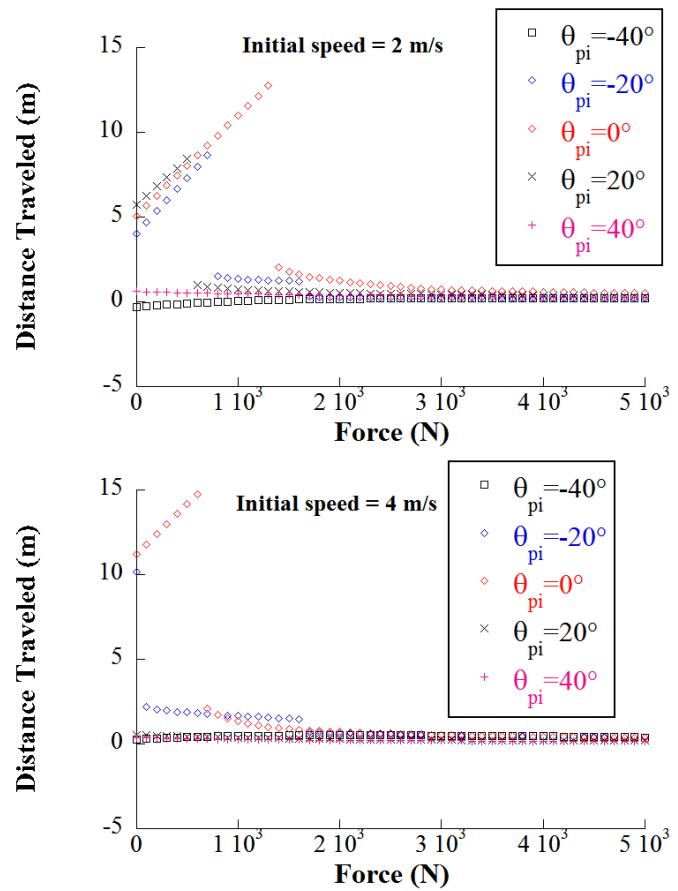
Figure 4.70: Distance traveled before failure.
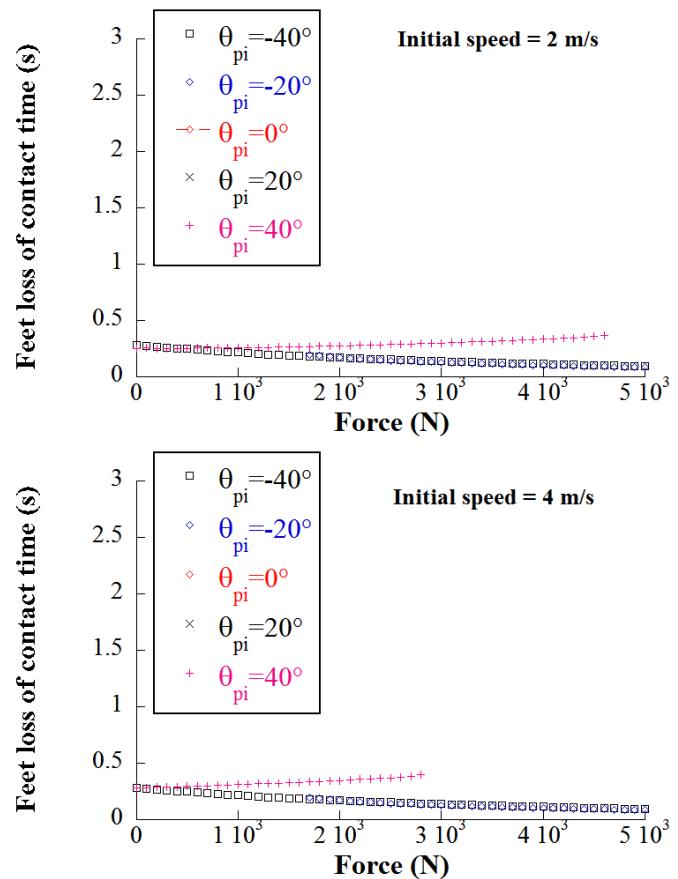
Figure 4.71: Rider-Segway Forces

4.2.4.2 Disturbance on wheel

A force was applied on the left wheel of the Segway model as shown in Figure 4.72. The force was located x_{lb} in front of the center of the wheel and z_{lb} above it. The components of the force were approximated by those measured on the bump tests performed on the Segway i2, as described before. . The forces were defined as a half sine pulse with a duration of 0.1 s, and peak magnitudes in the X,Y and Z axes of 594 kN, 561 kN, and 792 kN. These values were calculated by using the peak accelerations measured during the medium speed bump test. They then were multiplied by the mass of the Segway-rider system, 132 kg.

It is important to note that this simulation restricts the Segway to travel along the ground plane. For this reason, even if the vertical force is big enough to lift the Segway off the ground, the simulation will not represent this behavior.
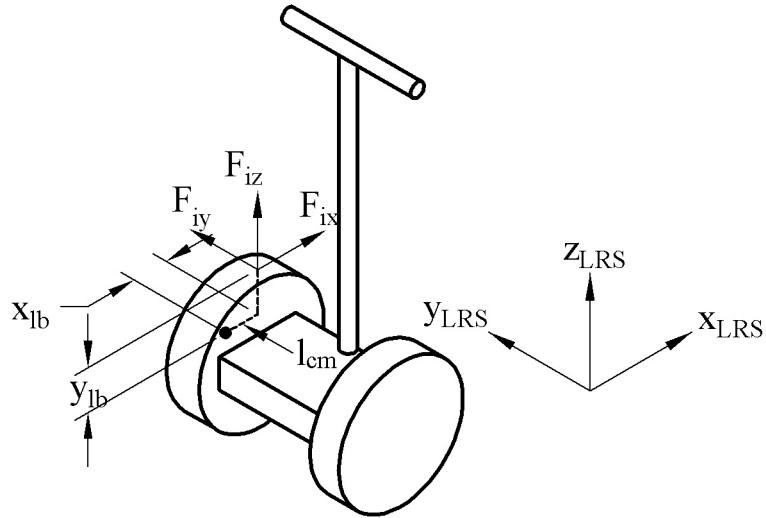
Figure 4.72: Disturbance force acting on a wheel.

Figure 4.73 shows the maximum pitch angle reached by the Segway after the disturbance force was applied on its left wheel. The graph shows the results for different initial pitch angles and initial speeds. It is important to note that any pitch angle above 1.57 (90°) means that the person-pendulum set is below ground level.

158

Therefore, as it is shown in Figure 4.73, the Segway fell down to the floor (the pitch exceeded 90°) for all the cases when the initial pitch angle was greater than or equal to -20°. This means the Segway can better resist these kind of disturbances when it is tilted backwards. It is interesting to note that the initial speed did not have an effect on the maximum pitch.
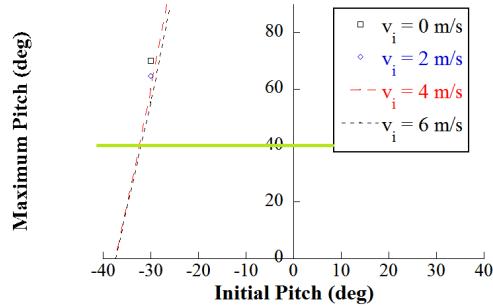
Figure 4.73: Maximum pitch angle.

Figure 4.74 shows the time at which the maximum pitch occurred. Unlike the period of oscillation, in this case, the time at which the peak pitch occurred is influenced by the initial pitch angle, with the time increasing as the pitch angle increases. This is taking into account only the cases where the Segway did not crash against the ground (initial pitch of -40° and -30°). Again, the speed did not seem to affect the time of the maximum pitch angle.
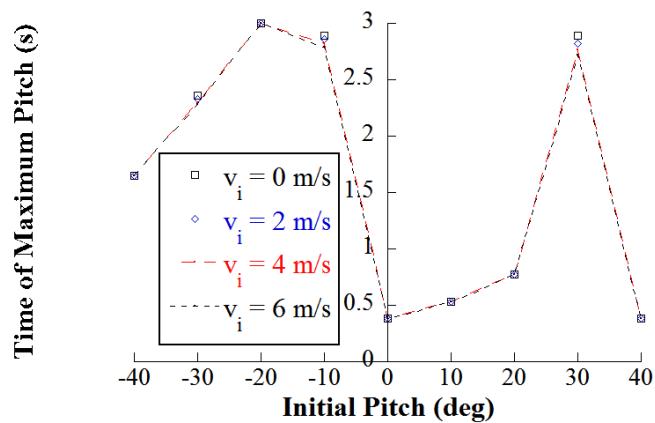
Figure 4.74: Time at which maximum pitch occurred.

159

Figure 4.75 shows the time at which the pitch limit of 40° is reached. For an initial pitch of -40°, the pitch limit was not reached at all. For the rest of the cases, the ones with negative initial pitch angles, the pitch limit was reached around 2 seconds into the simulation. For the cases when the initial pitch angle was zero or positive, the pitch limit was reached almost immediately after the force was applied on the wheel. The speed did not affect this time either. This means that when the rider is about to hit a bump, it can be beneficial to lean backwards in order to make the vehicle more robust to it.
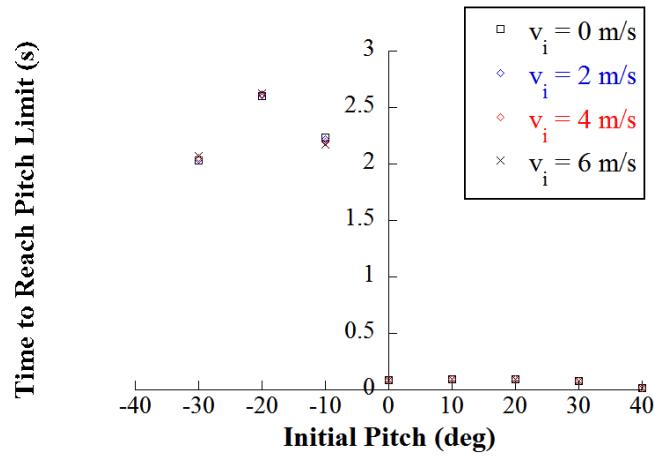
Figure 4.75: Time at which pitch limit is reached.

Figure 4.76 shows the time at which the speed limit was reached after applying the disturbance force on the wheel. The case where the initial speed is 6 m/s is not shown, because 6 m/s is above the speed limit of 12.5 mph. For the other cases, the speed limit is reached before the maximum pitch occurred, as can be noticed by comparing Figure 4.74 and Figure 4.76. However, this is not the case for the 10° initial pitch case, where the speed limit was not reached during the simulation at all.

It was noticed that the pitch limit is reached before the speed limit when the initial pitch angle is positive. This is visible when comparing Figures 4.75 and 4.76. It is important to note that even when the speed limit is reached before the pitch limit, the Segway would still fall over.

160
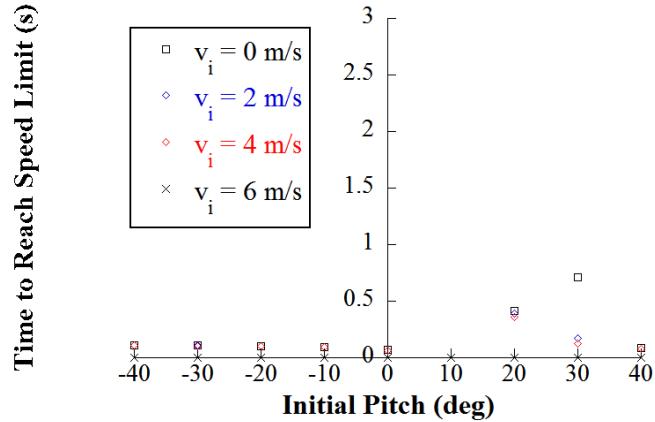
Figure 4.76: Time at which speed limit is reached.

Figure 4.77 shows the time at which contact is lost between the rider feet and the base of the Segway. Both feet lose contact almost immediately after the disturbance force is applied. However, it is interesting to note that the order in which this happens depends the initial pitch angle. If the initial pitch angle is less or equal than -20°, then contact is first lost on the right foot. The opposite occurs for angles greater than -20°. These results are limited in accuracy by the simulation restricting the trajectory of the Segway wheels to travel in a plane parallel to the ground.

Figure 4.78 shows the simulation time at which the normal force between the wheels and the ground becomes zero. In all cases, the left wheel lost contact almost immediately after the disturbance force was applied. The right wheel lost contact later in time as the initial pitch angle was increased, and this time reached a maximum when the initial pitch was 10°.

When the initial pitch angle was greater than -20°, the right wheel was able to maintain contact with the ground for some time after the left wheel lost contact. This explains why when the initial pitch angle was greater than -20°, the right foot lost contact after the left foot.

Figure 4.79 shows the global failure time, which is the time at which the first condition of failure was detected. This takes into account the Segway-ground and
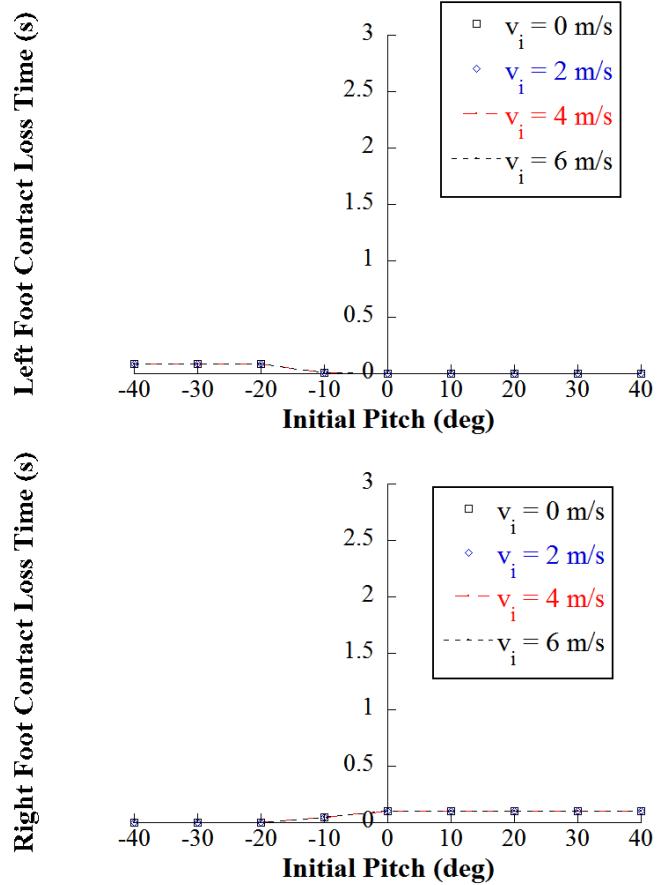
Figure 4.77: Time of contact loss at each foot.

rider-base normal forces. As seen, the first condition of failure is always detected almost immediately after the disturbance is applied. The largest time before a failure was detected occurred in the initial pitch angle of 20° case, in which the failure time was 0.125 s.
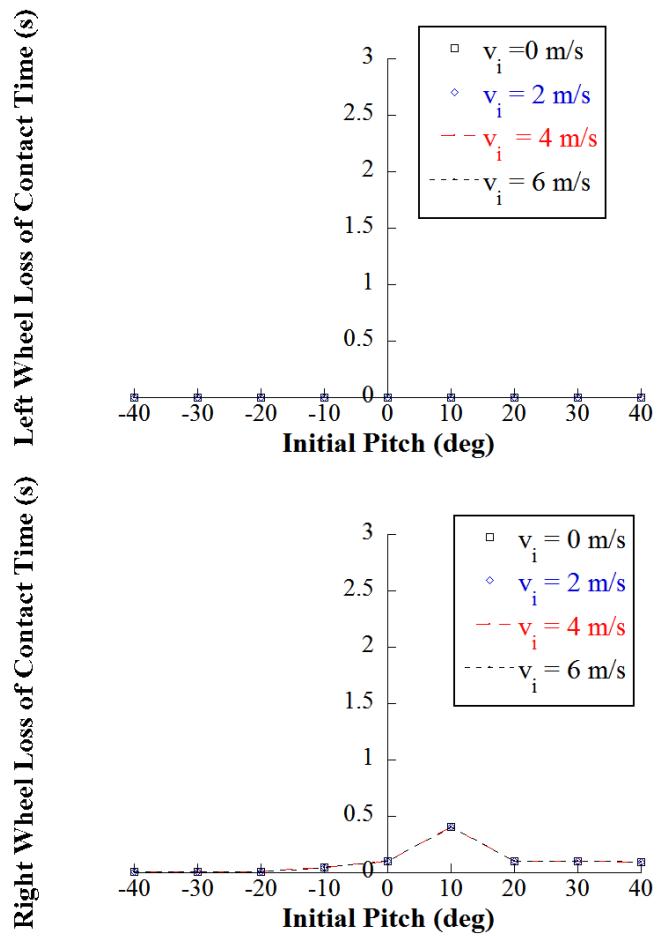
Figure 4.78: Time of contact loss of each wheel.
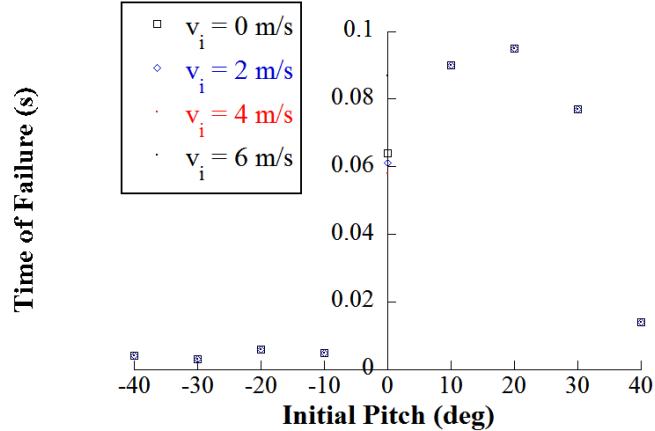
Figure 4.79: Failure Time.

4.3 Summary of failure modes

In this chapter, different failure modes were studied. It was found that sudden turning of the vehicle, without the person leaning over, caused the wheel-ground forces to become zero in less than 0.02 s. In the slope simulations, failure occurred due to surpassing the speed limit, which occurred within time frames of 0.1 to 0.7 s, depending on the initial pitch angle and the slope angle.

Simulations showed that slick surfaces make it hard for the vehicle to balance itself, and it falls to the ground within 0.75 to 1.25 s if no corrective measure is taken by the rider. When only one wheel slips on the ground, the wheel-ground contact is lost in as little as 0.1 s.

Disturbance simulations showed that depending on the magnitude of the disturbance force applied, as well as initial speed and pitch angle, the vehicle will fall down to the ground in as little as 0.2 to 0.8 s. When a force was applied to the wheel of the vehicle, the failure time occurred between 0.03 s to 0.1 s.

CHAPTER V

CONCLUSIONS

Two-wheeled inverted pendulums are systems that can be stabilized by simple controllers, such as a PD feedback controller. This approach is satisfactory in conditions where the disturbance forces are negligible and the system parameters are fixed. The Segway human transporter is a two-wheeled inverted pendulum that has been commercialized for its use in public spaces. In these spaces, there are numerous factors that can interfere with the performance of the balancing controller and can cause safety hazards to its user and the surrounding environment. Furthermore, operators with variable inertia parameters and time-varying actions make the system deviate considerably from simple linear dynamical behavior. In this thesis, a dynamic model of a two-wheeled inverted pendulum carrying a human rider was developed. This model was used to simulate basic dynamic behavior, as well as possibly dangerous conditions that can arise when traveling in real-world environments.

The literature review showed that many control techniques have been applied to the stabilization problem of two-wheeled inverted pendulums. These systems have also been proposed for some practical applications. However, there is a lack of understanding of how non ideal conditions and time-varying uncertainties affect the stability of such systems. This is especially important for practical applications, where non ideal conditions arise on a regular basis.

A dynamic model of a two-wheeled inverted pendulum was presented in Chapter II. The basic dynamics of a simple pendulum were studied where the movements of the cart in the direction in which the pendulum is falling down was demonstrated using simulations. Then, the basic geometric and mass properties of a two-wheeled

inverted pendulum were used to produce the dynamic equations of motion of the system. Following, a rigid-body model of a human rider was defined and added to the model to produce the equations of motion of a two-wheeled inverted-pendulum human transporter.

Experiments were performed to study the dynamic behavior of the Segway human transporter. Under small disturbances, the Segway-Human system has a very predictable behavior. In such cases, pitch angle and speed responses showed almost linearly under-damped responses. However, when stronger forces were involved, the human dynamics started to play a role. In such cases, the responses were difficult to predict due to the movements performed by the rider, showing the importance of their role in controlling the vehicle. Yaw turning dynamics were also studied and a map between the turning command and a resulting yaw rate was obtained from the experimental results.

The experimental results were used to set the simulation parameters for three different cases. First, the parameters of a two-wheeled inverted pendulum were adjusted to simulate the impulse response of an unloaded Segway. Then, a rigid-body model of a human was added to the model and its parameters adjusted until the simulation response matched the experimental impulse response of a loaded Segway to a manually applied force on the rider. Finally, the model parameters were set to match the response of the Segway and human rider to a known force.

The dynamic model was used to simulate different environmental conditions. Simulations of sudden turning motions showed the importance of the human rider for the stability in the roll direction. Without the person compensating for the centrifugal effect, the Segway model could not turn at very high speeds or high yaw rates without losing wheel-ground contact. When traveling on inclined surfaces, the pitch angle stability and speed are affected. It was found that the ability to climb up or go down a hill is highly affected by the pitch angle. Higher pitch angles helped the vehicle

climb up, and negative pitch angles helped to avoid instability when going down a slope. Slick surfaces also affected how well the vehicle could balance. Low friction surfaces limit the capability of the motors to accelerate the vehicle. When a high pitch angle is present and the traction provided by the ground is low, the vehicle is more likely to lose balance. If only one of the wheels loses traction with the ground, unstable yaw dynamics can be observed, and the effect was aggravated when high pitch angles were present.

Simulations of inclined surfaces and slipping in both wheels also showed that contact between the rider and the vehicle can be lost under many combinations of pitch angular accelerations and linear accelerations. Because the forces between the rider and the vehicle are compressive contact forces, when abrupt changes in net accelerations occur at high pitch angles, there is no force available to hold the rider and the vehicle together. In many of these simulations, failure conditions such as surpassing pitch and speed limits, or normal forces dropping to zero, occurred within tenths of seconds.

5.1 Future work

The work presented here can be extended in several different directions. The dynamic model presented here could be extended in order to account for an active human rider. More experimental testing can be carried out to track the human motion on different roles such as accelerating, decelerating, and turning. Markers can be placed on different segments of the person operating the vehicle. A more complex human model, in which each body segment is modeled as one rigid body could be developed. Then, the motion tracking data can be used to command the movements of the model person in the simulation.

A first step in extending the human model would be to model the interaction between him and the vehicle as a flexible link replacing the arm, as shown in Figure 5.1.
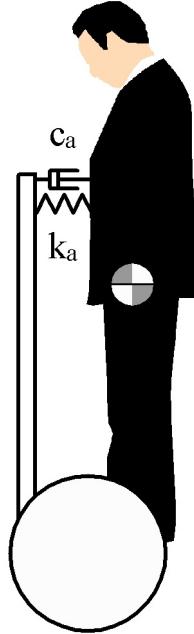
Figure 5.1: Flexible link between the transporter and its rider.

Tracking human motion when turning will provide information needed to simulate the movements required to tilt the handlebar. A more realistic scenario of the roll stability of the Segway i2 can be constructed from this information.

The model of the transporter could also be extended to account for the elasticity of the wheels. This will produce more realistic results when roll instability occurs. Currently, when sudden turning motion occurs, the model produces forces that change instantly. Including deformable wheels would eliminate this effect. The traction model can also be extended to include self aligning torques and transverse friction forces. This will allow the inclusion of more general trajectories in simulations of slipping conditions.

Steps of different heights can be simulated to determine the effectiveness of the transporter when dealing with irregularities on the surface. Having deformable wheels

will also be useful to simulate the dynamics of a Segway in this case because it plays an important role during the collision between the wheel and the obstacle.

APPENDIX A

DYNAMIC EQUATIONS - SLIPPING IN ONE WHEEL

$$\ddot{\theta}_p = -(r^2(I_{bz}+I_{pz}+2I_{wxz}+2m_ww^2+m_b(x_{wb}\cos(\theta_p)+z_{wb}\sin(\theta_p))^2+m_p(x_{wp}\cos(\theta_p)+$$

$$z_{wp}\sin(\theta_p))^2+(I_{bx}+I_{px}-I_{bz}-I_{pz})\sin(\theta_p)^2)(F_{fr}(m_b(x_{wb}\sin(\theta_p)-z_{wb}\cos(\theta_p))+m_p(x_{wp}$$

$$\sin(\theta_p)-z_{wp}\cos(\theta_p)))+(m_b(x_{wb}\sin(\theta_p)-z_{wb}\cos(\theta_p))+m_p(x_{wp}\sin(\theta_p)-z_{wp}\cos(\theta_p)))(T_l/r$$

$$+m_p(x_{wp}\cos(\theta_p)\dot{\theta}_p^2+z_{wp}\sin(\theta_p)\dot{\theta}_p^2+(x_{wp}\cos(\theta_p)+z_{wp}\sin(\theta_p))\dot{\beta}^2)+m_b(x_{wb}\cos(\theta_p)(\dot{\theta}_p^2+$$

$$\cos(\theta_p)^2\dot{\beta}^2)+\sin(\theta_p)(z_{wb}\dot{\beta}^2+z_{wb}\dot{\theta}_p^2+x_{wb}\sin(\theta_p)\cos(\theta_p)\dot{\beta}^2)))-(m_b+m_p+2m_w)(T_l+T_r-$$

$$gm_b(x_{wb}\cos(\theta_p)+z_{wb}\sin(\theta_p))-gm_p(x_{wp}\cos(\theta_p)+z_{wp}\sin(\theta_p))-((I_{bx}-I_{bz})\sin(\theta_p)\cos(\theta_p)+$$

$$(I_{px}-I_{pz})\sin(\theta_p)\cos(\theta_p)-m_p(x_{wp}\cos(\theta_p)+z_{wp}\sin(\theta_p))(x_{wp}\sin(\theta_p)-z_{wp}\cos(\theta_p))-$$

$$m_b(2x_{wb}z_{wb}\sin(\theta_p)^2+x_{wb}^2\sin(\theta_p)\cos(\theta_p)-x_{wb}z_{wb}-z_{wb}^2\sin(\theta_p)\cos(\theta_p)))\dot{\beta}^2))+I_{wy}(2w^2F_{fr}$$

$$(m_b(x_{wb}\sin(\theta_p)-z_{wb}\cos(\theta_p))+m_p(x_{wp}\sin(\theta_p)-z_{wp}\cos(\theta_p)))+w^2(m_b(x_{wb}\sin(\theta_p)-$$

$$z_{wb}\cos(\theta_p))+m_p(x_{wp}\sin(\theta_p)-z_{wp}\cos(\theta_p)))(m_p(x_{wp}\cos(\theta_p)\dot{\theta}_p^2+z_{wp}\sin(\theta_p)\dot{\theta}_p^2+(x_{wp}\cos(\theta_p)$$

$$+z_{wp}\sin(\theta_p))\dot{\beta}^2)+m_b(x_{wb}\cos(\theta_p)(\dot{\theta}_p^2+\cos(\theta_p)^2\dot{\beta}^2)+\sin(\theta_p)(z_{wb}\dot{\beta}^2+z_{wb}\dot{\theta}_p^2+x_{wb}\sin(\theta_p)$$

$$\cos(\theta_p)\dot{\beta}^2)))-w(m_b(x_{wb}\sin(\theta_p)-z_{wb}\cos(\theta_p))+m_p(x_{wp}\sin(\theta_p)-z_{wp}\cos(\theta_p)))\dot{\beta}(2(I_{bx}-$$

$$I_{bz})\sin(\theta_p)\cos(\theta_p)\dot{\theta}_p+2(I_{px}-I_{pz})\sin(\theta_p)\cos(\theta_p)\dot{\theta}_p-m_b(x_{wb}\cos(\theta_p)+z_{wb}\sin(\theta_p))(2x_{wb}$$

$$\sin(\theta_p)\dot{\theta}_p-v-2z_{wb}\cos(\theta_p)\dot{\theta}_p)-m_p(x_{wp}\cos(\theta_p)+z_{wp}\sin(\theta_p))(2x_{wp}\sin(\theta_p)\dot{\theta}_p-v-$$

$$2z_{wp}\cos(\theta_p)\dot{\theta}_p))-w^2(m_b+m_p+4m_w)(T_l+T_r-gm_b(x_{wb}\cos(\theta_p)+z_{wb}\sin(\theta_p))-$$

$$gm_p(x_{wp}\cos(\theta_p)+z_{wp}\sin(\theta_p))-((I_{bx}-I_{bz})\sin(\theta_p)\cos(\theta_p)+(I_{px}-I_{pz})\sin(\theta_p)\cos(\theta_p)-$$

$$m_p(x_{wp}\cos(\theta_p)+z_{wp}\sin(\theta_p))(x_{wp}\sin(\theta_p)-z_{wp}\cos(\theta_p))-m_b(2x_{wb}z_{wb}\sin(\theta_p)^2+x_{wb}^2\sin(\theta_p)$$

$$\cos(\theta_p)-x_{wb}z_{wb}-z_{wb}^2\sin(\theta_p)\cos(\theta_p)))\dot{\beta}^2)-(I_{bz}+I_{pz}+2I_{wxz}+m_b(x_{wb}\cos(\theta_p)+$$

$$z_{wb}\sin(\theta_p))^2+m_p(x_{wp}\cos(\theta_p)+z_{wp}\sin(\theta_p))^2+(I_{bx}+I_{px}-I_{bz}-I_{pz})\sin(\theta_p)^2)(T_l+T_r-$$

$$gm_b(x_{wb}\cos(\theta_p)+z_{wb}\sin(\theta_p))-gm_p(x_{wp}\cos(\theta_p)+z_{wp}\sin(\theta_p))-((I_{bx}-I_{bz})\sin(\theta_p)\cos(\theta_p)+$$

$$(I_{px}-I_{pz})\sin(\theta_p)\cos(\theta_p)-m_p(x_{wp}\cos(\theta_p)+z_{wp}\sin(\theta_p))(x_{wp}\sin(\theta_p)-z_{wp}\cos(\theta_p))-$$

$$m_b(2x_{wb}z_{wb}\sin(\theta_p)^2+x_{wb}^2\sin(\theta_p)\cos(\theta_p)-x_{wb}z_{wb}-z_{wb}^2\sin(\theta_p)\cos(\theta_p)))\dot{\beta}^2)))/(I_{wy}(I_{by}+$$

$I_{py} + m_b(x_{wb}^2 + z_{wb}^2) + m_p(x_{wp}^2 + z_{wp}^2))(I_{bz} + I_{pz} + 2I_{wxz} + 2m_w w^2 + 2I_{wy}w^2/r^2 + m_b(x_{wb}\cos(\theta_p) + z_{wb}\sin(\theta_p))^2 + m_p(x_{wp}\cos(\theta_p) + z_{wp}\sin(\theta_p))^2 + (I_{bx} + I_{px} - I_{bz} - I_{pz})\sin(\theta_p)^2) - (I_{wy}w^2 + r^2(I_{bz} + I_{pz} + 2I_{wxz} + 2m_w w^2 + m_b(x_{wb}\cos(\theta_p) + z_{wb}\sin(\theta_p))^2 + m_p(x_{wp}\cos(\theta_p) + z_{wp}\sin(\theta_p))^2 + (I_{bx} + I_{px} - I_{bz} - I_{pz})\sin(\theta_p)^2))((m_b + m_p + 2m_w + 2I_{wy}/r^2)(I_{by} + I_{py} + m_b(x_{wb}^2 + z_{wb}^2) + m_p(x_{wp}^2 + z_{wp}^2)) - (m_b(x_{wb}\sin(\theta_p) - z_{wb}\cos(\theta_p)) + m_p(x_{wp}\sin(\theta_p) - z_{wp}\cos(\theta_p)))^2))$

$\ddot{\beta} = -(r^2((m_b + m_p + 2m_w + 2I_{wy}/r^2)(I_{by} + I_{py} + m_b(x_{wb}^2 + z_{wb}^2) + m_p(x_{wp}^2 + z_{wp}^2)) - (m_b(x_{wb}\sin(\theta_p) - z_{wb}\cos(\theta_p)) + m_p(x_{wp}\sin(\theta_p) - z_{wp}\cos(\theta_p)))^2)(wF_{fr} - wT_l/r - \dot{\beta}(2(I_{bx} - I_{bz})\sin(\theta_p)\cos(\theta_p)\dot{\theta}_p + 2(I_{px} - I_{pz})\sin(\theta_p)\cos(\theta_p)\dot{\theta}_p - m_b(x_{wb}\cos(\theta_p) + z_{wb}\sin(\theta_p))(2x_{wb}\sin(\theta_p)\dot{\theta}_p - v - 2z_{wb}\cos(\theta_p)\dot{\theta}_p) - m_p(x_{wp}\cos(\theta_p) + z_{wp}\sin(\theta_p))(2x_{wp}\sin(\theta_p)\dot{\theta}_p - v - 2z_{wp}\cos(\theta_p)\dot{\theta}_p))) + I_{wy}(w(I_{by} + I_{py} + m_b(x_{wb}^2 + z_{wb}^2) + m_p(x_{wp}^2 + z_{wp}^2))(2T_l/r + m_p(x_{wp}\cos(\theta_p)\dot{\theta}_p^2 + z_{wp}\sin(\theta_p)\dot{\theta}_p^2 + (x_{wp}\cos(\theta_p) + z_{wp}\sin(\theta_p))\dot{\beta}^2) + m_b(x_{wb}\cos(\theta_p)(\dot{\theta}_p^2 + \cos(\theta_p)^2\dot{\beta}^2) + \sin(\theta_p)(z_{wb}\dot{\beta}^2 + z_{wb}\dot{\theta}_p^2 + x_{wb}\sin(\theta_p)\cos(\theta_p)\dot{\beta}^2))) + (I_{by} + I_{py} + m_b(x_{wb}^2 + z_{wb}^2) + m_p(x_{wp}^2 + z_{wp}^2))\dot{\beta}(2(I_{bx} - I_{bz})\sin(\theta_p)\cos(\theta_p)\dot{\theta}_p + 2(I_{px} - I_{pz})\sin(\theta_p)\cos(\theta_p)\dot{\theta}_p - m_b(x_{wb}\cos(\theta_p) + z_{wb}\sin(\theta_p))(2x_{wb}\sin(\theta_p)\dot{\theta}_p - v - 2z_{wb}\cos(\theta_p)\dot{\theta}_p) - m_p(x_{wp}\cos(\theta_p) + z_{wp}\sin(\theta_p))(2x_{wp}\sin(\theta_p)\dot{\theta}_p - v - 2z_{wp}\cos(\theta_p)\dot{\theta}_p)) - w(m_b(x_{wb}\sin(\theta_p) - z_{wb}\cos(\theta_p)) + m_p(x_{wp}\sin(\theta_p) - z_{wp}\cos(\theta_p)))(T_l + T_r - gm_b(x_{wb}\cos(\theta_p) + z_{wb}\sin(\theta_p)) - gm_p(x_{wp}\cos(\theta_p) + z_{wp}\sin(\theta_p)) - ((I_{bx} - I_{bz})\sin(\theta_p)\cos(\theta_p) + (I_{px} - I_{pz})\sin(\theta_p)\cos(\theta_p) - m_p(x_{wp}\cos(\theta_p) + z_{wp}\sin(\theta_p))(x_{wp}\sin(\theta_p) - z_{wp}\cos(\theta_p)) - m_b(2x_{wb}z_{wb}\sin(\theta_p)^2 + x_{wb}^2\sin(\theta_p)\cos(\theta_p) - x_{wb}z_{wb} - z_{wb}^2\sin(\theta_p)\cos(\theta_p)))\dot{\beta}^2)))$

$/(I_{wy}(I_{by} + I_{py} + m_b(x_{wb}^2 + z_{wb}^2) + m_p(x_{wp}^2 + z_{wp}^2))(I_{bz} + I_{pz} + 2I_{wxz} + 2m_w w^2 + 2I_{wy}w^2/r^2 + m_b(x_{wb}\cos(\theta_p) + z_{wb}\sin(\theta_p))^2 + m_p(x_{wp}\cos(\theta_p) + z_{wp}\sin(\theta_p))^2 + (I_{bx} + I_{px} - I_{bz} - I_{pz})\sin(\theta_p)^2) - (I_{wy}w^2 + r^2(I_{bz} + I_{pz} + 2I_{wxz} + 2m_w w^2 + m_b(x_{wb}\cos(\theta_p) + z_{wb}\sin(\theta_p))^2 + m_p(x_{wp}\cos(\theta_p) + z_{wp}\sin(\theta_p))^2 + (I_{bx} + I_{px} - I_{bz} - I_{pz})\sin(\theta_p)^2))((m_b + m_p + 2m_w + 2I_{wy}/r^2)(I_{by} + I_{py} + m_b(x_{wb}^2 + z_{wb}^2) + m_p(x_{wp}^2 + z_{wp}^2)) - (m_b(x_{wb}\sin(\theta_p) - z_{wb}\cos(\theta_p)) + m_p(x_{wp}\sin(\theta_p) - z_{wp}\cos(\theta_p)))^2))$

$$\dot{v} = -(r^2(I_{bz}+I_{pz}+2I_{wxz}+2m_ww^2+m_b(x_{wb}\cos(\theta_p)+z_{wb}\sin(\theta_p))^2+m_p(x_{wp}\cos(\theta_p)+$$

$$z_{wp}\sin(\theta_p))^2+(I_{bx}+I_{px}-I_{bz}-I_{pz})\sin(\theta_p)^2)((I_{by}+I_{py}+m_b(x_{wb}^2+z_{wb}^2)+m_p(x_{wp}^2+$$

$$z_{wp}^2))F_{fr}+(I_{by}+I_{py}+m_b(x_{wb}^2+z_{wb}^2)+m_p(x_{wp}^2+z_{wp}^2))(T_l/r+m_p(x_{wp}\cos(\theta_p)\dot{\theta}_p^2+$$

$$z_{wp}\sin(\theta_p)\dot{\theta}_p^2+(x_{wp}\cos(\theta_p)+z_{wp}\sin(\theta_p))\dot{\beta}^2)+m_b(x_{wb}\cos(\theta_p)(\dot{\theta}_p^2+\cos(\theta_p)^2\dot{\beta}^2)+\sin(\theta_p)$$

$$(z_{wb}\dot{\beta}^2+z_{wb}\dot{\theta}_p^2+x_{wb}\sin(\theta_p)\cos(\theta_p)\dot{\beta}^2)))-(m_b(x_{wb}\sin(\theta_p)-z_{wb}\cos(\theta_p))+m_p(x_{wp}\sin(\theta_p)-$$

$$z_{wp}\cos(\theta_p)))(T_l+T_r-gm_b(x_{wb}\cos(\theta_p)+z_{wb}\sin(\theta_p))-gm_p(x_{wp}\cos(\theta_p)+z_{wp}\sin(\theta_p))-$$

$$((I_{bx}-I_{bz})\sin(\theta_p)\cos(\theta_p)+(I_{px}-I_{pz})\sin(\theta_p)\cos(\theta_p)-m_p(x_{wp}\cos(\theta_p)+z_{wp}\sin(\theta_p))$$

$$(x_{wp}\sin(\theta_p)-z_{wp}\cos(\theta_p))-m_b(2x_{wb}z_{wb}\sin(\theta_p)^2+x_{wb}^2\sin(\theta_p)\cos(\theta_p)-x_{wb}z_{wb}-z_{wb}^2\sin(\theta_p)$$

$$\cos(\theta_p)))\dot{\beta}^2))+I_{wy}w(2w(I_{by}+I_{py}+m_b(x_{wb}^2+z_{wb}^2)+m_p(x_{wp}^2+z_{wp}^2))F_{fr}+w(I_{by}+$$

$$I_{py}+m_b(x_{wb}^2+z_{wb}^2)+m_p(x_{wp}^2+z_{wp}^2))(m_p(x_{wp}\cos(\theta_p)\dot{\theta}_p^2+z_{wp}\sin(\theta_p)\dot{\theta}_p^2+(x_{wp}\cos(\theta_p)+$$

$$z_{wp}\sin(\theta_p))\dot{\beta}^2)+m_b(x_{wb}\cos(\theta_p)(\dot{\theta}_p^2+\cos(\theta_p)^2\dot{\beta}^2)+\sin(\theta_p)(z_{wb}\dot{\beta}^2+z_{wb}\dot{\theta}_p^2+x_{wb}\sin(\theta_p)$$

$$\cos(\theta_p)\dot{\beta}^2)))-(I_{by}+I_{py}+m_b(x_{wb}^2+z_{wb}^2)+m_p(x_{wp}^2+z_{wp}^2))\dot{\beta}(2(I_{bx}-I_{bz})\sin(\theta_p)\cos(\theta_p)\dot{\theta}_p+$$

$$2(I_{px}-I_{pz})\sin(\theta_p)\cos(\theta_p)\dot{\theta}_p-m_b(x_{wb}\cos(\theta_p)+z_{wb}\sin(\theta_p))(2x_{wb}\sin(\theta_p)\dot{\theta}_p-v-2z_{wb}\cos(\theta_p)$$

$$\dot{\theta}_p)-m_p(x_{wp}\cos(\theta_p)+z_{wp}\sin(\theta_p))(2x_{wp}\sin(\theta_p)\dot{\theta}_p-v-2z_{wp}\cos(\theta_p)\dot{\theta}_p))-w(m_b(x_{wb}\sin(\theta_p)-$$

$$z_{wb}\cos(\theta_p))+m_p(x_{wp}\sin(\theta_p)-z_{wp}\cos(\theta_p)))(T_l+T_r-gm_b(x_{wb}\cos(\theta_p)+z_{wb}\sin(\theta_p))-$$

$$gm_p(x_{wp}\cos(\theta_p)+z_{wp}\sin(\theta_p))-((I_{bx}-I_{bz})\sin(\theta_p)\cos(\theta_p)+(I_{px}-I_{pz})\sin(\theta_p)\cos(\theta_p)-$$

$$m_p(x_{wp}\cos(\theta_p)+z_{wp}\sin(\theta_p))(x_{wp}\sin(\theta_p)-z_{wp}\cos(\theta_p))-m_b(2x_{wb}z_{wb}\sin(\theta_p)^2+x_{wb}^2\sin(\theta_p)$$

$$\cos(\theta_p)-x_{wb}z_{wb}-z_{wb}^2\sin(\theta_p)\cos(\theta_p)))\dot{\beta}^2)))/(I_{wy}(I_{by}+I_{py}+m_b(x_{wb}^2+z_{wb}^2)+m_p(x_{wp}^2+$$

$$z_{wp}^2))(I_{bz}+I_{pz}+2I_{wxz}+2m_ww^2+2I_{wy}w^2/r^2+m_b(x_{wb}\cos(\theta_p)+z_{wb}\sin(\theta_p))^2+m_p(x_{wp}\cos(\theta_p)$$

$$+z_{wp}\sin(\theta_p))^2+(I_{bx}+I_{px}-I_{bz}-I_{pz})\sin(\theta_p)^2)-(I_{wy}w^2+r^2(I_{bz}+I_{pz}+2I_{wxz}+$$

$$2m_ww^2+m_b(x_{wb}\cos(\theta_p)+z_{wb}\sin(\theta_p))^2+m_p(x_{wp}\cos(\theta_p)+z_{wp}\sin(\theta_p))^2+(I_{bx}+I_{px}-$$

$$I_{bz}-I_{pz})\sin(\theta_p)^2))((m_b+m_p+2m_w+2I_{wy}/r^2)(I_{by}+I_{py}+m_b(x_{wb}^2+z_{wb}^2)+m_p(x_{wp}^2+$$

$$z_{wp}^2))-(m_b(x_{wb}\sin(\theta_p)-z_{wb}\cos(\theta_p))+m_p(x_{wp}\sin(\theta_p)-z_{wp}\cos(\theta_p)))^2))$$

$$\dot{v}_s = -r^4((F_{fr}-T_r/r)(I_{bz}+I_{pz}+2I_{wxz}+2m_ww^2+2I_{wy}w^2/r^2+m_b(x_{wb}\cos(\theta_p)+$$

$$z_{wb}\sin(\theta_p))^2+m_p(x_{wp}\cos(\theta_p)+z_{wp}\sin(\theta_p))^2+(I_{bx}+I_{px}-I_{bz}-I_{pz})\sin(\theta_p)^2)((m_b+$$

$$m_p+2m_w+2I_{wy}/r^2)(I_{by}+I_{py}+m_b(x_{wb}^2+z_{wb}^2)+m_p(x_{wp}^2+z_{wp}^2))-(m_b(x_{wb}\sin(\theta_p)-$$

$$z_{wb}\cos(\theta_p)) + m_p(x_{wp}\sin(\theta_p) - z_{wp}\cos(\theta_p)))^2)/(I_{wy}(I_{wy}(I_{by} + I_{py} + m_b(x_{wb}^2 + z_{wb}^2) +$$

$$m_p(x_{wp}^2 + z_{wp}^2))(I_{bz} + I_{pz} + 2I_{wxz} + 2m_ww^2 + 2I_{wy}w^2/r^2 + m_b(x_{wb}\cos(\theta_p) + z_{wb}\sin(\theta_p))^2 +$$

$$m_p(x_{wp}\cos(\theta_p) + z_{wp}\sin(\theta_p))^2 + (I_{bx} + I_{px} - I_{bz} - I_{pz})\sin(\theta_p)^2) - (I_{wy}w^2 + r^2(I_{bz} + I_{pz} +$$

$$2I_{wxz} + 2m_ww^2 + m_b(x_{wb}\cos(\theta_p) + z_{wb}\sin(\theta_p))^2 + m_p(x_{wp}\cos(\theta_p) + z_{wp}\sin(\theta_p))^2 + (I_{bx} +$$

$$I_{px} - I_{bz} - I_{pz})\sin(\theta_p)^2))((m_b + m_p + 2m_w + 2I_{wy}/r^2)(I_{by} + I_{py} + m_b(x_{wb}^2 + z_{wb}^2) + m_p(x_{wp}^2 +$$

$$z_{wp}^2)) - (m_b(x_{wb}\sin(\theta_p) - z_{wb}\cos(\theta_p)) + m_p(x_{wp}\sin(\theta_p) - z_{wp}\cos(\theta_p)))^2))) + ((I_{by} + I_{py} +$$

$$m_b(x_{wb}^2 + z_{wb}^2) + m_p(x_{wp}^2 + z_{wp}^2))(I_{bz} + I_{pz} + 2I_{wxz} + 2m_ww^2 + 2I_{wy}w^2/r^2 + m_b(x_{wb}\cos(\theta_p) +$$

$$z_{wb}\sin(\theta_p))^2 + m_p(x_{wp}\cos(\theta_p) + z_{wp}\sin(\theta_p))^2 + (I_{bx} + I_{px} - I_{bz} - I_{pz})\sin(\theta_p)^2)((T_l + T_r)/r +$$

$$m_p(x_{wp}\cos(\theta_p)\dot{\theta}_p^2 + z_{wp}\sin(\theta_p)\dot{\theta}_p^2 + (x_{wp}\cos(\theta_p) + z_{wp}\sin(\theta_p))\dot{\beta}^2) + m_b(x_{wb}\cos(\theta_p)(\dot{\theta}_p^2 +$$

$$\cos(\theta_p)^2\dot{\beta}^2) + \sin(\theta_p)(z_{wb}\dot{\beta}^2 + z_{wb}\dot{\theta}_p^2 + x_{wb}\sin(\theta_p)\cos(\theta_p)\dot{\beta}^2))) - w((m_b + m_p + 2m_w +$$

$$2I_{wy}/r^2)(I_{by} + I_{py} + m_b(x_{wb}^2 + z_{wb}^2) + m_p(x_{wp}^2 + z_{wp}^2)) - (m_b(x_{wb}\sin(\theta_p) - z_{wb}\cos(\theta_p)) +$$

$$m_p(x_{wp}\sin(\theta_p) - z_{wp}\cos(\theta_p)))^2)(w(T_l - T_r)/r + \dot{\beta}(2(I_{bx} - I_{bz})\sin(\theta_p)\cos(\theta_p)\dot{\theta}_p + 2(I_{px} -$$

$$I_{pz})\sin(\theta_p)\cos(\theta_p)\dot{\theta}_p - m_b(x_{wb}\cos(\theta_p) + z_{wb}\sin(\theta_p))(2x_{wb}\sin(\theta_p)\dot{\theta}_p - v - 2z_{wb}\cos(\theta_p)\dot{\theta}_p) -$$

$$m_p(x_{wp}\cos(\theta_p) + z_{wp}\sin(\theta_p))(2x_{wp}\sin(\theta_p)\dot{\theta}_p - v - 2z_{wp}\cos(\theta_p)\dot{\theta}_p))) - (m_b(x_{wb}\sin(\theta_p) -$$

$$z_{wb}\cos(\theta_p)) + m_p(x_{wp}\sin(\theta_p) - z_{wp}\cos(\theta_p)))(I_{bz} + I_{pz} + 2I_{wxz} + 2m_ww^2 + 2I_{wy}w^2/r^2 +$$

$$m_b(x_{wb}\cos(\theta_p) + z_{wb}\sin(\theta_p))^2 + m_p(x_{wp}\cos(\theta_p) + z_{wp}\sin(\theta_p))^2 + (I_{bx} + I_{px} - I_{bz} -$$

$$I_{pz})\sin(\theta_p)^2)(T_l + T_r - gm_b(x_{wb}\cos(\theta_p) + z_{wb}\sin(\theta_p)) - gm_p(x_{wp}\cos(\theta_p) + z_{wp}\sin(\theta_p)) -$$

$$((I_{bx} - I_{bz})\sin(\theta_p)\cos(\theta_p) + (I_{px} - I_{pz})\sin(\theta_p)\cos(\theta_p) - m_p(x_{wp}\cos(\theta_p) + z_{wp}\sin(\theta_p))(x_{wp}$$

$$\sin(\theta_p) - z_{wp}\cos(\theta_p)) - m_b(2x_{wb}z_{wb}\sin(\theta_p)^2 + x_{wb}^2\sin(\theta_p)\cos(\theta_p) - x_{wb}z_{wb} - z_{wb}^2\sin(\theta_p)$$

$$\cos(\theta_p)))\dot{\beta}^2))/(r^2(I_{wy}(I_{by} + I_{py} + m_b(x_{wb}^2 + z_{wb}^2) + m_p(x_{wp}^2 + z_{wp}^2))(I_{bz} + I_{pz} + 2I_{wxz} +$$

$$2m_ww^2 + 2I_{wy}w^2/r^2 + m_b(x_{wb}\cos(\theta_p) + z_{wb}\sin(\theta_p))^2 + m_p(x_{wp}\cos(\theta_p) + z_{wp}\sin(\theta_p))^2 +$$

$$(I_{bx} + I_{px} - I_{bz} - I_{pz})\sin(\theta_p)^2) - (I_{wy}w^2 + r^2(I_{bz} + I_{pz} + 2I_{wxz} + 2m_ww^2 + m_b(x_{wb}\cos(\theta_p) +$$

$$z_{wb}\sin(\theta_p))^2 + m_p(x_{wp}\cos(\theta_p) + z_{wp}\sin(\theta_p))^2 + (I_{bx} + I_{px} - I_{bz} - I_{pz})\sin(\theta_p)^2))((m_b +$$

$$m_p + 2m_w + 2I_{wy}/r^2)(I_{by} + I_{py} + m_b(x_{wb}^2 + z_{wb}^2) + m_p(x_{wp}^2 + z_{wp}^2)) - (m_b(x_{wb}\sin(\theta_p) -$$

$$z_{wb}\cos(\theta_p)) + m_p(x_{wp}\sin(\theta_p) - z_{wp}\cos(\theta_p)))^2))))$$

REFERENCES

[1] AEROSPACE MEDICAL RESEARCH LABORATORY, "Investigation of the Inertial Properties of the Human Body," Accessed on May 24, 2012. Available: http://www.dtic.mil.

[2] AEROSPACE MEDICAL RESEARCH LABORATORY, "Moments of Inertia and Centers of Gravity of the Living Human Body," Accessed on May 24, 2012. Available: http://www.dtic.mil.

[3] ANDERSON, C. W., "Learning to control an inverted pendulum with connectionist networks," in *American Control Conference, 1988*, pp. 2294 –2298, june 1988.

[4] BAGDANOFF, J. L. and CITRON, S. J., "Experiments with an inverted pendulum subject to random parametric excitation," pp. 447–452, 1965.

[5] BLITZER, L., "Inverted pendulum," vol. 33, no. 12, pp. 1076–1078, 1965.

[6] BONIFACE, K., MCKAY, M. P., LUCAS, R., SHAFFER, A., and SIKKA, N., "Serious injuries related to the Segway personal transporter: A case series," *Annals of Emergency Medicine*, vol. 57, no. 4, pp. 370 – 374, 2011.

[7] BUI, T. H., NGUYEN, T. T., CHUNG, T. L., and KIM, S. B., "A simple nonlinear control of a two-wheeled welding mobile robot," *International Journal of Control, Automation, and Systems*, vol. 1, no. 1, pp. 35–42, 2003.

[8] CANUDAS DE WIT, C. and TSIOTRAS, P., "Dynamic tire friction models for vehicle traction control," in *Decision and Control, 1999. Proceedings of the 38th IEEE Conference on*, vol. 4, pp. 3746–3751, IEEE, 1999.

[9] CHOI, D. and OH, J.-H., "Human-friendly motion control of a wheeled inverted pendulum by reduced-order disturbance observer," in *Robotics and Automation, 2008. ICRA 2008. IEEE International Conference on*, pp. 2521 –2526, may 2008.

[10] DEEGAN, P., THIBODEAU, B., and GRUPEN, R., *Designing a self-stabilizing robot for dynamic mobile manipulation.* Proc. RSS Workshop: Manipulation for Human Environments, Philadelphia, PA, Aug, 2006.

[11] DING, F., HUANG, J., WANG, Y., MATSUNO, T., FUKUDA, T., and SEKIYAMA, K., "Modeling and control of a novel narrow vehicle," in *Robotics and Biomimetics (ROBIO), 2010 IEEE International Conference on*, pp. 1130 –1135, dec. 2010.

[12] D.W, "Segway," Accessed on May24, 2012. Available: http://www.dudeworld.com.au/REVIEW.SEGWAY.HTML.

[13] GRASSER, F., D'ARRIGO, A., COLOMBI, S., and RUFER, A. C., "Joe: A mobile, inverted pendulum," *IEEE Transactions on Industrial Electronics*, vol. 49, pp. 107–114, February 2002.

[14] HA, Y.-S. and YUTA, S., "Trajectory tracking control for navigation of the inverse pendulum type self-contained mobile robot," *Robotics and Autonomous Systems*, 1996.

[15] HUANG, C., WANG, W.-J., and CHIU, C.-H., "Velocity control realisation for a self-balancing transporter," *Control Theory Applications, IET*, vol. 5, pp. 1551 –1560, 8 2011.

[16] JEONG, S. H. and TAKAHASHI, T., "Wheeled inverted pendulum type assistant robot: inverted mobile, standing, and sitting motions," in *Intelligent Robots and Systems, 2007. IROS 2007. IEEE/RSJ International Conference on*, pp. 1932 –1937, 29 2007-nov. 2 2007.

[17] JUNG, S. and KIM, S. S., "Control experiment of a wheel-driven mobile inverted pendulum using neural network," *Control Systems Technology, IEEE Transactions on*, vol. 16, pp. 297 –303, march 2008.

[18] KAKIO, M., MIYASHITA, T., MITSUNAGA, N., ISHIGURO, H., and HAGITA, N., "Natural reflexive behavior for wheeled inverted pendulum type humanoid robots," in *Robot and Human Interactive Communication, 2006. ROMAN 2006. The 15th IEEE International Symposium on*, pp. 451 –456, sept. 2006.

[19] KAMEN, D., AMBROGI, R., DATTOLO, J., DUGGAN, R., FIELD, J., HEINZMANN, R., McCAMBRIDGE, M., MORRELL, J., PIEDMONTE, M., ROSASCO, R., and OTHERS, "Control of a personal transporter based on user position," Oct. 2 2007. US Patent 7,275,607.

[20] KAMEN, D., ARLING, R., FIELD, J., MORRELL, J., and POMPA, J., "Steering control of a personal transporter," June 24 2003. US Patent 6,581,714.

[21] KATARIYA, A. S., "Optimal State-Feedback and Output-Feedback Controllers for the Wheeled Inverted Pendulum System," Master's thesis, Georgia Institute of Technology, 2010.

[22] KIM, Y., KIM, S. H., and KWAK, Y. K., "Improving driving ability for a two-wheeled inverted-pendulum-type autonomous vehicle," *Proceedings of the Institution of Mechanical Engineers, Part D: Journal of Automobile Engineering*, vol. 220, no. 2, pp. 165–175, 2006.

[23] KIM, Y., KIM, S. H., and KWAK, Y. K., "Dynamic analysis of a nonholonomic two-wheeled inverted pendulum robot," *Journal of Intelligent and Robotic Systems*, vol. 44, pp. 25–46, 2005.

[24] Ko, A., Lau, H., and Lau, T., "Soho security with mini self-balancing robots," *The Industrial Robot*, vol. 32, no. 6, pp. 492–498, 2005.

[25] Kolhe, P., Dantam, N., and Stilman, M., "Dynamic pushing strategies for dynamically stable mobile manipulators," in *Robotics and Automation (ICRA), 2010 IEEE International Conference on*, pp. 3745 –3750, may 2010.

[26] Kuindersma, S., "Control model learning for whole-body mobile manipulation," vol. 3, (Atlanta, GA, United states), pp. 1939 – 1940, 2010.

[27] Li, J., Gao, X., Huang, Q., Du, Q., and Duan, X., "Mechanical design and dynamic modeling of a two-wheeled inverted pendulum mobile robot," in *Automation and Logistics, 2007 IEEE International Conference on*, pp. 1614 –1619, aug. 2007.

[28] Li, Z. and Xu, C., "Adaptive fuzzy logic control of dynamic balance and motion for wheeled inverted pendulums," *Fuzzy Sets and Systems*, vol. 160, no. 12, pp. 1787 – 1803, 2009. <ce:title>Theme: Control Engineering</ce:title>.

[29] Li, Z. and Zhang, Y., "Robust adaptive motion force control for wheeled inverted pendulums," *Automatica*, vol. 46, no. 8, pp. 1346 – 1353, 2010.

[30] Lowenstern, E. R., "Stabilising effect of imposed oscillations on a dynamical system," *Philosophical Magazine*, vol. 13, pp. 458–486, 1932.

[31] Miles, J., "Directly forced oscillations of an inverted pendulum," *Physics Letters A*, vol. 133, no. 6, pp. 295 – 297, 1988.

[32] Morrell, J. B. and Field, D., "Design of a closed loop controller for a two wheeled balancing transporter," in *Proceedings of the 2007 IEEE/RSJ International Conference on Intelligent Robots and Systems*, (San Diego, CA, USA), Oct 29 - Nov 2 2007.

[33] Nasrallah, D., Angeles, J., and Michalska, H., "Velocity and orientation control of an anti-tilting mobile robot moving on an inclined plane," in *Robotics and Automation, 2006. ICRA 2006. Proceedings 2006 IEEE International Conference on*, pp. 3717 –3723, may 2006.

[34] Nawawi, S., Ahmad, M., and Osman, J., "Development of a two-wheeled inverted pendulum mobile robot," in *Research and Development, 2007. SCOReD 2007. 5th Student Conference on*, pp. 1 –5, dec. 2007.

[35] Nelson, R. A. and Olsson, M. G., "The pendulum rich physics from a simple system," *American Journal of Physics*, vol. 54, no. 2, pp. 112–121, 1986.

[36] Ness, D. J., "Small oscillations of a stabilized, inverted pendulum," vol. 35, no. 10, pp. 964–967, 1967.

[37] PACEJKA, H., BAKKER, E., and NYBORG, L., "Tyre modelling for use in vehicle dynamics studies," *SAE paper*, vol. 870421, 1987.

[38] PATHAK, K., FRANCH, J., and AGRAWAL, S. K., "Velocity and position control of a wheeled inverted pendulum by partial feedback linearization," *IEEE Transactions on Robotics*, vol. 21, no. 3, pp. 505–513, 2005.

[39] PAVEL HOLOBORODKO, "Smooth noise-robust differentiators," Accessed on May14, 2012. Available: http://www.holoborodko.com/pavel/numerical-methods/numerical-derivative/smooth-low-noise-differentiators.

[40] PHELPS, F. and JR., J. H., "An analytical solution of the inverted pendulum," 1964.

[41] PIPPARD, A. B., "The inverted pendulum," *European Journal of Physics*, vol. 8, no. 3, p. 203, 1987.

[42] ROZENBLAT, G. H., "Optimal parametric stabilization of an inverted pendulum," *Journal of Applied Mathematics and Mechanics*, vol. 45, no. 1, pp. 45 − 50, 1981.

[43] RUAN, X.-G. and ZHAO, J., "The flexible two-wheeled self-balancing robot based on hopfield," in *Intelligent Robotics and Applications* (XIE, M., XIONG, Y., XIONG, C., LIU, H., and HU, Z., eds.), vol. 5928 of *Lecture Notes in Computer Science*, pp. 1196–1204, Springer Berlin / Heidelberg, 2009.

[44] SAHBA, M., "Computer-aided design of feedback controllers for nonlinear systems with applications to control of a double-inverted pendulum," *IEE proceedings. D, Control theory and applications*, vol. 130, no. 6, pp. 350–358, 1983.

[45] SASAKI, M., YANAGIHARA, N., MATSUMOTO, O., and KOMORIYA, K., "Forward and backward motion control of personal riding-type wheeled mobile platform," in *Robotics and Automation, 2004. Proceedings. ICRA '04. 2004 IEEE International Conference on*, vol. 4, pp. 3331 − 3336 Vol.4, 26-may 1, 2004.

[46] SAWATZKY, B., DENISON, I., and TAWASHY, A., "The segway for people with disabilities meeting clients' mobility goals," *American journal of physical medicine and rehabilitation*, vol. 88, no. 6, pp. 484–490, 2009.

[47] SEGWAY INC., "PT Models for Individuals," Accessed on May 6, 2012. Available: http://www.segway.com/individual/models/index.php.

[48] SEGWAY ROBOTICS, "Project PUMA," Accessed on May 6, 2012. Available: http://www.segway.com/puma/.

[49] SEGWAY ROBOTICS, "Segway RMP," Accessed on May 6, 2012. Available: http://rmp.segway.com/.

[50] SHIROMA, N., MATSUMOTO, O., and TANI, K., "Cooperative behavior of a mechanically unstable mobile robot for object transportation," *JSME International Journal Series C*, vol. 42, no. 4, pp. 965–973, 1999.

[51] STEPHENSON, A., "A new type of dynamic stability," *Proc. of the Manchester Literary and Philosophical Society*, 1908.

[52] STEPHENSON, A., "On induced stability," *Philosophical Magazine*, 1909.

[53] STILMAN, M., WANG, J., TEEYAPAN, K., and MARCEAU, R., "Optimized control strategies for wheeled humanoids and mobile manipulators," in *Humanoid Robots, 2009. Humanoids 2009. 9th IEEE-RAS International Conference on*, pp. 568 –573, dec. 2009.

[54] TAKAHASHI, Y., NONOSHITA, H., NAKAMURA, T., and MAEDA, Y., "Behavioral development of ball kicking motion of a two-wheeled inverted pendulum mobile robot," in *Fuzzy Systems (FUZZ), 2010 IEEE International Conference on*, pp. 1 –6, july 2010.

[55] TAKEI, T., IMAMURA, R., and YUTA, S., "Baggage transportation and navigation by a wheeled inverted pendulum mobile robot," *Industrial Electronics, IEEE Transactions on*, vol. 56, pp. 3985 –3994, oct. 2009.

[56] TAKEI, T., MATSUMOTO, O., and KOMORIYA, K., "Simultaneous estimation of slope angle and handling force when getting on and off a human-riding wheeled inverted pendulum vehicle," in *Intelligent Robots and Systems, 2009. IROS 2009. IEEE/RSJ International Conference on*, pp. 4553 –4558, oct. 2009.

[57] VICON MOTION SYSTEMS LIMITED, "Vicon | Products | Cameras | MX-3+ [Online]," Accessed on March 15, 2012. Available: http://www.vicon.com/products/mx3.html.

[58] VICON MOTION SYSTEMS LIMITED, "Vicon MX Hardware System Reference, Revision 1.6, Oxford, UK, 2007."

[59] VLASSIS, N., TOUSSAINT, M., KONTES, G., and PIPERIDIS, S., "Learning model-free robot control by a monte carlo em algorithm," *Autonomous Robots*, vol. 27, pp. 123–130, 2009. 10.1007/s10514-009-9132-0.

[60] WINTER, D., PATLA, A., PRINCE, F., ISHAC, M., and GIELO-PERCZAK, K., "Stiffness control of balance in quiet standing," *Journal of Neurophysiology*, vol. 80, no. 3, pp. 1211–1221, 1998.

[61] YAMAFUJI, K. and KAWAMURA, T., "Study on the postural and driving control of a coaxial bicycle," *Transactions of the JSME, Series C*, vol. 54, no. 501, pp. 1114–1121, 1988.

[62] YAMAKAWA, T., "Stabilization of an inverted pendulum by a high-speed fuzzy-logic controller hardware system," *Fuzzy Sets and Systems*, vol. 32, no. 2, pp. 161–180, 1989.